AN ABSTRACT OF THE THESIS OF

Siavash Yousefi for the degree of Master of Science in Electrical and Computer Engineering on May 29, 2008.

Title: Digital Pulse Shape Discrimination Methods for Triple-Layer Phoswich Detectors Using Wavelets and Fuzzy Logic.

Abstract approved:

_____

Luca Lucchese

A two-channel data acquisition system for simultaneous detection and discrimination of beta particles and gamma rays has been developed. Each channel measures and analyzes the input pulses resulting from the absorption of radiation in the layers of the detector. The detector is a triple-layer phoswich (phosphor sandwich) scintillation detector followed by a photomultiplier tube (PMT). The PMT amplifies the photons and converts them into an electric signal. The signal is digitized and sent to the host computer for further processing. Two new digital algorithms based on Fuzzy Logic and on the Continuous Wavelet Transform have been developed and are discussed in this thesis.

In the first method, a de-noising algorithm based on the Wavelet Transform is implemented to reduce the effect of noise introduced by the analog channel and by the photomultiplier tube. Three new timing features are extracted and given as

input to a fuzzy interface system. The main goal of fuzziness in a data set is to reduce the system complexity and to provide a model that allows for approximate results. Compared to the method which was originally implemented for this detector, the fuzzy algorithm shows a better performance in separating beta and gamma spectra, especially at high energies. Also, absorption in multiple layers is detected more efficiently.

The second algorithm is based on the Continuous Wavelet Transform. The novelty of this method consists in using scale-domain features. Since the output pulse shape of the photomultiplier tube is a non-stationary signal, conventional Fourier methods are not efficient for analyzing these signals and most of the existing pulse shape discrimination methods use time-domain features. Therefore, a time-frequency space is better suited to analyze these non-stationary signals. This method shows better performance over existing time-domain methods in terms of robustness to noise and reliability.

The simultaneous detection of beta particles and gamma rays has several applications (for instance detection of underground nuclear explosions). The methods presented in this thesis could also be used in alpha/beta/neutron/gamma discrimination systems for cancer diagnosis and treatment.

Digital Pulse Shape Discrimination Methods for Triple-Layer Phoswich Detectors Using Wavelets and Fuzzy Logic

by
Siavash Yousefi

A THESIS

submitted to

Oregon State University

in partial fulfillment of

the requirements for the

degree of

Master of Science

Presented May 29, 2008

Commencement June 2009

Master of Science thesis of Siavash Youesefi presented on May 29, 2008.

APPROVED:

_____

Major Professor, representing Electrical and Computer Engineering

_____

Director of the School of Electrical Engineering and Computer Science

_____

Dean of the Graduate School

I understand that my thesis will become part of the permanent collection of Oregon State University libraries. My signature below authorizes release of my thesis to any reader upon request.

_____

Siavash Yousefi, Author

ACKNOWLEDGMENTS

I owe a great debt of appreciation to my parents Ahmad Ali and Mina, who made my graduate studies in the United States possible and constantly supported me and always gave me hope to rise above all difficulties.

My deepest gratitude is to my advisor, Dr. Luca Lucchese, for his support and guidance during my two years as a graduate student. His patience, motivation and creativity helped me overcome many problems and finish this thesis. He taught me how to express the ideas I had in mind and find solutions to complicated problems. He has been not only an exceptional advisor, but also a good friend to me.

I would like to acknowledge Dr. Abi Farsoni and Dr. David Hamby from the Radiation Center and Nuclear Engineering Department at Oregon State University for their partial support and collaboration on this project and for providing the digital data from the detector they designed and built.

I would also like to thank Dr. Michael D. Aspinall from Lancaster University who provided us with the data for neutron/gamma discrimination.

During my stay in Corvallis, I made new friends and I hope we remain friends after we have all gone separate ways. Nima Maghari: thanks for your help and company, as my Iranian friend. Daniel Lopez, Eduardo Alban, Panupat Poocharoen, Yun Rim Park and Anne Setiono: thank you for being special friends and thank you for our many shared beautiful moments.

TABLE OF CONTENTS

Page

TABLE OF CONTENTS (Continued)

Page

LIST OF FIGURES

Figure Page

LIST OF FIGURES (Continued)

Figure Page

LIST OF FIGURES (Continued)

Figure Page

LIST OF FIGURES (Continued)

Figure Page

LIST OF FIGURES (Continued)

Figure Page

LIST OF TABLES

Table Page

Digital Pulse Shape Discrimination Methods for Triple-Layer Phoswich Detectors Using Wavelets and Fuzzy Logic

1 Introduction

Scintillators are used to detect electromagnetic waves or particles by converting the energy to light of a wavelength, which can be measured by inexpensive or easy to handle devices such as photomultiplier tubes (PMTs) or photodiodes. The photomultiplier tube amplifies the photon and converts the output light to an electric signal which can be used to measure the energy of the absorbed wave or particle in the scintillator. The intensity of the produced light in the scintillator is proportional to the energy deposited in the crystal.

Spectroscopy is the study of the interaction between radiation and matter as a function of energy (wavelength). It can be used to measure the energy spectra of a radiation field to detect the radiation types present in the environment. There are several methods for detecting different radiation particles and waves using scintillators. One common method consists in using a scintillator crystal which responds with different output pulse shapes for the radiation types of interest. This difference in the light signal can be used to discriminate among radiation types. Another technique to detect multiple radiation types consists in using several scintillator crystals which are coupled together and viewed with a single PMT. Each

crystal is selected to interact with a specific radiation type. The pulse shape at the output of the PMT determines in which layer(s) the interaction occurred.

The simultaneous detection of beta particles and gamma rays has broad ranging applications in nuclear non-proliferation, radioactive waste management, worker safety and homeland security. As a part of the Comprehensive Nuclear Test Ban Treaty, the International Monitoring Systems (IMS) has been established for monitoring xenon radio-isotope in the atmosphere to detect atmospheric or underground nuclear explosions (Farsoni et al. 2007). A radio-xenon detection system was designed by Farsoni and Hamby (Farsoni et al. 2007) at the Radiation Center, Oregon State University. The detector consists of a thin hollow disk as the xenon gas cell surrounded by two identical planar triple-layer phoswich detectors which provided a 3.4π solid angle for the gas. Fig. 1.1 shows the schematic of the two-channel triple-layer phoswich detector. The output pulse of each channel can belong to one out of seven possible cases, each of which indicates the interaction of radiation in one, two, or three layers of the detector.

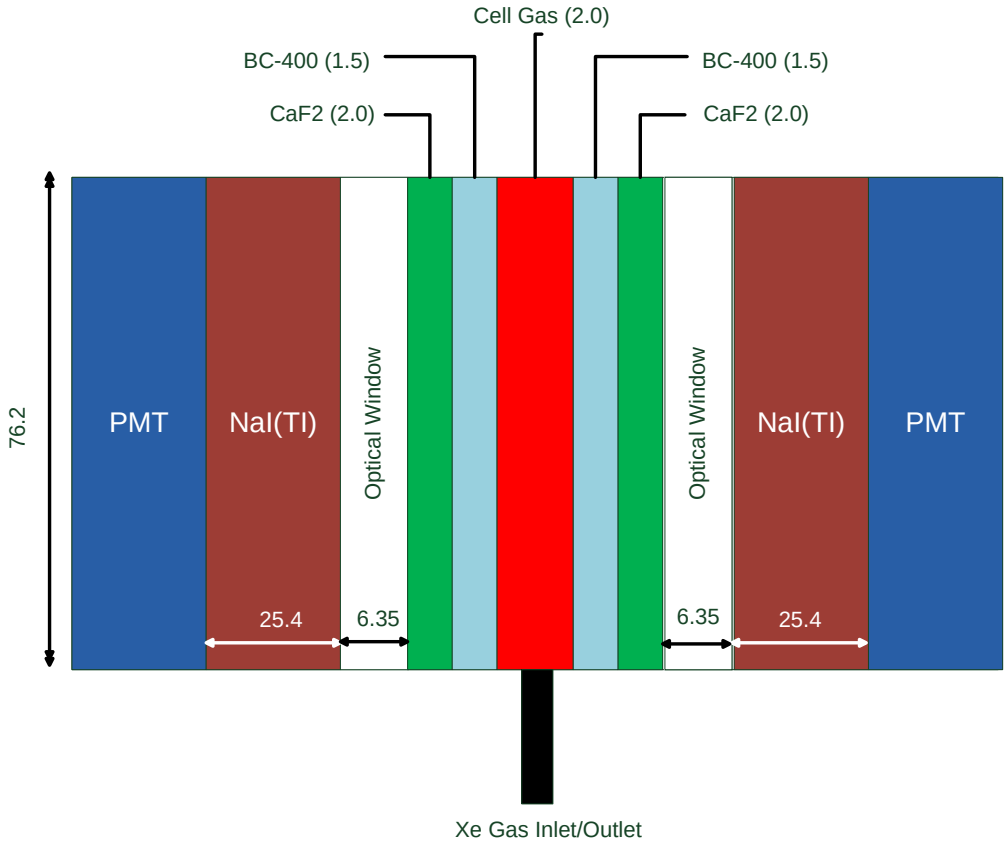

Fig. 1.1. The schematic arrangement of the two-channel phoswich detector. All dimensions are in mm. (Farsoni et al. 2007 ©)

In this thesis, a two-channel data acquisition board is designed and implemented for this detector structure. The system is composed of several stages. First, a signal conditioning and a digitizing board is designed and implemented on printed circuit board (PCB). Then, the digitized signal is sent to an FPGA, and a digital logic system triggers and records the input pulse and sends the data to a host computer. Finally, a digital signal processing algorithm in the host computer determines the origin of the interaction and measures the energy of the signal. Fig. 1.2 shows the schematic diagram of the designed data acquisition system.

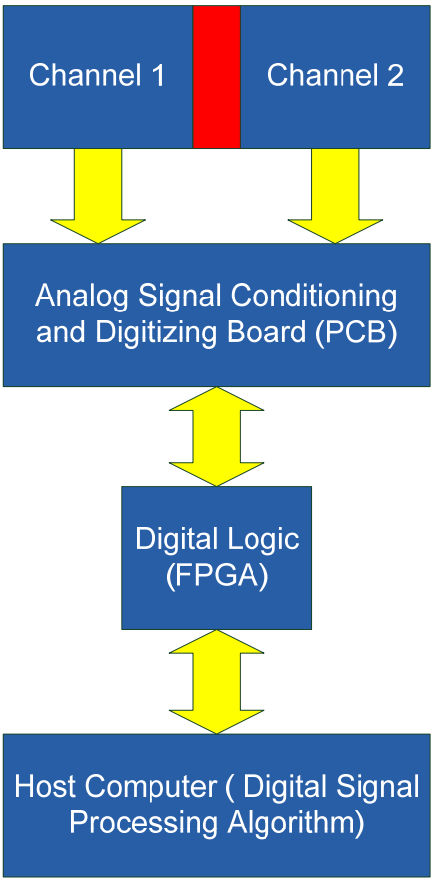

Fig. 1.2. The schematic diagram of the designed data acquisition system.

In the host computer, two novel digital algorithms for a single channel prototype are implemented in Matlab®. The first algorithm is based on the use of fuzzy logic to discriminate among possible cases. This method shows that using fuzziness in contrast to crispiness in data sets improves the discrimination results.

Most of the existing pulse shape discrimination (PSD) methods reported in the literature use time-domain features of the signal (e. g. time of flight or rise-time

measurement). However, there are no contributions to date regarding PSD methods operating in the frequency domain. Since the pulse shape at the output of the photomultiplier tube is a non-stationary signal, the conventional Fourier transform cannot capture relevant features for the discrimination process. The wavelet transform is an efficient tool to analyze non-stationary signals on a time-frequency scale.

The second method employs wavelet transform to extract important features of the input signal to discriminate between different pulse shapes. The implemented method using wavelet has superior performance over time-domain methods in terms of reliability and robustness to noise. Also, the wavelet method for this detector structure is more efficient than other time-domain methods in detecting multiple-absorptions in the layers of the detector. It can also detect unusually shaped pulses (mostly pile-up events).

A similar procedure based on the wavelet method for this detector structure is applied to another scintillation detection system for neutron/gamma discrimination. The system utilizes liquid scintillators to discriminate between gamma rays and neutrons. One of the applications of a neutron/gamma discrimination system is in cancer diagnosis and treatment.

2 Literature Review

2.1 Radiation Sources

There are four general types of radiation: fast electrons, heavy charged particles, electromagnetic radiation and neutrons. *Fast electrons* include (positive or negative) beta particles emitted in nuclear decay as well as energetic electrons produced by any other process. *Heavy charged particles* denote a category that encompasses all energetic ions with mass of one atomic mass unit or greater, such as alpha particles, protons, fission products, or the other products of many nuclear reactions. The *electromagnetic radiations of interest include* X-ray emitted in the rearrangement of electron shells of atoms and gamma rays that originate from transitions within the nucleus itself. *Neutrons* generated in various nuclear processes are often further divided into *slow neutron and fast neutron* subcategories (Knoll 2000).

The radiation energy measurement unit is the *electron-volt (eV)*, which is defined as the kinetic energy gained by an electron by its acceleration through a potential difference of 1 volt (Knoll 2000).

The most common sources of fast electrons are beta decay, internal conversion, and auger electrons. Heavy charged particle sources include alpha decay and spontaneous fission. The major sources of electromagnetic radiations are gamma rays following beta decay, annihilation radiation, gamma-rays following nuclear

reactions, bremsstrahlung, characteristic X-rays and synchrotron radiation (Knoll 2000).

2.1.1 Interaction of Fast Electrons

Fast electrons lose their energy at a lower rate compared to heavy charged particles. The specific energy loss due to ionization and excitation (the collisional losses) for fast electrons given in equation [2.1] is derived by Bethe (Knoll 2000).

$$-\left(\frac{dE}{dx}\right)_c = \frac{2\pi e^4 NZ}{m_0 v^2}\left(\frac{\ln(m_0 v^2 E)}{2I^2(1-\beta^2)} - (ln2)\left(2\sqrt{1-\beta^2} - 1 + \beta^2\right) + (1-\beta^2)\right) + \frac{\pi e^4 NZ}{4m_0 v^2}\left(1-\sqrt{1-\beta^2}\right)^2\right). \quad [2.1]$$

In Eq. [2.1] v is the velocity, N and Z are the density number and the atomic number of the atoms of the absorber material, respectively, m_0 is the electron rest mass, e is the electronic charge and $\beta \equiv \frac{v}{c}$.

Fast electrons may also lose their energy by radiative processes as well as by coulomb interactions (Knoll 2000). These radiative loses take the form of *bremsstrahlung* or electromagnetic radiation. The linear specific energy loss through this radiative process is

$$-\left(\frac{dE}{dx}\right)_r = \frac{NEZ(Z+1)e^4}{137 m_0^2 c^4}\left(4ln\frac{2E}{m_0 c^2} - \frac{4}{3}\right). \quad [2.2]$$

The total linear stopping power for electrons is the sum of the collisional and radiative losses:

$$\frac{dE}{dx} = \left(\frac{dE}{dx}\right)_c + \left(\frac{dE}{dx}\right)_r. \quad [2.3]$$

The mechanism whereby a beta particle (charged particle) loses its energy or is deflected from its original path, involves four principal types of interactions (Evans 1995):

1. *Inelastic collision with atomic electrons.* This is the predominant mechanism by which a beta particle loses kinetic energy in an absorber. As a result of such collision, one or more atomic electrons experience a transition to an excited state (excitation) or to an unbound state (ionization).
2. *Inelastic collision with a nucleus.* In this case, the incident beta particle experiences a deflection in the field of the nucleus. With this deflection, a quantum of radiation is emitted (bremsstrahlung photons), and a corresponding amount of kinetic energy is lost by the colliding particles.
3. *Elastic collision with nucleus.* The incident particle, in this case, is deflected but does not radiate, nor does it excite the nucleus. The incident particle loses only the kinetic energy required for conservation of momentum between the two particles.
4. *Elastic collision with atomic electrons.* An incident charged particle may be elastically deflected in the field of the atomic electrons of an atom. Such collisions are significant only for the case of very low-energy incident electrons (<100eV).

2.1.2 Interaction of Gamma Rays

There are three major mechanism types through which gamma rays may interact with matter: photoelectric absorption, Compton scattering, and pair production. In all mechanisms, the transfer of the gamma ray photon energy to electron energy can be partial or complete (Knoll 2000).

In the photoelectric absorption process, the photon completely disappears and an energetic photo-electron is rejected by the atom from one of its bound shells. In addition, an ionized absorber atom with a vacancy in one of its bound shells is also created. This vacancy is quickly filled through capture of a free electron from the medium and/or re-arrangement of electrons from other shells of the atom and one or more characteristic X-ray photons may also be generated.

The interaction process of Compton scattering takes place between the incident gamma ray photon and an electron in the absorbing material.

If the gamma ray energy exceeds twice the rest mass energy of an electron (1.02 MeV), practically several MeV, the process of pair production is possible. In the interaction (which must take place in the coulomb field of a nucleus), the gamma ray photon disappears and is replaced by an electron-positron pair. These pairs escape in

exactly opposite directions. This phenomenon is used in biomedical imaging devices like PET (positron emission tomography) scanners.

2.2 Scintillation Detection Principles

2.2.1 Scintillation Materials

Scintillators are materials that interact with radiation materials and produce a signature visible or ultraviolet photon. This phenomenon has been used to detect radiation sources for a long time. A good scintillator is transparent to its own light, possesses fast light-emission times, has a degree of scintillation efficiency, and has a linear light emission property and good optical qualities (Knoll 2000). There are different types of scintillators: organic scintillators (crystals, thin films, liquids) and inorganic scintillators (crystals like NaI, CsI, CaF2).

The excitation and de-excitation process in organic scintillators can be described adequately by simple exponential rise and decay times:

$$I = I_0(e^{-\frac{t}{\tau}} - e^{-\frac{t}{\tau_1}}), \qquad [2.4]$$

where τ is the decay time constant and τ_1 is the excitation time constant. Organic scintillators are usually used for electron or beta spectroscopy (Knoll 2000).

The light emission from inorganic crystals is based on excitation and de-excitation of energy states in the lattice structure. Excited states are all formed at

once and then decay exponentially. Although inorganic scintillators have a better energy linearity compared to organic ones, they have longer decay times. Since inorganic materials have a higher Z than the organic ones, they are used in low-energy gamma interface and cause backscatter with incident beta particles.

In order to detect the light output of scintillation materials, a photomultiplier tube (PMT) or a photodiode is used to amplify and convert the light to an electrical signal. The amplification in PMT is usually on the order of 10^6 to 10^7. The charge (voltage) at the anode of the PMT is related to the energy of input light which is related to the energy of the radiation source.

The output pulse shape of PMT which is the result of a scintillation event depends on the scintillation time constant and also on the time constant of the anode circuit. The voltage pulse at the anode is given by (Knoll 2000):

$$V(t) = \frac{1}{\tau - RC} \times \frac{\tau Q}{C} \left(e^{-RCt} - e^{-\tau t}\right), \qquad [2.5]$$

where τ is the scintillator decay time constant, RC is the anode circuit time constant, and Q is the total charge collected over the entire pulse.

2.2.2 Phoswich Detectors

A Phoswich (phosphor sandwich) detector is a combination of two or three different scintillators optically coupled together and viewed with a single

photomultiplier tube (PMT). Each scintillator layer has a different light output characteristic and is chosen to interact with a specific radiation type. The light output of the PMT has to be subsequently processed to interpret the pulse information and detect the radiation type.

The purpose of designing a phoswich detector is the simultaneous detection of different radiation types or the detection of a desired radiation in a mixed field containing other radiation types in the background (Farsoni 2007). Phoswich detectors have a variety of applications. One of the recent uses is in radio-xenon monitoring for underground nuclear explosions (Hennig et al. 2007).

One of the advantages of using phoswich detectors is independent measurement of the energy deposited in each scintillator without the need for a second PMT (Farsoni and Hamby 2005).

2.3 Pulse Shape Discrimination

Pulse shape discrimination (PSD) refers to the method differentiating between different pulse shapes which may result in the absorption of different radiation types in a single scintillator (single layer scintillator detectors) or different radiation types in different layers of a phoswich detector. Most of the PSD methods in phoswich detectors are based on the different decay time constants of each layer. Since each

layer is chosen to interact with a specific radiation type, PSD determines which type of radiation has been absorbed in the detector.

The performance of the PSD methods is usually measured by the FWHM (full width at half of maximum which shows the percentage of the width of the spectrum peak at half of its maximum divided by the peak energy) or the error rate which shows the amount of misclassification of a radiation type as another type.

Traditionally, pulse shape discrimination and radiation spectroscopy was carried out by analog modules. Several modules had to work together to derive the energy spectrum of a radiation material. With the advance of fast digitizing components and computer interface systems, digital signal processing techniques have become popular in radiation detection. The use of digital techniques is more efficient, cost-effective, and flexible compared to traditional analog methods. In a digital pulse analyzing system, the output pulse of a PMT is first digitized using fast digitizing components. Further processing is carried out online or offline in a digital pulse processor. The data can also be stored in a memory for offline processing.

There exist different pulse shape discrimination methods for single-layer scintillator detectors. Most of the existing methods use time-domain analysis for PSD. The most popular methods are the constant fraction discrimination (CDF) method, the rise-time discrimination (RTD) method, the constant-time discrimination (CTD) method, and the charge comparison (CC) method (Chandrikamohan et al. 2007). These methods are mostly designed for single layer detectors or double-layer

phoswich detectors and they are not efficient for triple-layer phoswich detectors. Based on the structure of the phoswich, the PSD method for each detector configuration can be different from the other ones (Farsoni et al. 2007).

Several configurations of two or three layer phoswich detectors for different applications have been implemented, tested, and analyzed in the literature. Usuda et al. (1994, 1997) developed many phoswich detectors for simultaneous detection of alpha, beta (gamma), thermal and fast neutrons. Pulse-height and rise-time of the signal were used to discriminate between different pulse shapes. However, this detector could not achieve good separation between beta and gamma interactions and they were clustered in the same group.

White and Miller (1999) developed a three-crystal phoswich detector (then analyzed by Childress and Miller (2002)) for simultaneous alpha/beta/gamma spectroscopy. A two-step method was used to discriminate between pulse shapes. First, the rise-time (representing the time from the beginning of the pulse to its peak) of each pulse was used to discriminate between gamma rays and other radiation types (beta and alpha). The separation of beta and alpha particles was carried out by finding the correlation of the incoming pulse with a reference signal. The pulse was classified as belonging to the category which had the largest correlation coefficient. In this method, the radiation interaction is assumed to be in only one layer of the detector. So other possible cases where interaction may occur in two or three layers were ignored. Another disadvantage of this method is the sensitivity of the reference

pulse shape to temperature changes because the scintillator's decay time is a function of temperature (Knoll 2000). Consequently, for the spectroscopy applications where the environment temperature is not fixed during measurement (e.g. stand-alone devices for radioactive xenon monitoring) the correlation method is not efficient.

Bardelli et al. (2002) in the FIASCO experiment (Casini et al. 2000 and Piantelli et al. 2002), used a digital technique for identification of fast charged particles with a triple-layer phoswich detector. A digitizing board was designed and implemented and two digital algorithms were used for particle identification on the sampled data. The first pulse shape analysis was based on the integration of the anode signal over three different time windows where each window was representative of energy absorption in one layer. The second method was based on a linear fitting of the anode signal to a combination of three signals, each showing the output waveform of a scintillator layer. The digital algorithm was compared with the standard analog method, and the digital algorithm outperformed the analog one. However, temperature variations may degrade the fitting algorithm performance, and it is not an efficient way of performing pulse shape discrimination in applications where the experiment environment temperature is not fixed.

Farsoni and D. Hamby (2007) designed, and constructed a triple-layer phoswich detector and electronic read-out system for simultaneous beta and gamma spectroscopy. The structure of the triple-layer phoswich detector is shown in Fig. 2.1.

The first layer is a plastic scintillator (BC-400) with a very fast decay constant (2.4 ns), and the second layer is an inorganic crystal (CaF2 (Eu)) with a very slow decay time (930 ns). Both materials are used for stopping beta particles with energies up to 3.2 MeV. The phoswich detector is designed such that an incident beta must deposit energy in the first layer, or in both the first and second layers, for a pulse to be recorded as a beta-induced pulse. The third layer is an inorganic scintillator (NaI(TI)) with a 230ns light decay constant. A quartz layer separates the third layer from second layer because plastic scintillators cannot be completely dried and would gradually destroy the performance of the third layer (Farsoni et al. 2007).

Compton scattering is the prominent interaction mechanism from incident gamma-rays in the first two layers. Since the second layer is thick enough to accommodate electrons up to 3.2 MeV, the unwanted events (mostly Compton scattering) in the beta-side of the detector are comparable to that of the gamma-side, the third layer. However, since common beta particles have much shorter mean free paths than gamma rays in scintillation materials, events in the first layers can be used with the second layer, and so the Compton events can be distinguished quite easily (Farsoni et al. 2007).

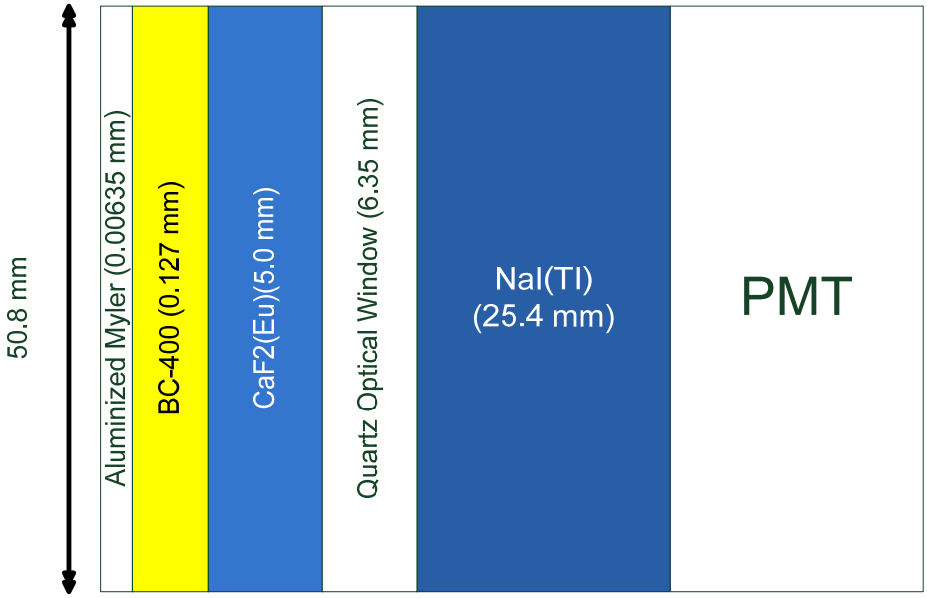

Fig. 2.1. The structure of the triple-layer phoswich detector.

In order to discriminate between pulse shapes and extract the energy spectrum, seven possible scenarios were studied. One of these scenarios is related to the gamma-ray absorption and two other scenarios show beta absorption. The other four scenarios were rejected because the signal information could not be extracted. Fig. 2.2 shows the structure of the detector used by Farsoni et al. (2007) and the possible scenarios.

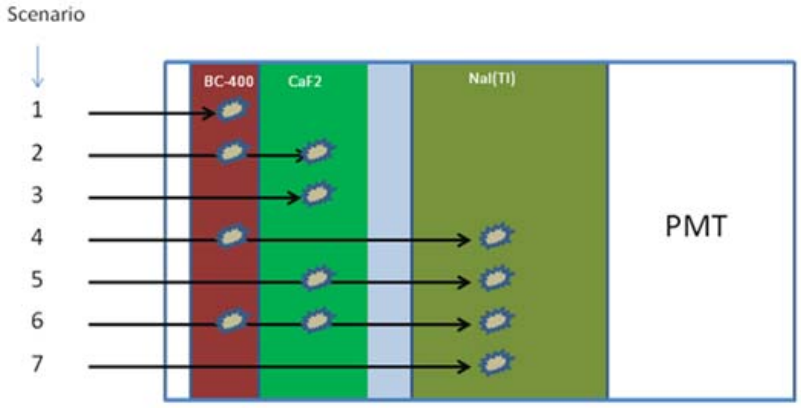

Scenario	Scintillation Layers			Total Probability (%)*		Pulse Recorded as:
	BC-400	CaF2	NaI:Tl	Gamma	Beta	
1	×			0.35	12.32	Beta
2	×	×		0.07	81.70	Beta
3		×		14.40	4.60	Rejected
4	×		×	0.06	0.08	Rejected
5		×	×	2.65	0.03	Rejected
6	×	×	×	0.01	0.57	Rejected
7			×	12.87	0.00	Gamma

Fig. 2.2. The possible interaction scenarios in the triple-layer phoswich detector.

After digitizing the signal and sending the waveform from the FPGA to the host computer, two timing features of the signal, fast ratio and slow ratio, were extracted and were used for pulse shape discrimination. First the fast ratio of the signal was compared with a threshold, and if it was larger than that, it was classified as beta. If the pulse was not classified as beta, the slow ratio was measured and compared to a

threshold. If the ratio was larger than a threshold, it would be classified as gamma. If none of the conditions was true, the pulse was rejected and classified as “unknown”. One of the disadvantages of the method employed by (Farsoni et al. 2007) is that, if the signal is the result of an absorption in the 1^{st} and 3^{rd} layer, it would be misclassified either as beta or as gamma. If this device is to be used in a mixed radiation field, the algorithm is not efficient in discriminating between single-type and multiple-type radiations. This method is not effective in detecting the simultaneous absorption in the 1^{st} and 2^{nd} layer and some of these pulses are rejected because they cannot be analyzed.

However, there are no contributions to date regarding PSD methods operating in the frequency-domain. Since the pulse shapes at the output of the photomultiplier tube are non-stationary signals, their analysis using conventional Fourier transform cannot capture relevant features. The wavelet transform (Mallat 1989 and Daubechies 1988) is an efficient tool to analyze non-stationary signals on a time-frequency scale (A. Kareem et al. 1993). The wavelet transform has gained great popularity in digital signal processing and is widely used in different engineering and medical applications (Fargo et al. 1992, Wahl et al. 1993). The time-frequency scale of the wavelet transform is not uniform over the entire domain, thus allowing for multi-scale characteristics with the scale being adjustable according to the signal features.

3 Materials and Methods

3.1 Data Acquisition System

3.1.1 Overview

The function of a spectrometry system is to convert the electrical (charge) pulses originating at the output of the radiation detector into voltage pulses and then, to obtain their energy distribution function as accurately as possible (Simoes et al. 1999). Most scintillation detection systems use analog modules for radiation spectroscopy. With the recent development of fast analog to digital converters and digital processors, digital signal processing methods have gained popularity in radiation spectroscopy. Compared to analog modules, digital devices are more compact and cost-effective, and post-processing of data is much easier (Farsoni et al. 2007).

The data acquisition system designed in this project is composed of two parts: an analog signal conditioning module and a digital logic system. The analog board was designed and implemented in the Instrumentation Lab at Radiation Center, Oregon State University, and the FPGA board is a commercial device.

The analog board was designed for a two-channel spectroscopy system. The block diagram of the acquisition system is shown in Fig. 3.1. The output of each detector (and PMT) is sent to the analog circuit board. After sampling and digitizing,

the digital signal is sent to the FPGA. A digital logic system is designed and implemented on FPGA which triggers and records the input. When a pulse is completely recorded, the captured pulse is transmitted to the host computer for further processing. In the host computer, a digital pulse shape discrimination algorithm determines which class this pulse belongs to and measures its energy and plots the histogram.

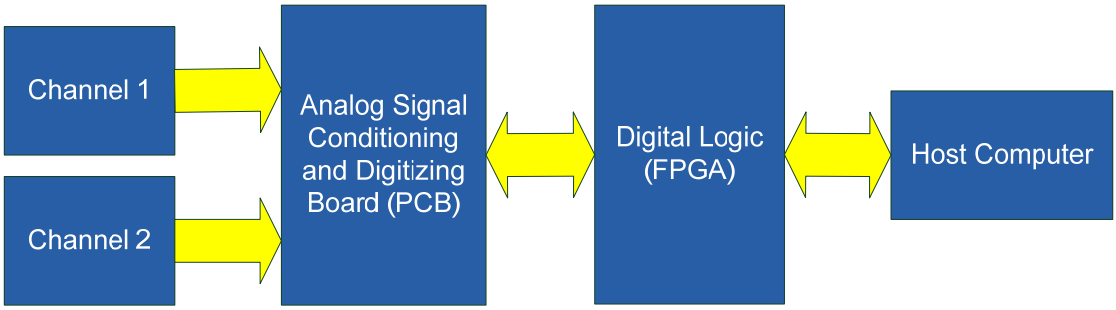

Fig. 3.1. The block diagram of the data acquisition system.

The FPGA board used in this application was a commercial device from Opal Kelly (Fig. 3.2), with a Xilinx Spartan3 FPGA, and USB interface to the host computer.

Fig. 3.2. The FPGA board from Opal Kelly®

The mechanical drawing of the top and bottom of the board is shown in Fig. 3.3. The connection between the analog part and the digital part was carried out by two connection tags which were implemented on the PCB board (Fig. 3.4).

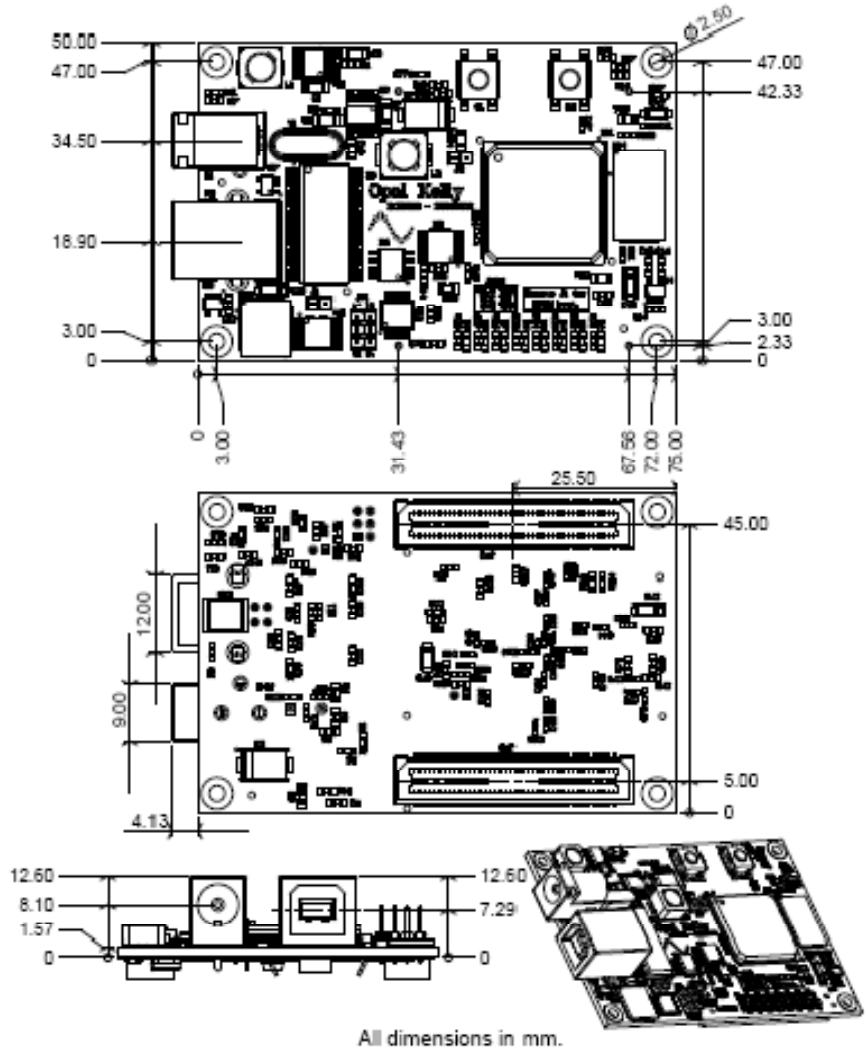

Fig. 3.3. The mechanical drawing of the FPGA board.

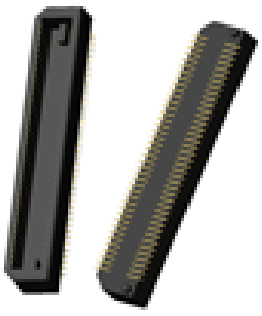

Fig. 3.4. Connection tags.

3.1.2 Analog Circuit Board Design

The schematic of the analog circuit board is shown in Fig. 3.5.

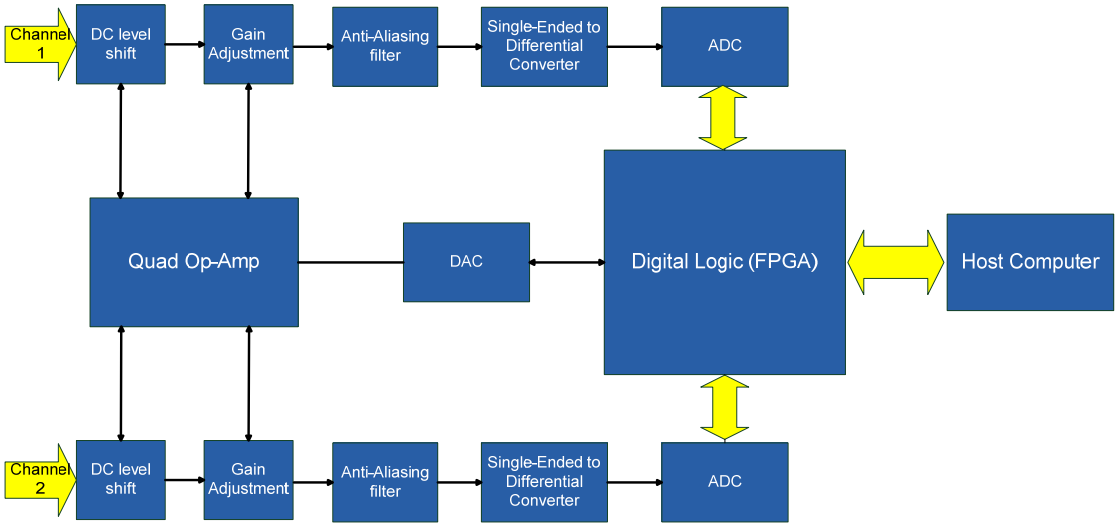

Fig. 3.5. The block diagram of the analog board.

This board has different stages. The first stage performs base-line correction and dc level shift using a simple op-amp structure. The second stage is a variable gain amplifier which tunes the peak to peak amplitude of the input signal to the input range of the analog to digital converter (ADC). The gain and the offset are controlled in the FPGA by a digital to analog converter (DAC).

After the dc-level shift and gain correction, a 3rd order anti-aliasing filter is implemented. In this application, a Bessel filter is chosen due to constant delay compared to Butterworth and Chebychev filters. The 3-dB cut-off frequency edge of the filter is chosen to sample the data at 250MSPS rate. For a higher performance the input signal of and ADC is recommended to be differential rather than single-ended. In order to change the single-ended signal to a differential signal, a buffer is used. This stage improves the common mode rejection ratio and enhances the performance of the ADC

The final stage is a 250 MSPS ADC which samples and sends the input signal to the FPGA. The ADC which is used in this application is AD9230 (12-bit, 250 MSPS, 1.8V). This device is available in 56-pin LFCSP (Lead Frame Chip Scale Package). The other components used on this board include voltage regulators and clock translators. The schematic capture of the analog board is plotted in Fig. 3.6 and Fig. 3.7.

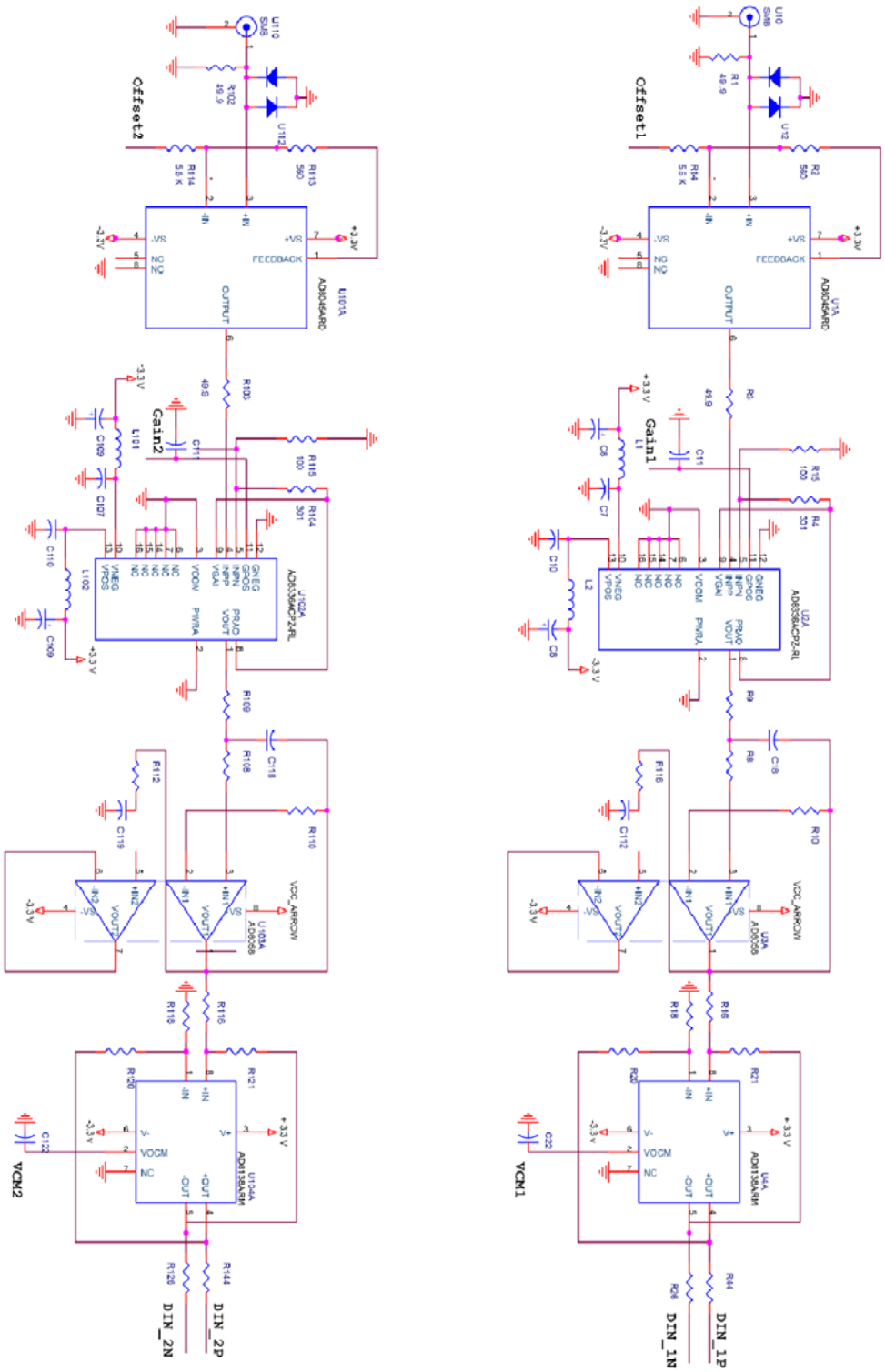

Fig. 3.6. The schematic of the circuit board (Part 1).

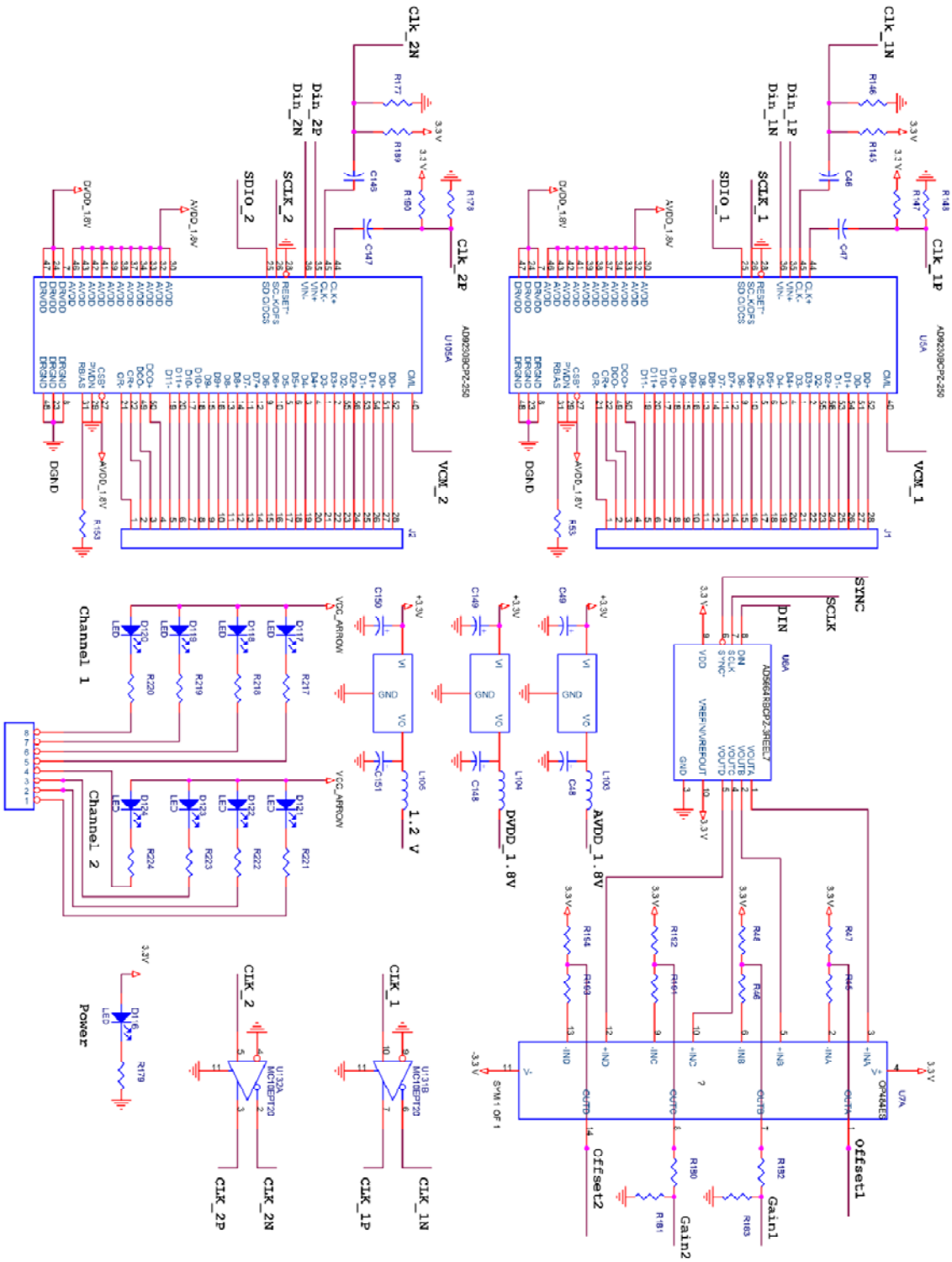

Fig. 3.7. The schematic of the analog circuit (Part 2).

The analog design was implemented on a 3in X 3in 6-layer printed circuit board. The different layers of the board are shown in Fig. 3.8 to Fig. 3.13.

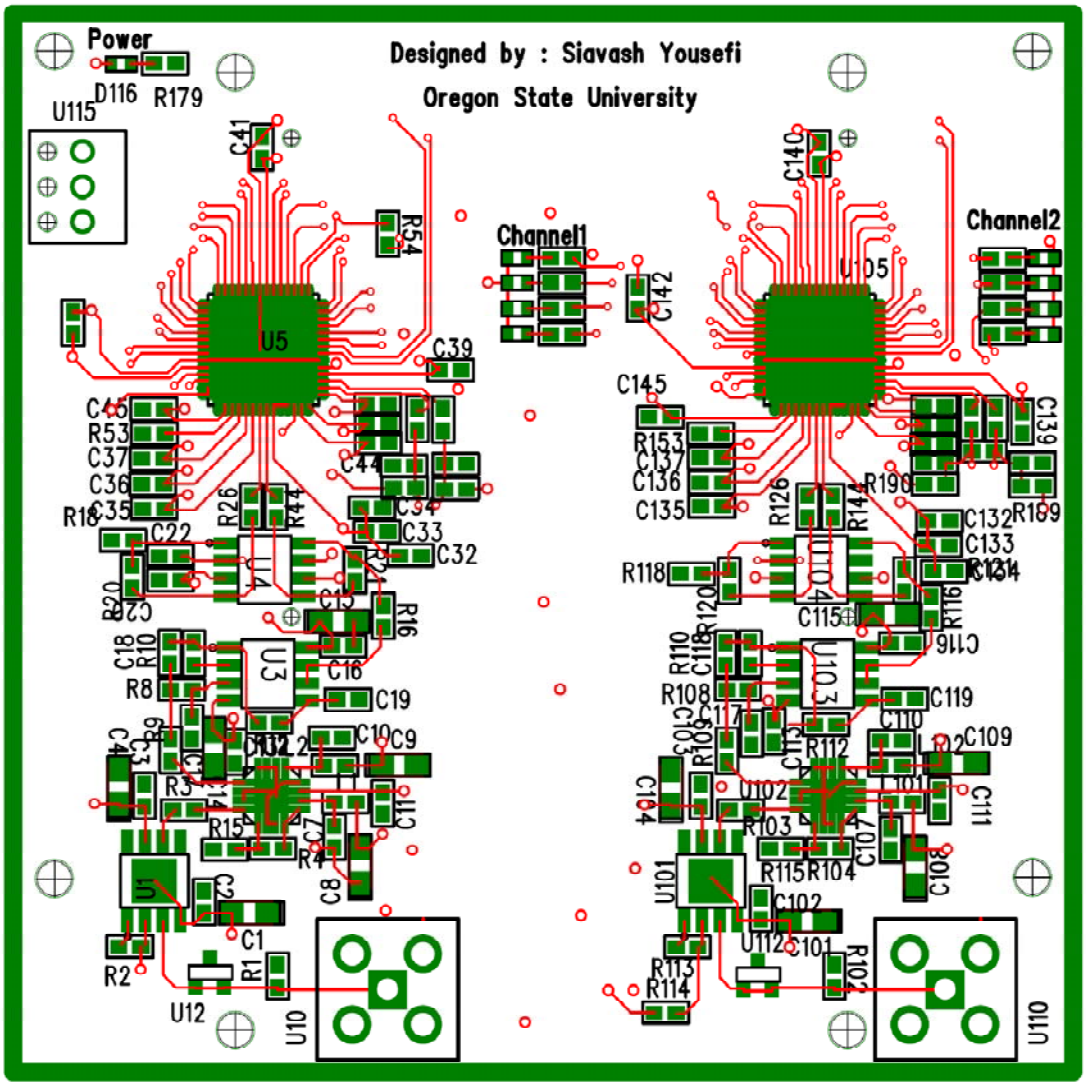

Fig. 3.8. The top layer of the PCB.

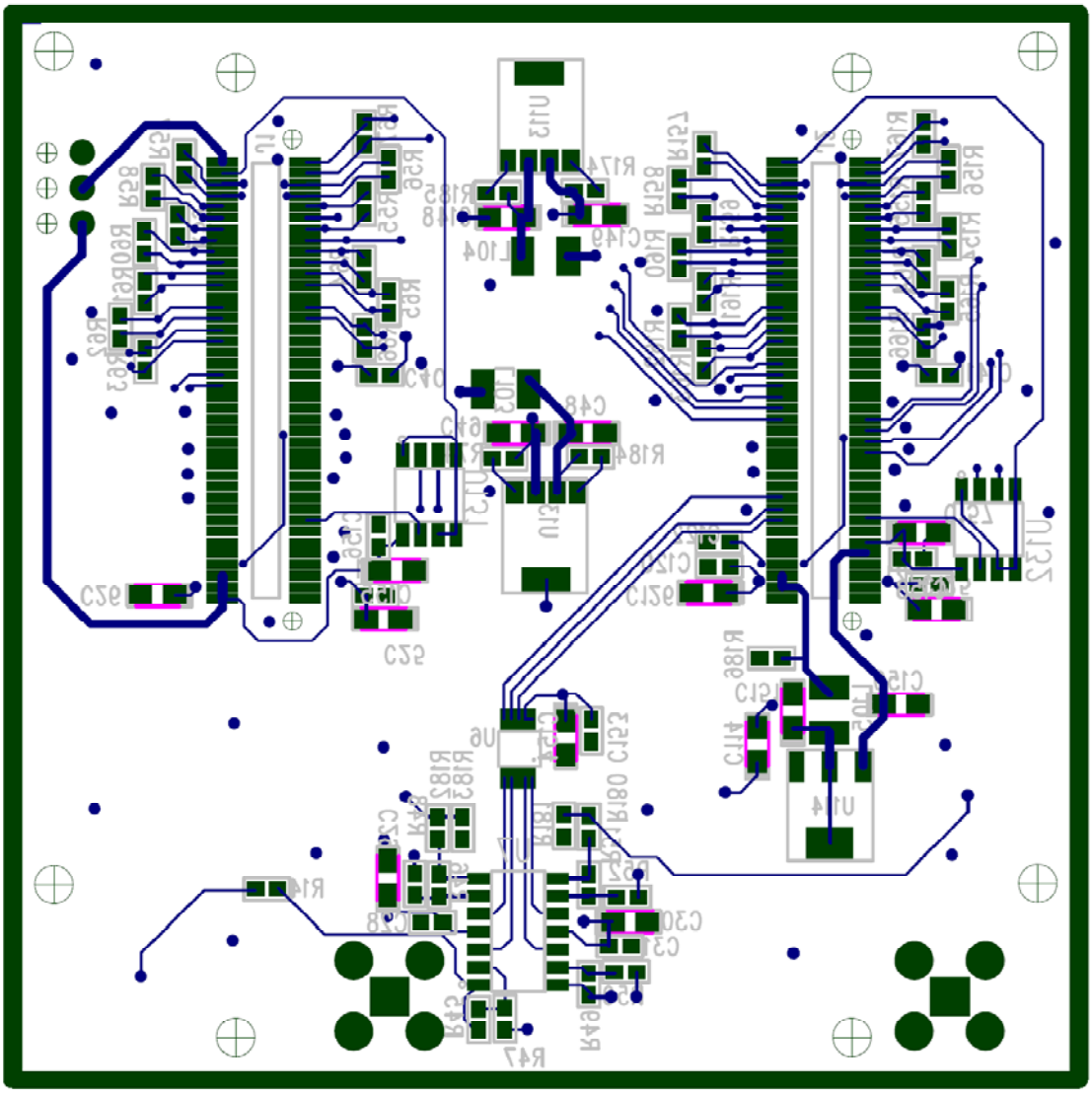

Fig. 3.9. The bottom layer.

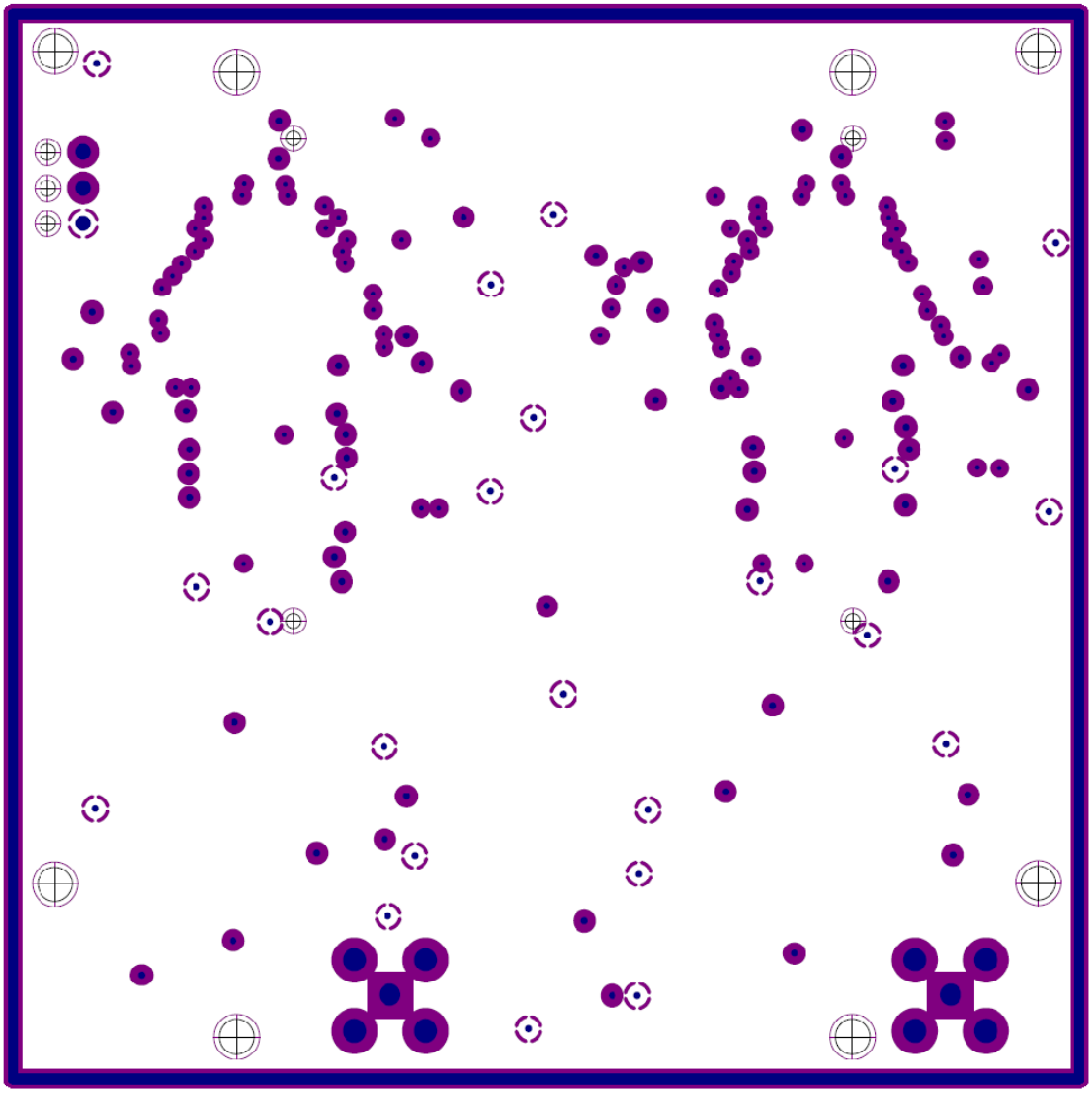

Fig. 3.10. The 1st inner layer (+VCC).

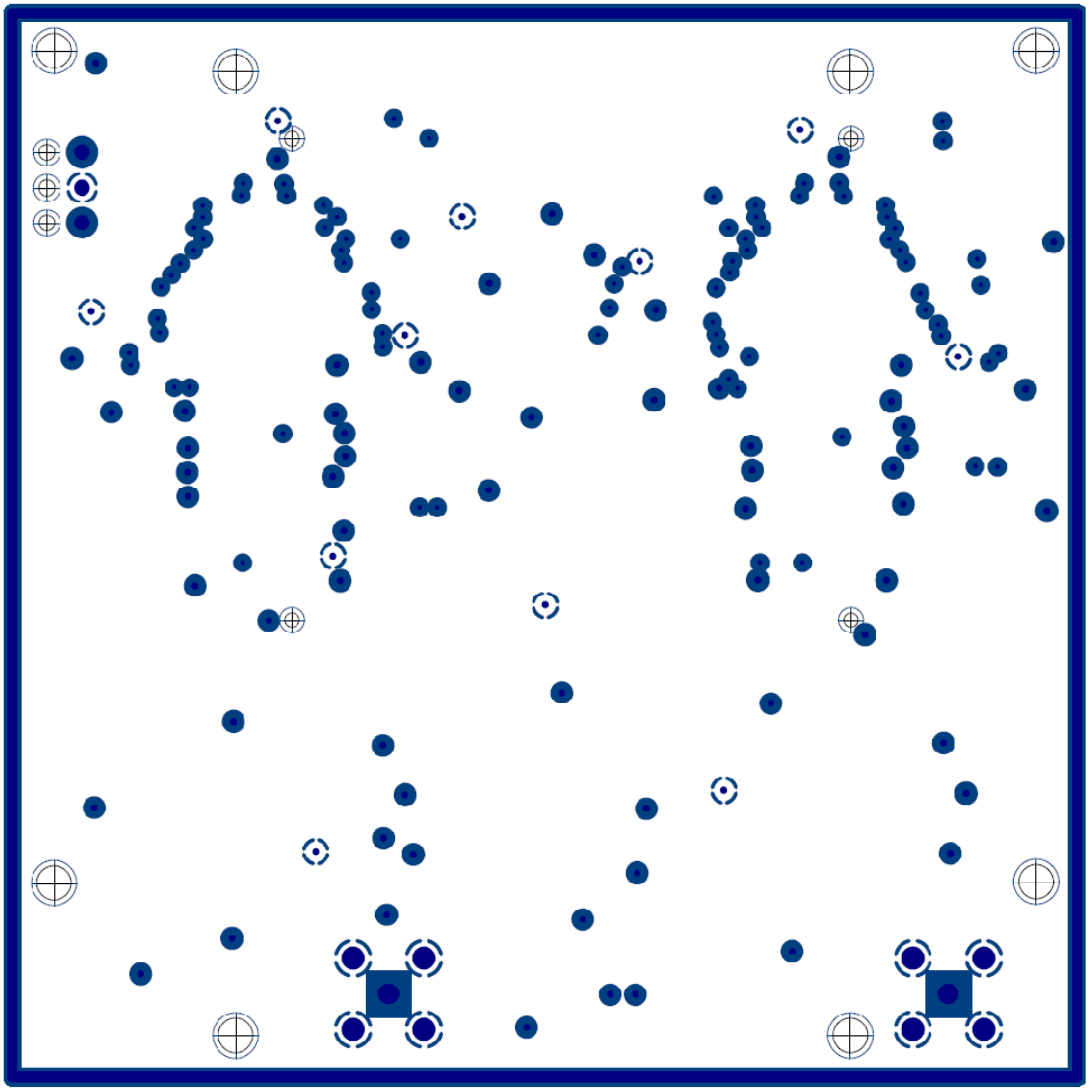

Fig. 3.11. The 2nd inner layer (Ground plane).

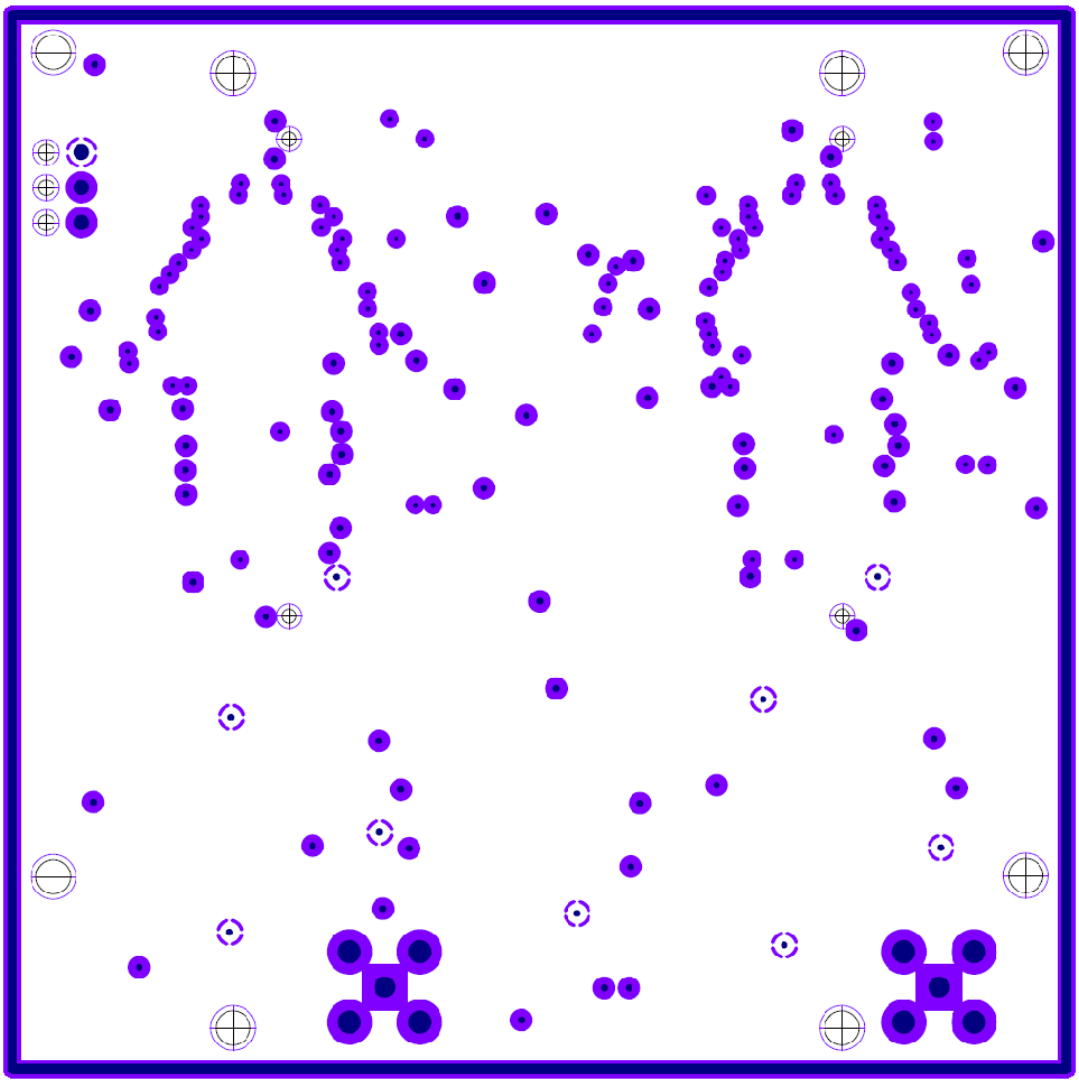

Fig. 3.12. The 3rd inner layer (-VCC).

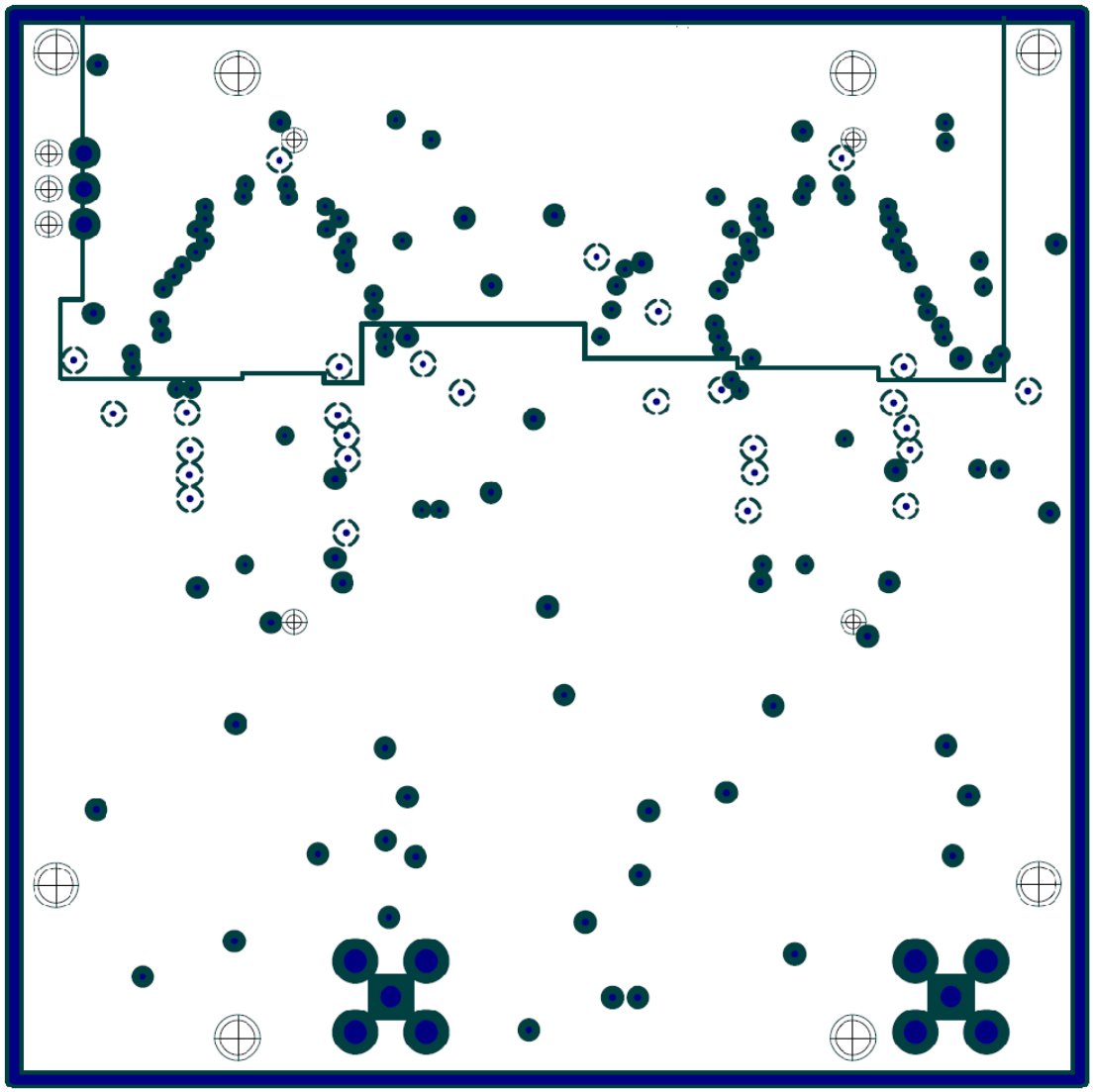

Fig. 3.13. The 4th inner layer (1.8V analog and 1.8V digital).

Table 3.1 shows the detailed list of the materials used in this design.

Table 3.1. The list of materials and components which were used on the board.

Item	Reference Designator	Device	Package	Description	Part Number
1	U1, U101	AD8045	SOIC_8 Exposed Paddle	Op Amp	
2	U2, U102	AD8336	LFCSP_16	Variable Gain Amplifier	
3	U3, U103	AD8058	SOIC_8	Dual Op Amp	
4	U4, U104	AD8138	SOIC_8	Differential Op Amp	
5	U5, U105	AD9230	LFCSP_56	250 MSPS ADC	
6	R1, R3, R102, R103	Chip Resistor	0603	49.9 Ω	
7	R2, R113	Chip Resistor	0603	560 Ω	
8	R14, R114	Chip Resistor	0603	5.6 KΩ	
9	R4, R104	Chip Resistor	0603	310 Ω	
10	R9, R109	Chip Resistor	0603	931 Ω	
11	R8, R108	Chip Resistor	0603	887 Ω	
12	R10, R110	Chip Resistor	0603	324 Ω	
13	R12, R112	Chip Resistor	0603	1 KΩ	
14	R16, R 116, R21, R121,	Chip Resistor	0603	499 Ω	

	R20, R120				
15	R18, R118	Chip Resistor	0603	330 Ω	
16	R44, R26, R144, R126	Chip Resistor	0603	33 Ω	
17	R54-R67, R154-R167	Chip Resistor	0603	100 Ω	
18	R53, R153, R45-R52, R184, R74, R174, R185	Chip Resistor	0603	10 kΩ	
19	R180, R182	Chip Resistor	0603	56 KΩ	
20	R181, R183	Chip Resistor	0603	15 KΩ	
21	R179, R217-R224	Chip Resistor	0603	150 Ω	
22	C1, C4, C101, C104, C9, C109, C14, C114, C19, C119, C25, C26, C125, C126, C155, C157, C49, C48, C149, C148, C30, C29, C150	Tantalum Capacitor	ACASE	10 µF	
23	C2, C3, C102, C103, C7, C10, C110, C111, C107, C13, C16, C113, C116,	Chip Capacitor	0603	0.1 µF	

	C20, C21, C120, C121, C32-C47, C132-C147, C153, C158, C156, C28, C31				
24	C17, C117	Chip Capacitor	0603	1 pF	
25	C18, C118	Chip Capacitor	0603	1.8 pF	
26	C19, C119	Chip Capacitor	0603	1.5 pF	
27	C151	Tantalum Capacitor	ACASE	33 µF	
28	U10, U110	SMA Connector			
29	U12, U112	Schottkey Diode	SOT323		ZUMD70-40
30	U6	Quad DAC	MSOP (RM-10)		AD5664R
31	U7	Quad Op Amp	SOIC (R-14) Narrow Body		OP484
32	U131, U132	Clock Translator (LVPECL to LVDS)	SOIC-8 NB CASE 751-07		MC100EPT20
33	U13, U113	1.8V LDO Voltage Regulator	SOT 223-5	3.3V to 1.8V	LP3872

34	U114	1.2V LDO Voltage Regulator	4-Lead SOT-223	3.3V to 1.2V	FAN1112
35	L1, L2, L101, L102	Inductor		Ferrite Bead	BLM18BA750SN1D
36	L103, L104, L105	Inductor	3.2mm X 2.5 mm X 1.6mm	Ferrite Bead	Digi-key P9811CT-ND
37	D117-D124	LED	0603	Green	
38	D116	LED	0603	Red	

3.2 Pulse Shape Discrimination Methods

3.2.1 Fuzzy Method

The digital pulse shape discrimination method we advance is composed of the following steps. First, a de-noising algorithm is applied to the data. Then, important features for pulse shape discrimination (PSD) are extracted. These features are inputs to the fuzzy interface system. Finally, a decision-making unit decides whether the signal can be sent for energy measurement and spectroscopy or should be rejected. The block diagram of the system is shown in Fig.3.14.

Fig. 3.14. The block diagram of the fuzzy method.

3.2.1.1 Wavelet De-nosing

Since the PMT anode signal is very noisy and timing features highly depend on the signal at specific times, a de-noising algorithm is required. There exist different digital de-noising methods (e. g. moving average filters, median filters) depending on the application. In this application, smoothing filters are not appropriate because the signal contains a sharp portion associated with the absorption in the first layer (fast component). In order to de-noise the signal and avoid loss of important information, an approach based on the wavelet transform (Mallat 1989) is used.

The wavelet transform is an interesting signal processing method and is widely used in different engineering and medical applications (Farge 1992 and Wahl et al. 1993). The time-frequency scale of the wavelet transform is not uniform over the entire domain, thus allowing for multi-scale characteristics with the scale being adjustable according to the signal features. C. Shiguo et al. (2004) used wavelet de-noising to process the sampled data obtained from a gas detector and improved its SNR effectively.

In our application, a 5-level de-noising algorithm based on 'sym8' wavelet functions was used. Fig. 3.15 shows the noisy signal (a) and the de-noised signal (b) of a typical pulse shape captured from ^{90}Sr/Y which is the result of beta absorption in the 1st and 2nd layer of the detector. Note that the fast component of the signal, which is due to the interaction in the first layer of the phoswich detector, is preserved.

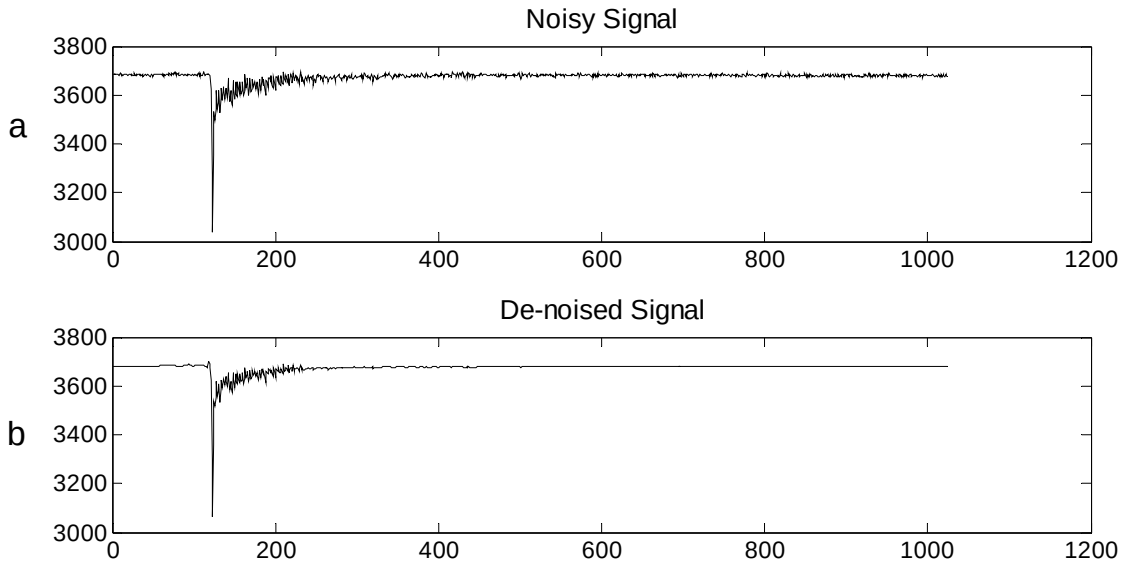

Fig. 3.15. (a) Noisy signal. (b) De-noised signal using a 5-level de-noising algorithm based on "sym8" wavelet functions.

To compare the wavelet de-noising performance with smoothing filters, the de-noised signal using a 5-point moving average filter is shown in Fig. 3.16. It can be noticed that the timing features of the signal related to the fast component are smoothed by applying a moving average filter but are mostly preserved using wavelet

de-noising. The signal is a typical ^{90}Sr/Y waveform which is the result of beta absorption in the 1st and 2nd layer of the detector.

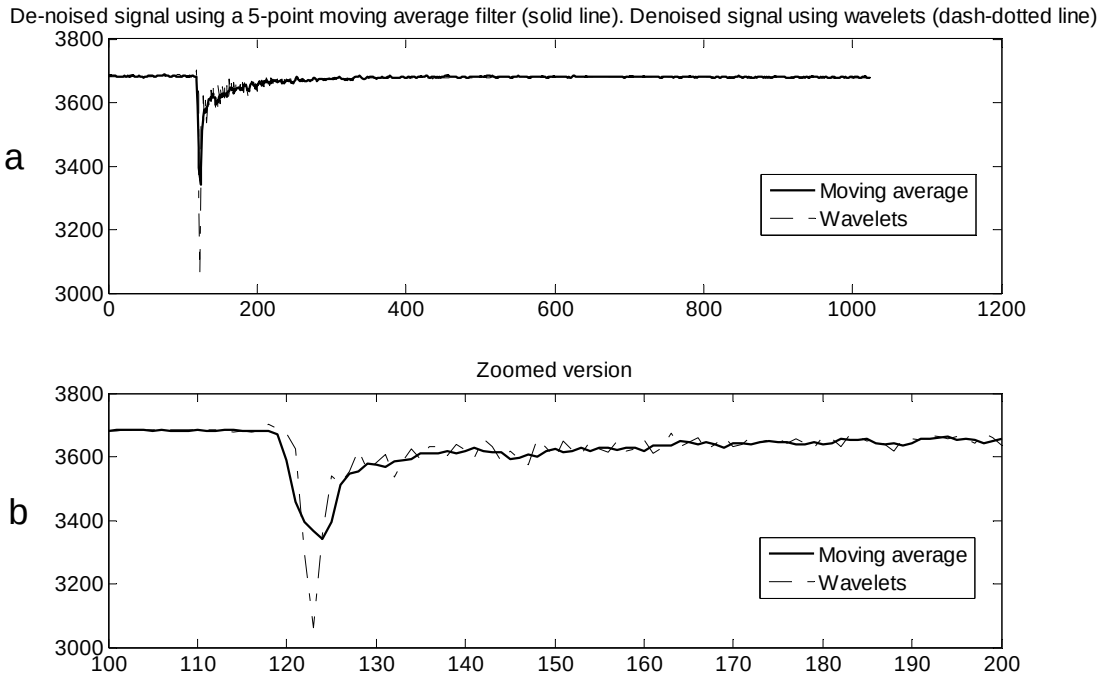

Fig. 3.16. (a) ^{90}Sr/Y Wavelet de-noising (dash-dotted line) and de-noising using a 5-point moving average filter (solid line). (b) The bottom plot is a zoomed version of the top plot.

3.2.1.2 Feature Extraction

The output waveform of the triple-layer phoswich detector, after the peak, can be modeled as the linear combination of three exponential decays, each one

showing the absorption in one layer of the detector (Knoll 2000 and Bardelli et al. 2002). Since the intensity of the fluorescence of the scintillator decays exponentially (Birks 1964), a mathematical model of the principal components of the input signal, which stem from the absorption in the three layers of the phoswich detector, can be expressed as

$$s(t) = K_1 \times A_1 \times e^{-t/\tau_1} + K_2 \times A_2 \times e^{-t/\tau_2} + K_3 \times A_3 \times e^{-t/\tau_3} . \qquad [3.1]$$

Depending on the layer(s) in which the absorption occurred, constants K1, K2, and K3 can take on the value zero or one. A1, A2, and A3 are constants related to the energy absorption in each scintillator layer. The τ values are the decay constants of each scintillator layer.

In order to discriminate among seven scenarios, at least three features are chosen. According to the possible shapes of the signal and the different scenarios which may arise, the features in the block diagram of Fig. 3.14 are extracted using the following algorithm:

$$d_1 = abs\left(\frac{\left(\left(S(t_{peak}) - S(t_{peak}+30ns) \right) \right)}{S(t_{peak})} \right), \qquad [3.2]$$

$$peak_{ratio} = abs\left(\frac{s(t_{peak}+30ns)}{s(t_{peak})} \right) \qquad [3.3]$$

$if\ peak_{ratio} < peak_{threshold}\ and\ d1 < d_{threshold}\ then$

$$d_2 = abs\left(\frac{s(t_{peak}+30ns)-s(t_{peak}+300ns)}{1.4\times\left(s(t_{peak}+30ns)\right)}\right), \quad [3.4]$$

$$d_3 = abs\left(\frac{s(t_{peak}+1200ns)-s(t_{peak}+3500ns)}{1.4\times\left(s(t_{peak}+30ns)\right)}\right), \quad [3.5]$$

else

$$d_2 = abs\left(\frac{s(t_{peak}+30ns)-s(t_{peak}+300ns)}{s(t_{peak})}\right), \quad [3.6]$$

$$d_3 = abs\left(\frac{s(t_{peak}+1200ns)-s(t_{peak}+3500ns)}{s(t_{peak})}\right). \quad [3.7]$$

First feature d1 determines if the input signal s(t) contains a fast component (fast exponential decay in the first layer of the detector BC400). Feature d3 determines if the signal contains a slow component (slow exponential decay in the second layer of the detector (CaF2)). Feature d2 is used to discriminate among other possible cases and is mostly used to indicate the absorption in the 3rd layer. The condition for the peak ratio is for the cases where the sharp point of the signal is much larger than the rest of the signal. Thus it prevents the misclassification of the slow portion of the signal. Fig. 3.17 shows the time features of the signal extracted from a typical synthetic waveform which contains the absorption in all three layers.

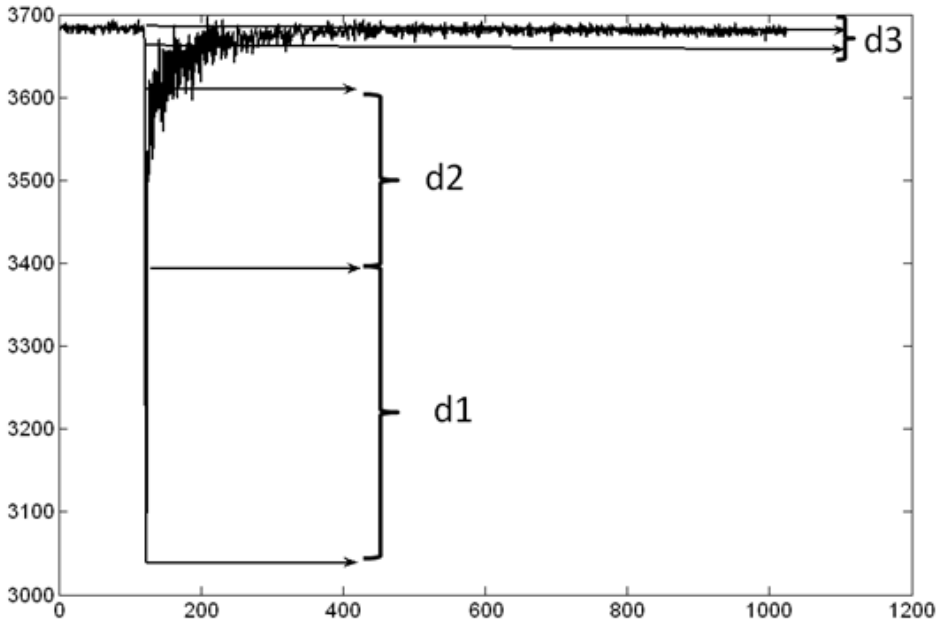

Fig. 3.17. Timing features of the input signal.

3.2.1.3 Fuzzy Interface System

Fuzziness in contrast with crispiness in data sets was introduced by L. Zadeh (1965). The main goal of fuzziness is to reduce system complexity and to provide a model that allows approximate results. Fuzzy logic has many applications in control systems, data clustering (Radecki 1982), image processing (Franke et al. 2000 and Wachs et al. 2003), robot control (Ghidary et al. 2001 and Shim et al. 1998), temperature and pressure control (Magdelena et al. 1996 and Zhang et al. 1999) and finance (Diao et al. 2000). In general it can be applied to all problems which contain some sort of uncertainty (Nedjah 2005).

Conventional mathematical system modeling (e. g. using differential equations) is not efficient when the system has some uncertainty and is non-deterministic, and most real world systems contain uncertainty. Fuzzy interface can model qualitative aspects of human knowledge without using exact quantitative analyses (Zhang 1993). The block diagram of a typical fuzzy interface system is shown in Fig. 3.18. First the crisp input is mapped into a linguistic input membership space (fuzzification). Then, according to the weight and strength, the output of each rule is generated and all the outputs are aggregated to make a fuzzy output. Finally, the fuzzy output is mapped into the crispy space using a defuzzification process (Zhang 1993).

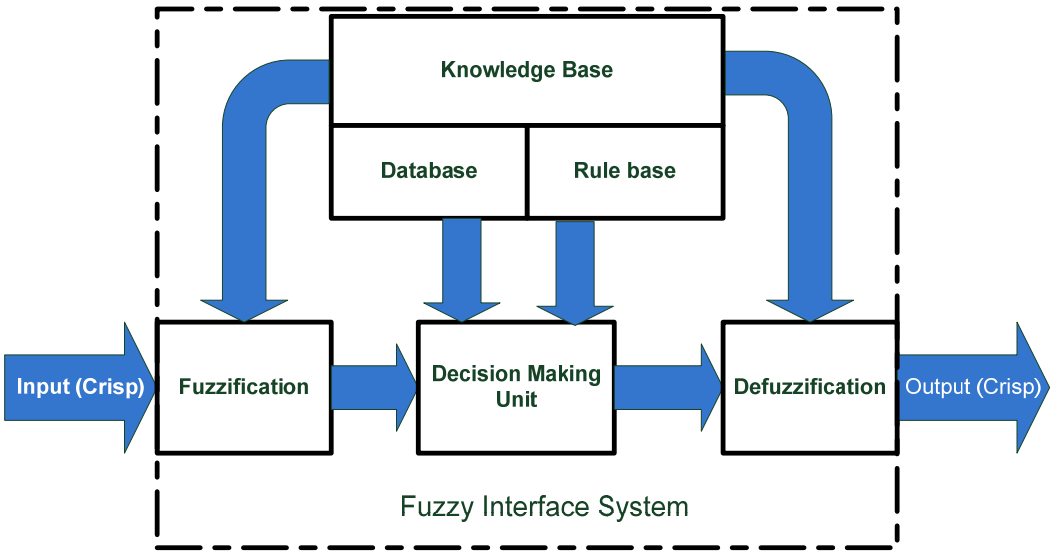

Fig. 3.18. Block diagram of a typical fuzzy system employed.

The fuzzy system employed in this paper has three inputs and three outputs. Fig. 3.19 shows the block diagram of the fuzzy system. The inputs to the system are features extracted in the previous part. The outputs are constant values K1, K2, and K3 in equation [3.1] and indicate if the signal contains the corresponding kind of exponential decay or not.

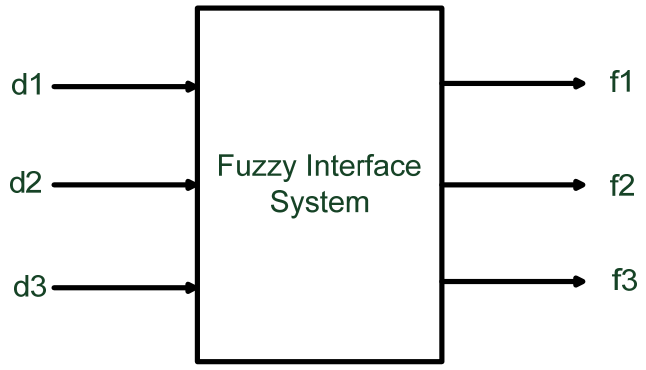

Fig. 3.19. Block Diagram of the fuzzy system employed.

For each input, a membership function with two linguistic values was selected. The input membership functions are shown in Fig. 3.20. Input d1 has two linguistic values, small and large. Input d2 is marked with two values, medium and large, and input d3 is marked with values small and large.

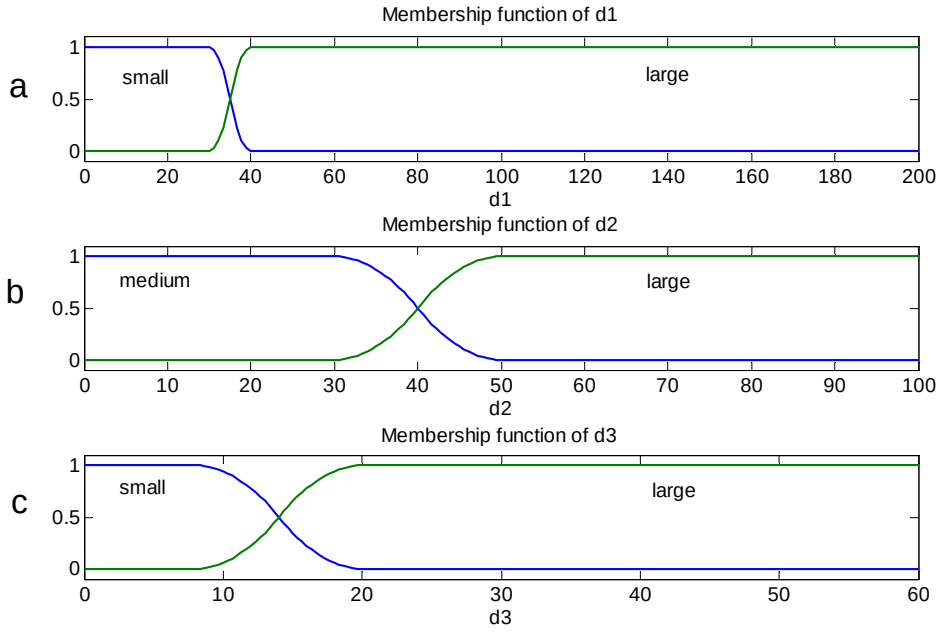

Fig. 3.20. Input membership functions. (a) Membership function of d1, (b) membership function of d2, (c) membership function of d3.

The output membership functions for the output variables (K1, K2 and K3), are shown in Fig. 3.21. Each output has two membership functions, negative and positive, which are Gaussian shaped functions centered at 1 and -1.

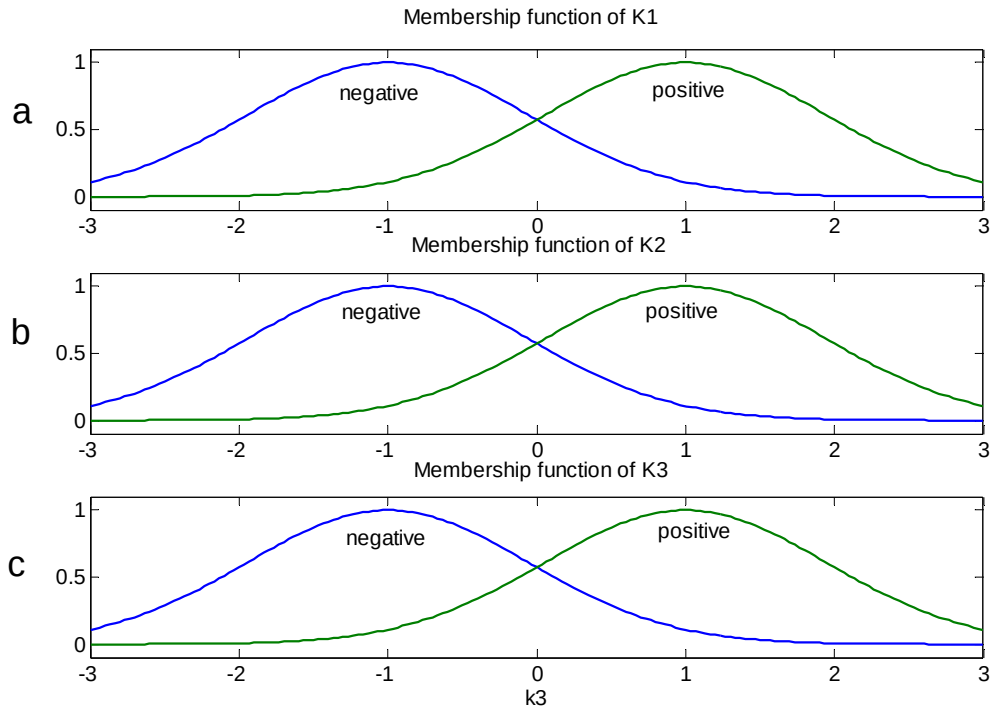

Fig. 3.21. Output membership functions. (a) Membership function of K1, (b) membership function of K2, (c) membership function of K3.

In order to discriminate between the seven possible cases suggested in (Farsoni et al 2007), seven rules were used. The if-then rule data base is shown below.

R1: If d1 is large and d2 is medium and d3 is small then K1 is positive and K2 is negative and K3 is negative.

R2: If d1 is small and d2 is large and d3 is small then K1 is negative and K2 is positive and K3 is negative.

R3: If d1 is large and d2 is large and d3 is small then K1 is positive and K2 is positive and K3 is negative.

R4: If d1 is small and d2 is medium and d3 is large then K1 is negative and K2 is negative and K3 is positive.

R5: If d1 is large and d2 is medium and d3 is large then K1 is positive and K2 is negative and K3 is positive.

R6: If d1 is small and d2 is large and d3 is large then K1 is negative and K2 is positive and K3 is positive.

R7: If d1 is large and d2 is large and d3 is large then K1 is positive and K2 is positive and K3 is positive.

If the output (K1, K2, and K3) is negative, it indicates that the interaction did not occur in that layer. If it is positive, it indicates that the interaction in that layer has occurred. Negative outputs are set to zero and positive values are set to one to validate equation [3.1].

3.2.1.4 Experimental Results for the Fuzzy Method

Pulses from the phoswich detector are captured using a digital pulse processor and analyzed using Matlab®. Several cases were studied using pure beta,

pure gamma, and mixed beta/gamma sources. ^{99}Tc and ^{90}Sr/Y were used for beta, ^{137}Cs for gamma and the combination of the sources for the mixed case. Single beta/gamma sources were not used for both beta and gamma components because of a moderate amount of self-shielding already present in the check sources and the inability to capture mono-energetic conversion electrons.

Gamma Sources

The features and the spectra of the pulses captured from a ^{137}Cs source are plotted in Fig. 3.22 and Fig. 3.33, respectively. This spectrum was obtained by capturing 4945 pulses from a ^{137}Cs source and processing them in a host computer. The beta energy spectrum of ^{137}Cs indicates that, at low energies, some gamma rays, mostly Compton events, interact with the 1st and 2nd layer and cause the misclassification of pulses as beta. This phenomenon is not observed at high energies because high energy gamma rays usually do not interact with the 1st and 2nd layer.

The algorithm performance can be measured by full width at half maximum (FWHM) of the spectrum at the energy peak. The measured 662KeV photo-peak resolution in this experiment was approximately 6.7%. It can be noticed that photo-peak is almost symmetrical. Other spectral features such as the Backscatter peak, the Compton continuum, and the Compton edge can also be observed.

Some low-energy gamma rays (mostly Compton events) interact with the 1st and/or 2nd layer and cause the pulse to be misclassified as beta. However, this phenomenon is not observed at higher energies and these pulses pass so the spectra of gamma-ray absorption in the 1st and 2nd layer should be observed only at low energies.

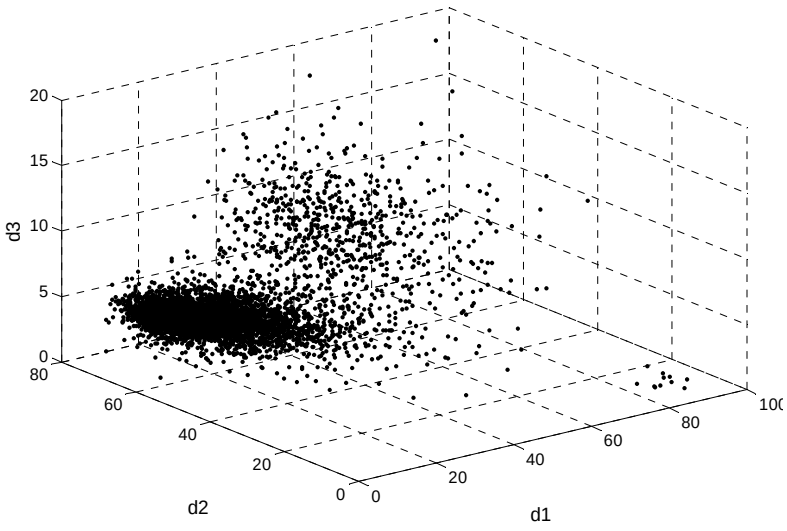

Fig. 3.22. The fuzzy features of a ^{137}Cs source.

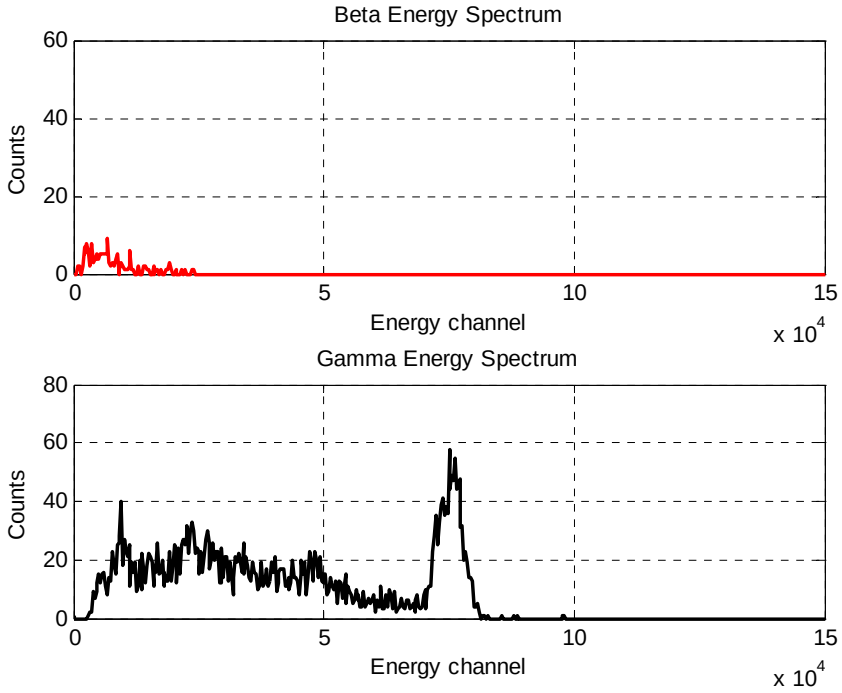

Fig. 3.23. The energy spectrum of the ^{137}Cs with the features plotted in Fig. 3.22.

The features and spectrum of the pulses recorded from a ^{60}Co source are plotted in Fig. 3.24 and Fig. 3.25, respectively.

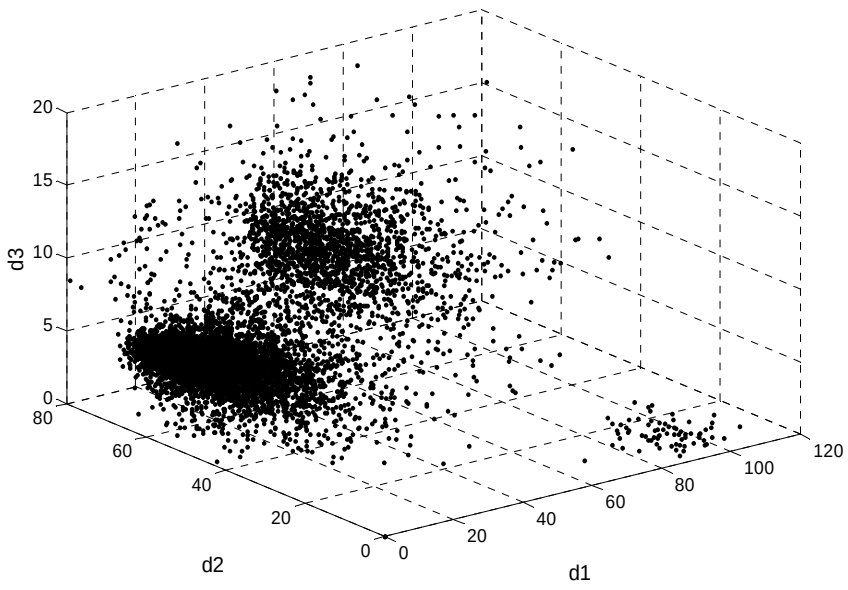

Fig. 3.24. The fuzzy features of a ^{60}Co source.

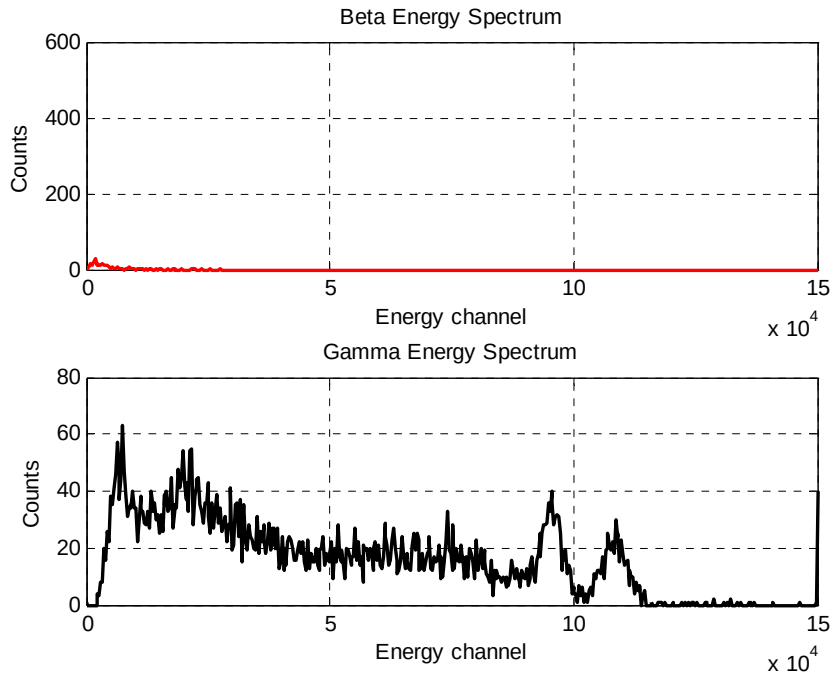

Fig. 3.25. The energy spectrum of the ^{60}Co source with the features plotted in Fig. 3.24.

Beta Sources

To evaluate the algorithm for the beta response, two sources were used. The features and the spectra of the pulses from a ^{99}Tc source are plotted in Fig. 3.26 and Fig. 3.27, respectively. In this experiment, 4989 pulses from the ^{99}Tc source were captured. At lower energies the detector works correctly in discriminating beta and gamma signals. But some high energy pulses could escape from the 1st and 2nd layer, and interact with the 3rd layer, which causes misclassification of these pulses as gamma. Some of the pulses are misclassified as Compton-induced pulses which may originate from interactions of gamma-rays in the second layer. This phenomenon is more obvious when capturing signals from a higher energy beta source (e. g. ^{90}Sr/Y). High-energy beta particles have a better chance to escape from the 1st and 2nd layer and interact with the 3rd layer and cause misclassification as gamma.

The features and the spectra of the pulses recorded from a ^{90}Sr/Y source are plotted in Fig. 3.28 and Fig. 3.29, respectively. In this experiment, 10,000 pulses from this source were captured.

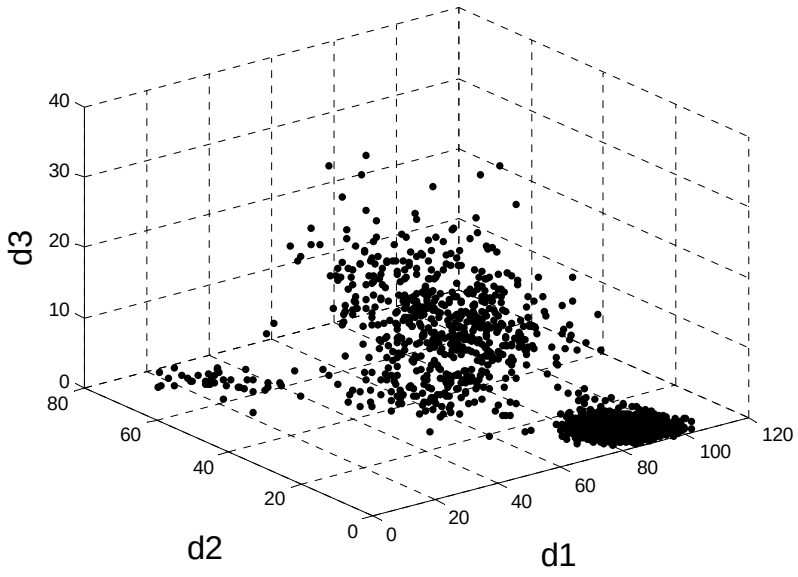

Fig. 3.26. The fuzzy features of a ^{99}Tc source.

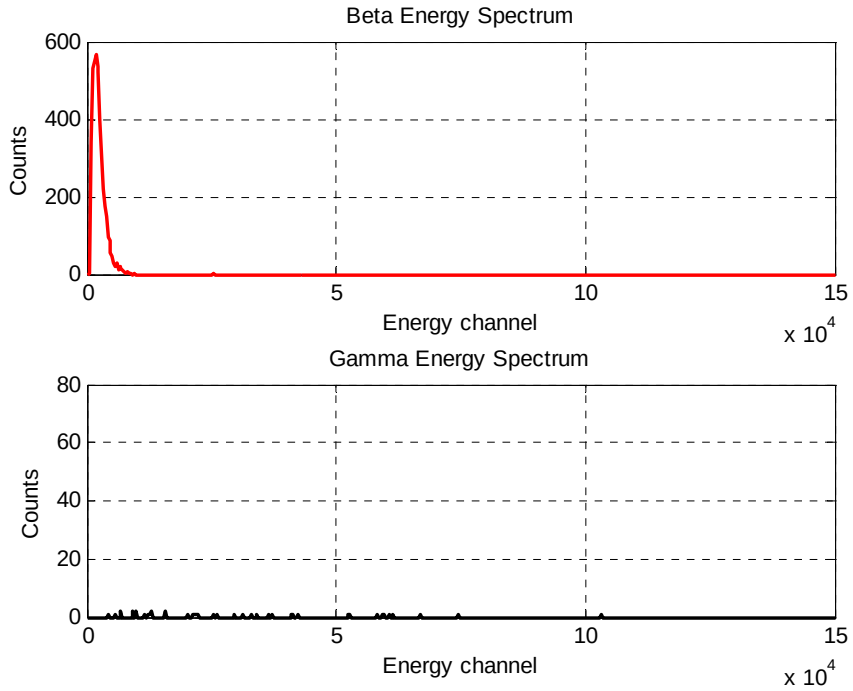

Fig. 3.27. The energy spectrum of the ^{99}Tc source with the features plotted in Fig. 3.26.

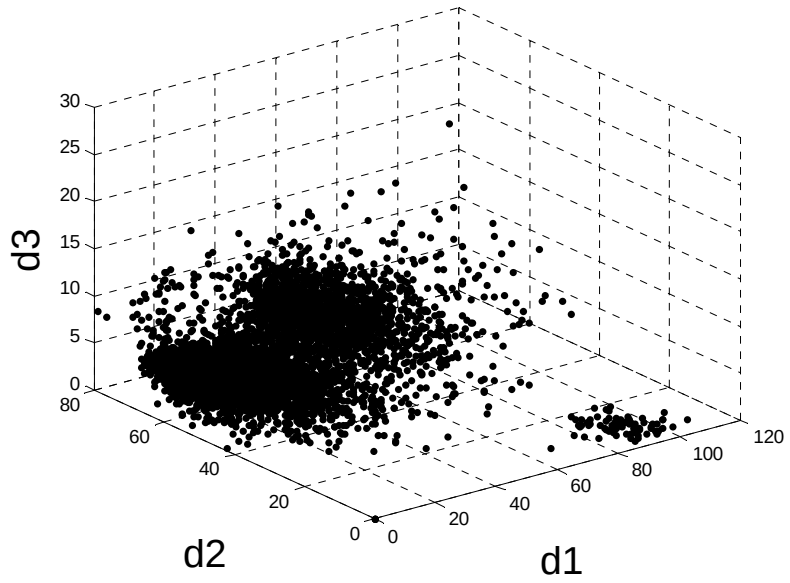

Fig. 3.28. The fuzzy features of a ^{90}Sr/Y source.

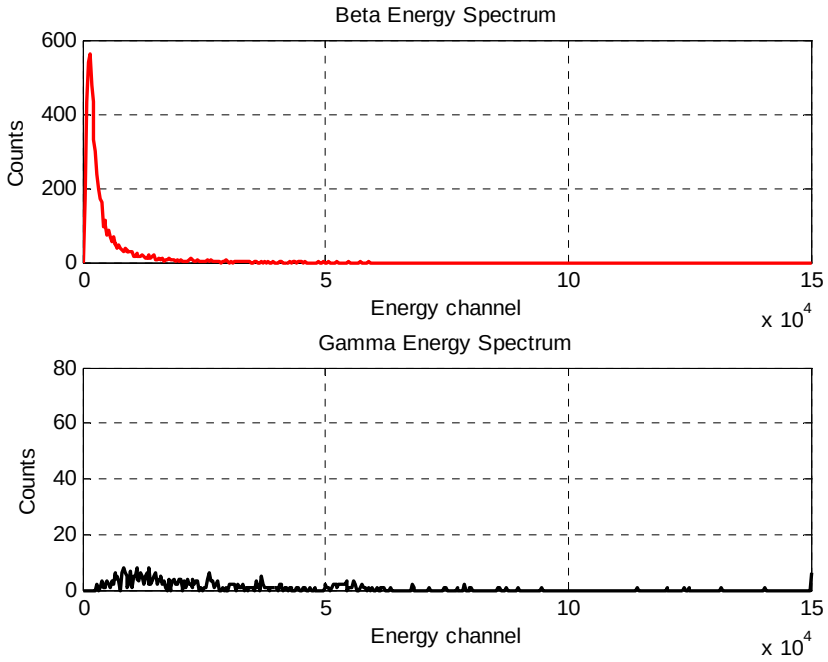

Fig. 3.29. The energy spectrum of the ^{90}Sr/Y source with the features plotted in Fig. 3.28.

Mixed beta and gamma Sources

Simultaneous detection of beta and gamma was tested by using different sources of beta and gamma together. The spectrums of the mixed fields are shown below. The features and the spectra of the pulses captured from a mixed field of ^{137}Cs and ^{90}Sr/Y sources are plotted in Fig. 3.30 and Fig. 3.31, respectively. Also, the features and the spectra of the mixed field of ^{60}Co and ^{99}Tc are plotted in Fig. 3.32 and Fig. 3.33, respectively.

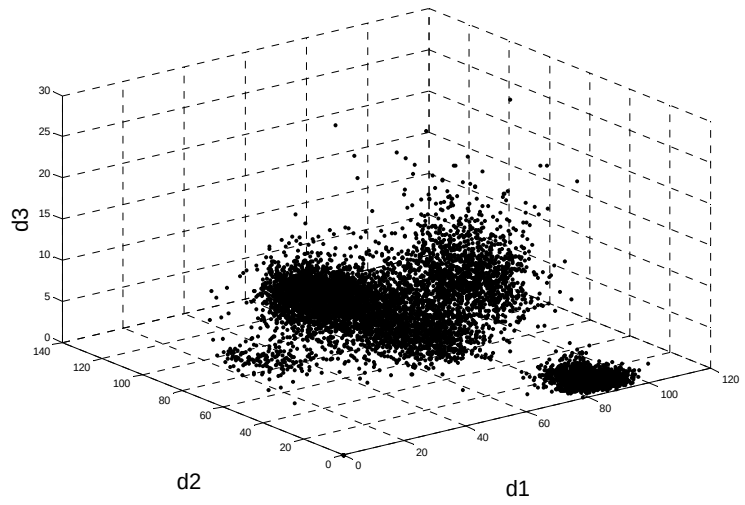

Fig. 3.30. The fuzzy features of a mixed radiation field of ^{137}Cs and ^{90}Sr/Y sources.

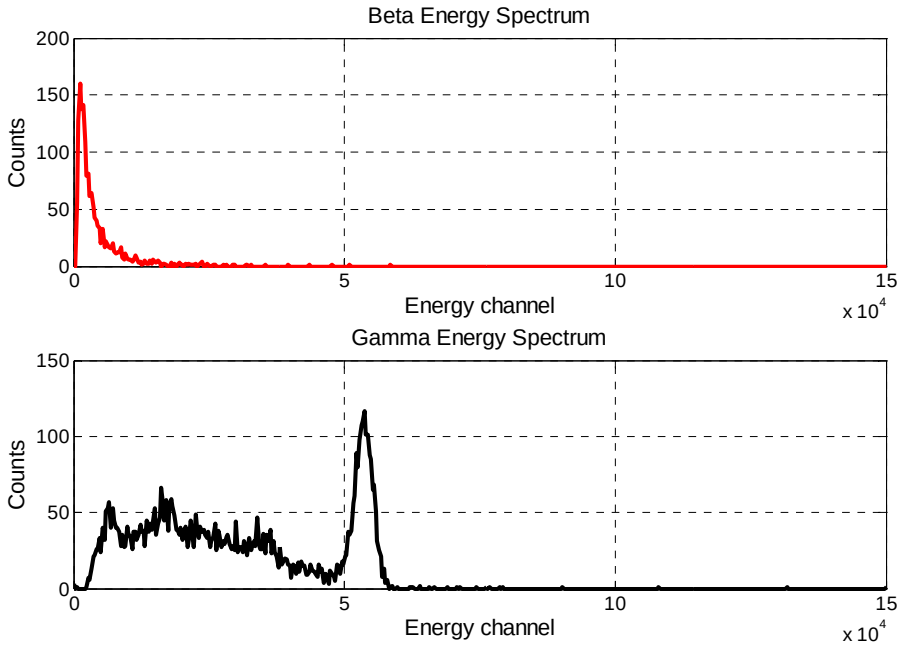

Fig. 3.31. The energy spectrum of the mixed ^{137}Cs and ^{90}Sr/Y sources with the features plotted in Fig. 3.30.

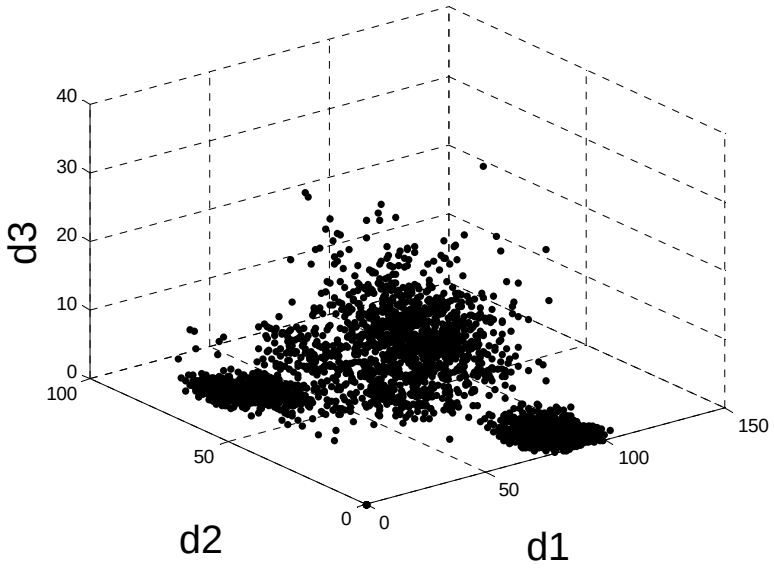

Fig. 3.32. The fuzzy features of a mixed radiation field of ^{60}Co and ^{99}Tc source.

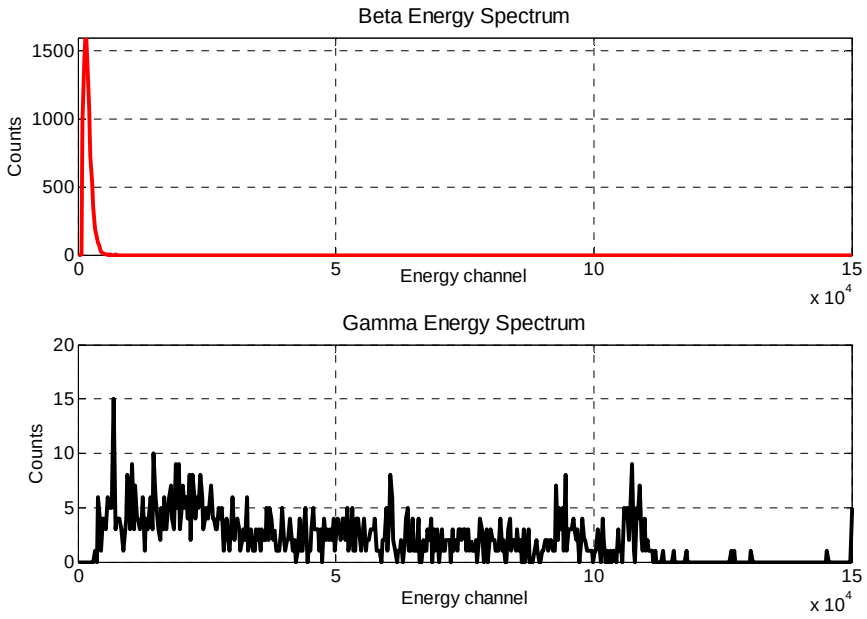

Fig. 3.33. The energy spectrum of the mixed field of ^{60}Co and ^{99}Tc sources with the features plotted in Fig. 3.32.

3.2.2 Wavelet Method

3.2.2.1 The Wavelet Transform

The wavelet transform decomposes signals over dilated and translated wavelets. The wavelet transform of a function $f \in L^2(\mathbb{R})$, the space of square integrable functions over $\mathbb{R}$ at scale *a* and shift *b* is defined as

$$W_f(a,b) = < f, \psi_{a,b} > = \int_{-\infty}^{\infty} f(t) \frac{1}{\sqrt{a}} \psi^*(\frac{t-b}{a}) dt, \qquad [3.8]$$

where $\psi \in L^2(\mathbb{R})$ is the wavelet function with zero average and unit L_2 norm $||\psi|| = 1$. In this application, 'Haar' wavelets were used. It should be noted that each pulse is

normalized to a unit peak to peak signal before computing the wavelet transform. The normalization process removes the dependency of the wavelet transform on the amplitude of the signal.

It should be noted that *f(t)* is a discrete signal and we use a piecewise constant interpolation of the *f(k)* where *k=1 to length(f).* The algorithm can be written as

$$C_{a,b} = < f, \psi_{a,b} > = \int_{-\infty}^{\infty} f(t) \frac{1}{\sqrt{a}} \psi^*(\frac{t-b}{a}) dt = \sum_k \int_k^{k+1} f(t) \frac{1}{\sqrt{a}} \psi^*(\frac{t-b}{a}) \quad [3.9]$$

If *f(t)=f[k]* for $t \in [k, k+1]$ then

$$C_{a,b} = \frac{1}{\sqrt{a}} \sum_k s(k) \int_k^{k+1} f[k] \psi^*(\frac{t-b}{a}) \quad [3.10]$$

A new function P(a) (called the 'Scale function') is defined as the energy of the wavelet transform of the signal at a specific scale and with different shifts. Its expression is

$$P(a) = \frac{1}{1+n_b} \sum_{j=0}^{n_b} | W_\psi^s(a, b_j)|^2, \quad [3.11]$$

where $W_\psi^s(a, b_j)$ is the wavelet transform of the normalized signal.

The experimental results show that the scale function allows for a good separation between different signals having different decaying components. It was observed that the pulses recorded from a mixed ^{137}Cs and ^{90}Sr radiation field have seven different pulse shapes which are the result of the absorption of beta particles

and gamma rays in different layers. Each pulse shape represents one scenario from seven possible cases (Farsoni et al. 2007). The seven possible normalized pulses and their corresponding scale functions are plotted in Fig. 3.34 and Fig. 3.35, respectively. It can be observed that the scale functions of the pulses with different decaying components show different behaviors, and the scale function can be used as a discrimination function between these pulses. It should be noted that the scenario associated with the absorption in the 1^{st} and 3^{rd} layer and also the scenario associated with the absorption in all three layers were, very rare and were observed only a few times.

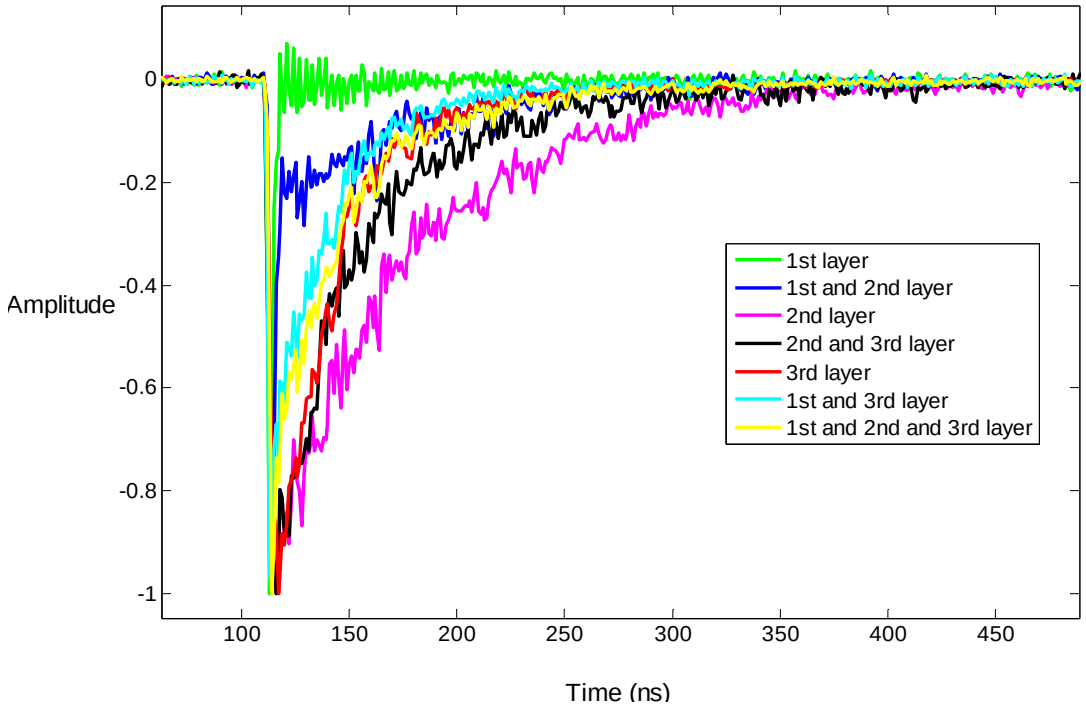

Fig. 3.34. The normalized waveforms of the seven possible scenarios.

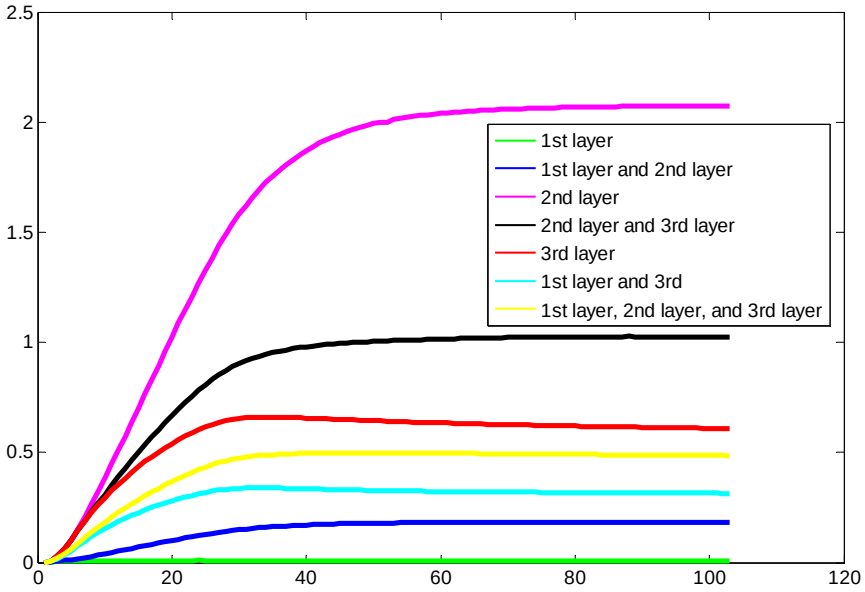

Fig. 3.35. The corresponding scale functions of the seven possible waveforms of Fig. 3.34.

3.2.2.2 Feature Extraction

The scale functions of 250 pulses from a mixed field of ^{137}Cs and ^{90}Sr are plotted in Fig.3.36. It can be observed that the values of the scale function at scales 128 and 1024 can be used to discriminate between these pulses.

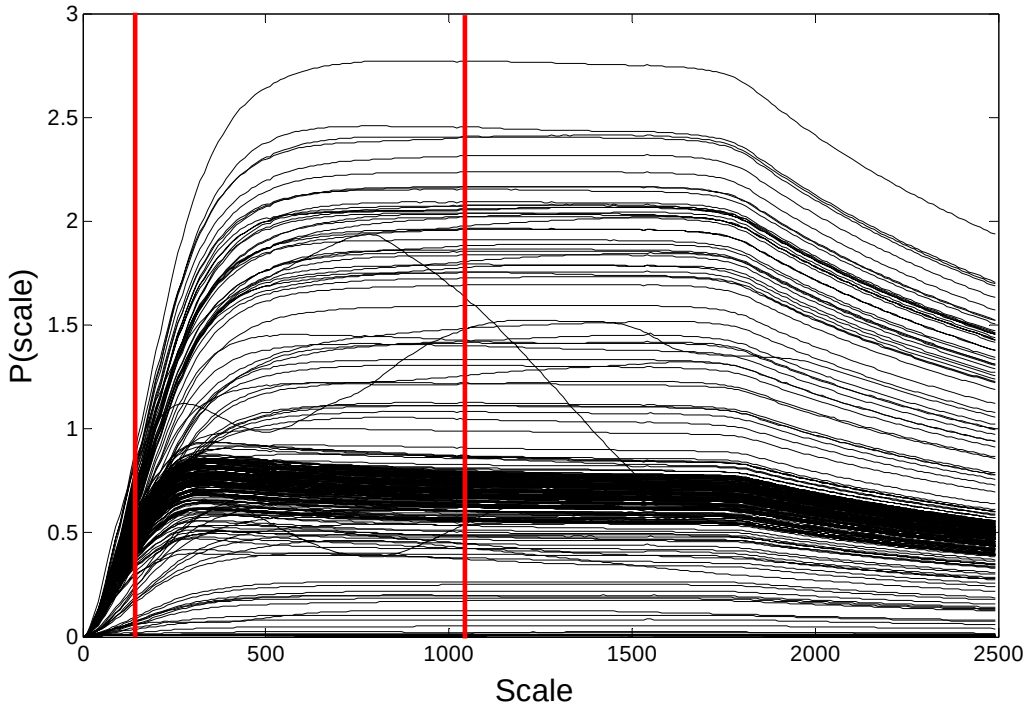

Fig. 3.36. The scale functions of 250 pulses recorded from a mixed source of ^{137}Cs and ^{90}Sr/Y (black pulses). The scale function at scales 128 and 2024 are chosen as the PSD features.

For simplicity, in the algorithm, the discrimination features are selected as follows. First, a feature is selected as the value of the scale function at scale 128. The second feature is selected as the ratio of the value of the scale function at scale 1024 to the value of scale function at scale 128. Scales 128 and 1024 are chosen as powers of 2 in order use the discrete wavelet transform (DWT). The DWT can be easily implemented in digital processors and FPGAs (Ballagh 2001). Features f_1 and f_2 are selected using the following equations

$$f_1 = P\,(a)|_{a=128}\,, \qquad [3.12]$$

and

$$f_2 = \frac{P\,(a)|_{a=1024}}{P\,(a)|_{a=128}} \quad . \qquad [3.13]$$

The features of 250 pulses taken separately from ^{137}Cs and ^{99}Tc sources are plotted in Fig. 3.37 where the X axis is f_1 and the Y axis is f_2. The blue dots represent the features of the pulses taken from a ^{137}Cs source and the red dots represent the features of the pulses taken from a ^{99}Tc source. It can be observed that the selected features allow for a good separation between beta particles and gamma rays and can be used to discriminate among pulses which are recorded from a mixed radiation field.

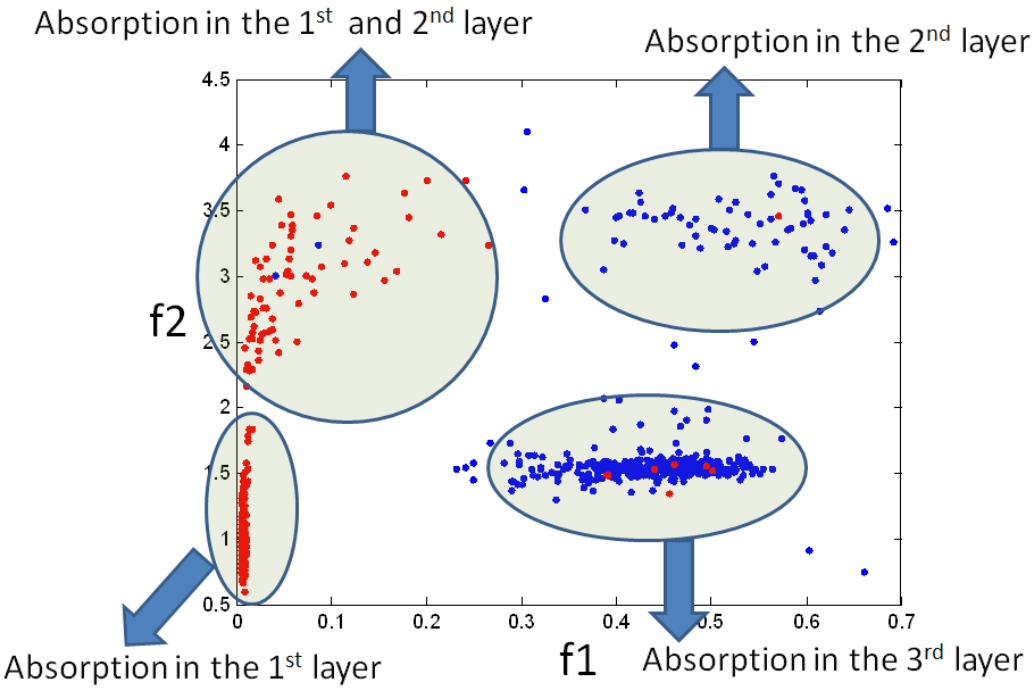

Fig. 3.37. The features of 250 captured pulses from ^{137}Cs and ^{99}Tc, separately. The blue dots represent the ^{137}Cs features and the red dots represent the ^{99}Tc features.

In order to test the algorithm for different radiation sources, different beta and gamma sources were used separately and simultaneously. In this experiment, ^{137}Cs and ^{60}Co gamma sources and ^{90}Sr/Y and ^{99}Tc beta sources were used. After performing the pulse shape discrimination, the energy of the signal is measured and the beta spectrum and gamma spectrum are derived. The results are presented next.

The features and the spectra of the pulses captured from a ^{137}Cs source are plotted in Fig. 3.38 and Fig. 3.39, respectively. Also, the features and the spectra of the pulses recorded from a ^{60}Co source are plotted in Fig. 3.40 and Fig. 3.41, respectively.

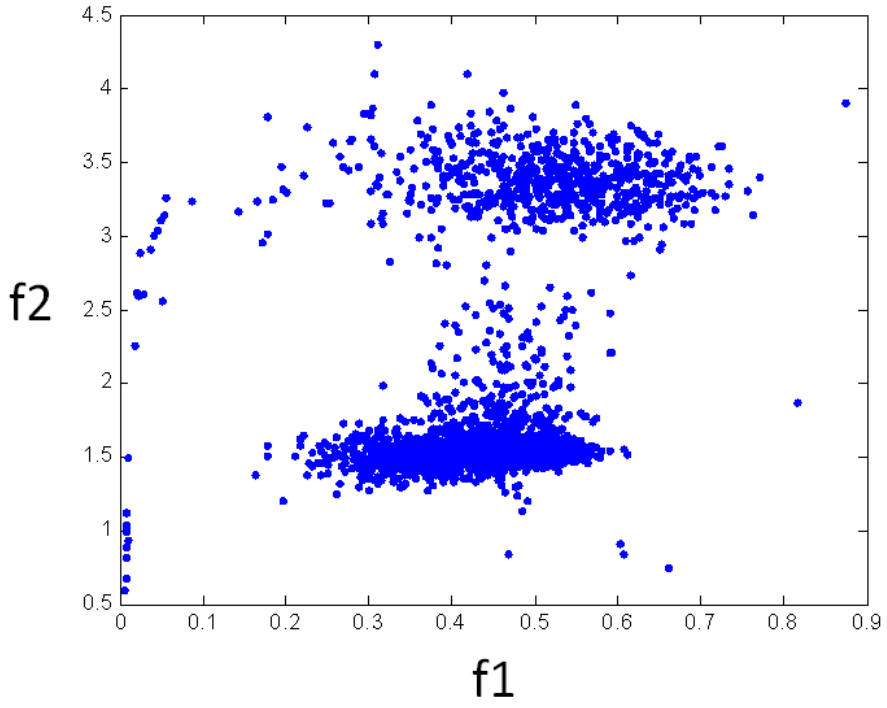

Fig. 3.38. The wavelet features of a ^{137}Cs source.

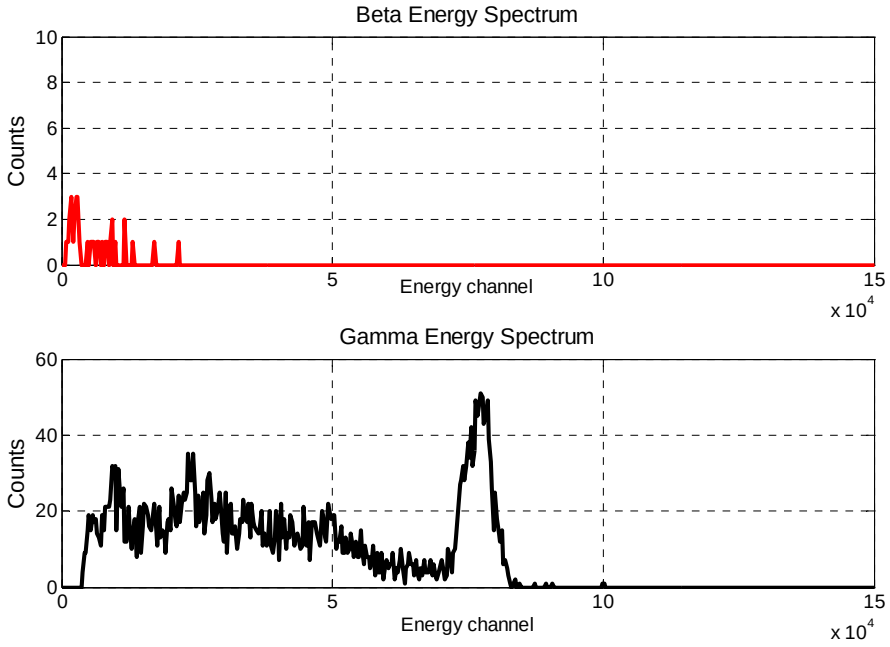

Fig. 3.39. The energy spectrum of the ^{137}Cs source with the features plotted in Fig. 3.38.

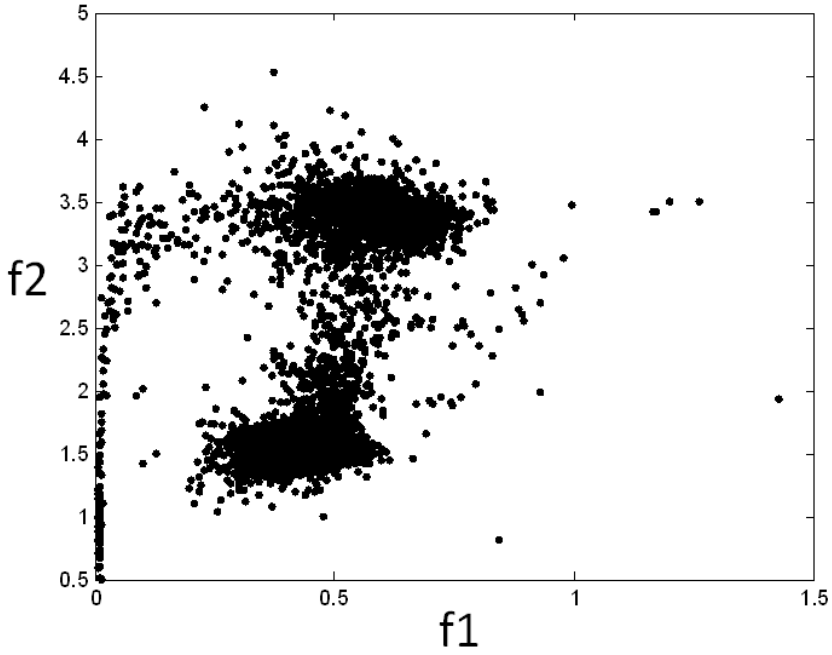

Fig. 3.40. The wavelet features of a ^{60}Co source.

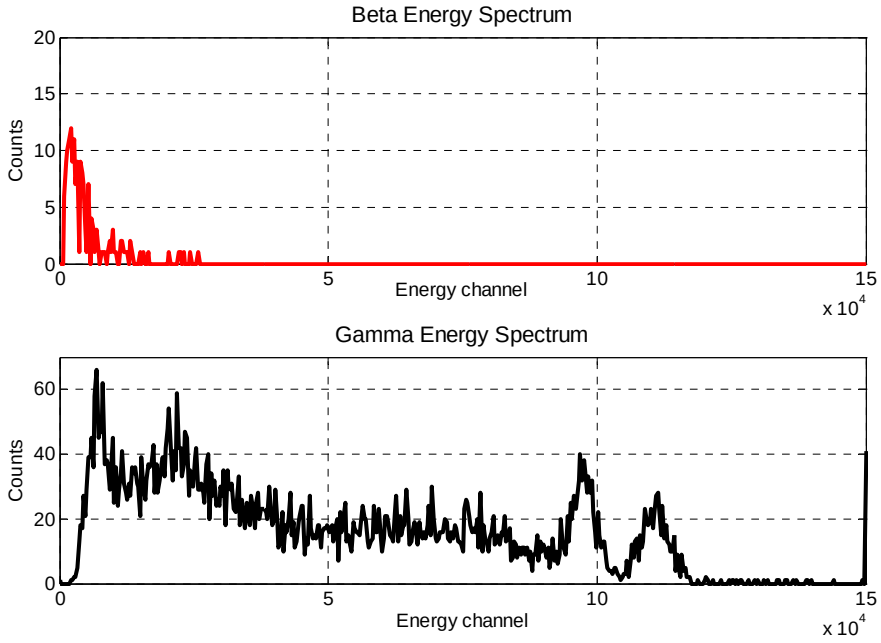

Fig. 3.41. The energy spectrum of the ^{60}Co source with the features plotted in Fig. 3.40.

In order to test the algorithm for beta sources, ^{90}Sr/Y and ^{99}Tc were used. The features and the spectra of the pulses captured from a ^{99}Tc source are plotted in Fig. 3.42 and Fig. 3.43, respectively. The features and the spectra of the pulses recorded from a ^{90}Sr/Y source are plotted in Fig. 3.44 and Fig. 3.45, respectively.

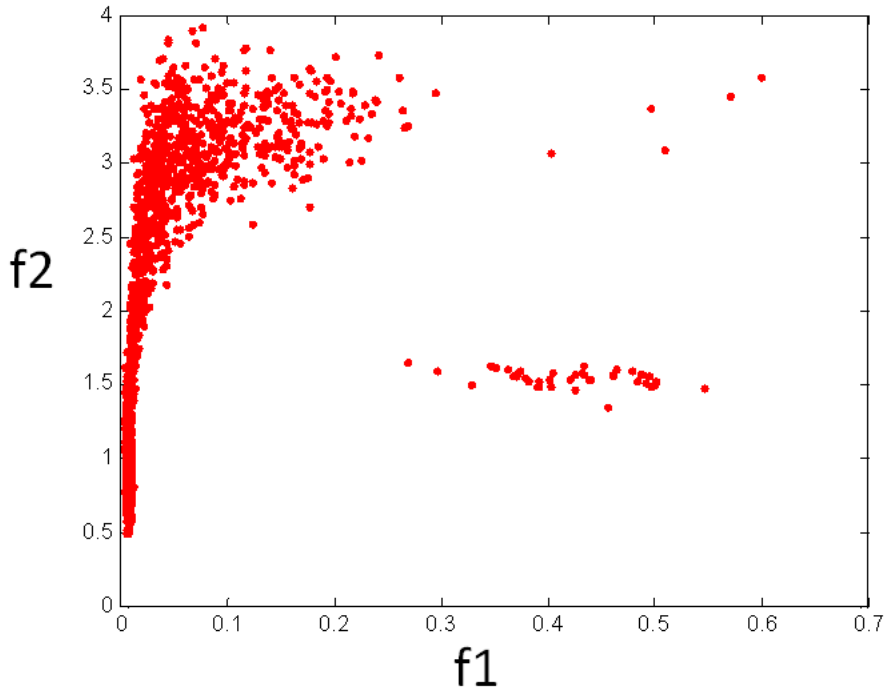

Fig. 3.42. The wavelet features of a ^{99}Tc source.

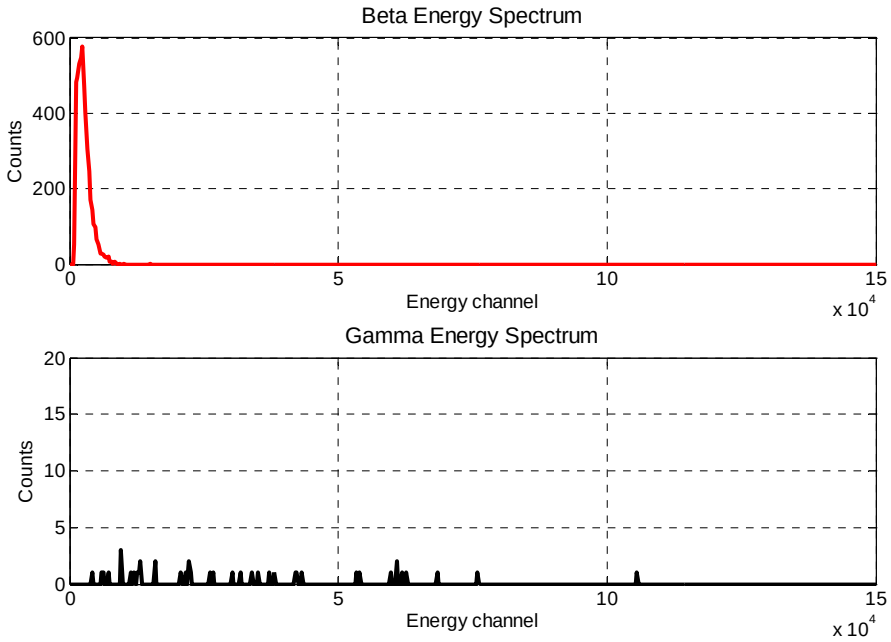

Fig. 3.43. The energy spectrum of the ^{99}Tc source with the features plotted in Fig. 3.42.

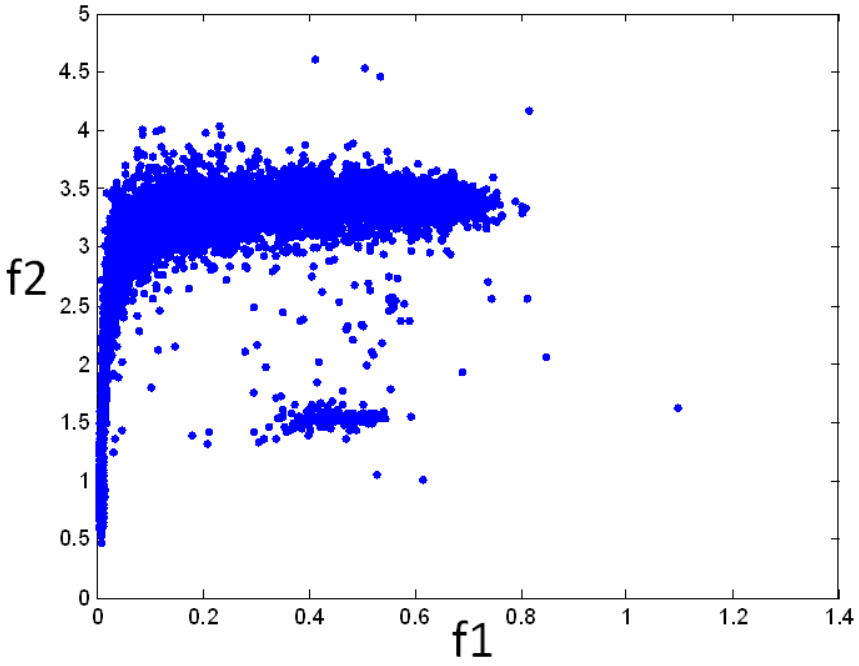

Fig. 3.44. The wavelet features of a ^{90}Sr/Y source.

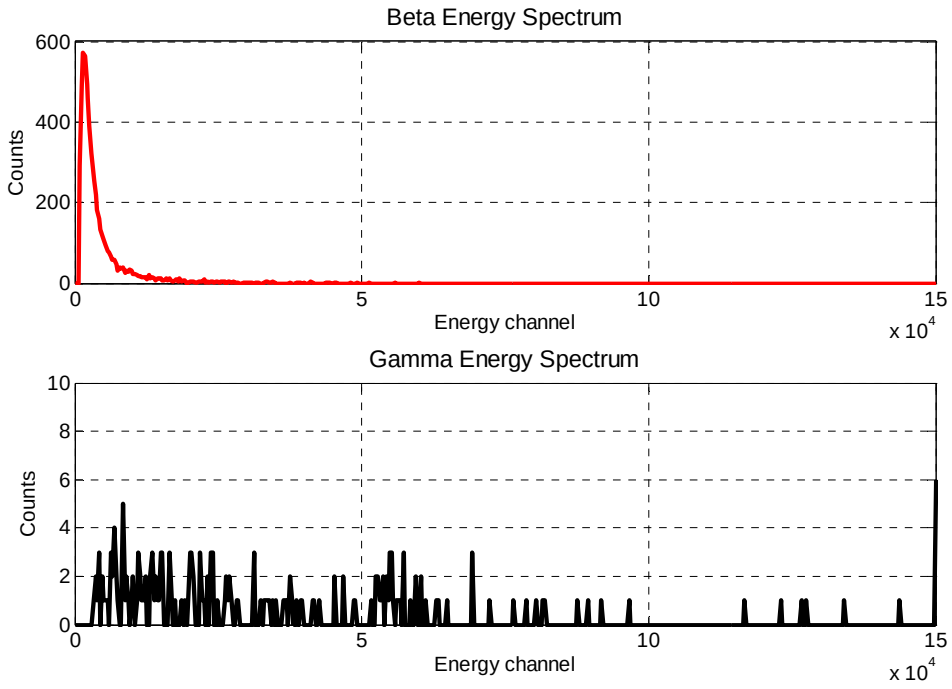

Fig. 3.45. The energy spectrum of the ^{90}Sr/Y source with the features plotted in Fig. 3.44.

The features and the spectra of the pulses captured from a mixed field of ^{137}Cs and ^{90}Sr/Y are plotted in Fig. 3.46 and Fig. 3.47, respectively. Also, the features and the spectra of the mixed field of ^{60}Co and ^{99}Tc are plotted in Fig. 3.48 and Fig. 3.49, respectively.

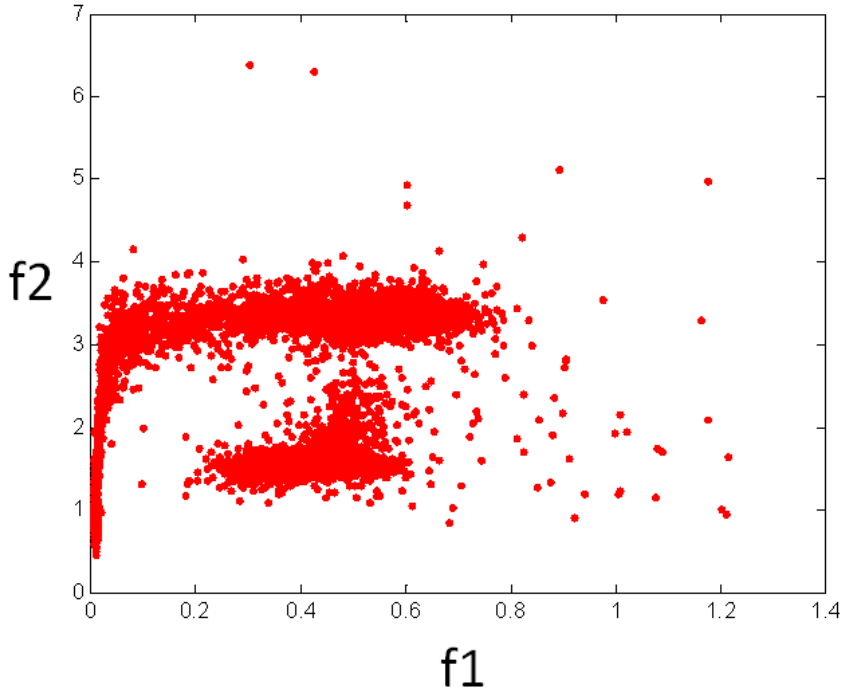

Fig. 3.46. The wavelet features of a mixed radiation field of ^{137}Cs and ^{90}Sr/Y sources.

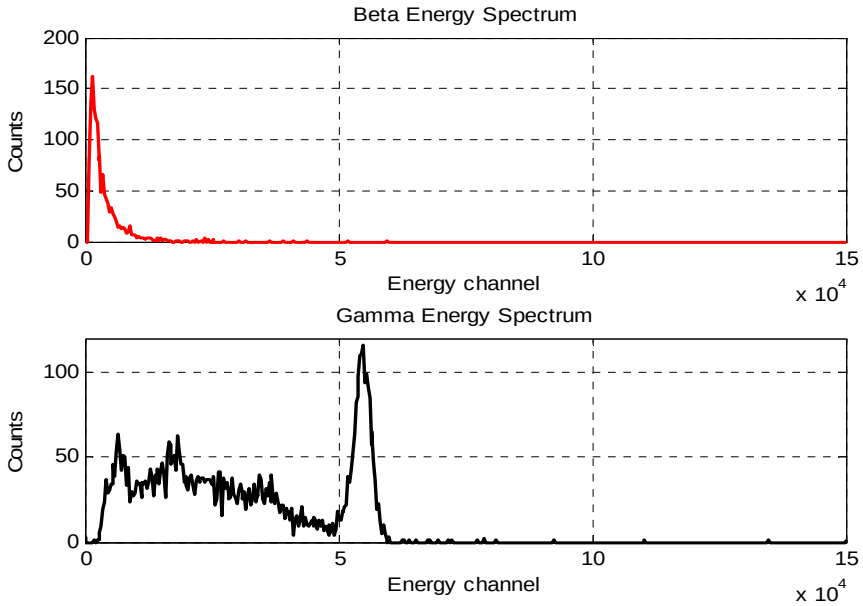

Fig. 3.47. The energy spectrum of the mixed ^{137}Cs and ^{90}Sr/Y source with the features plotted in Fig. 3.46.

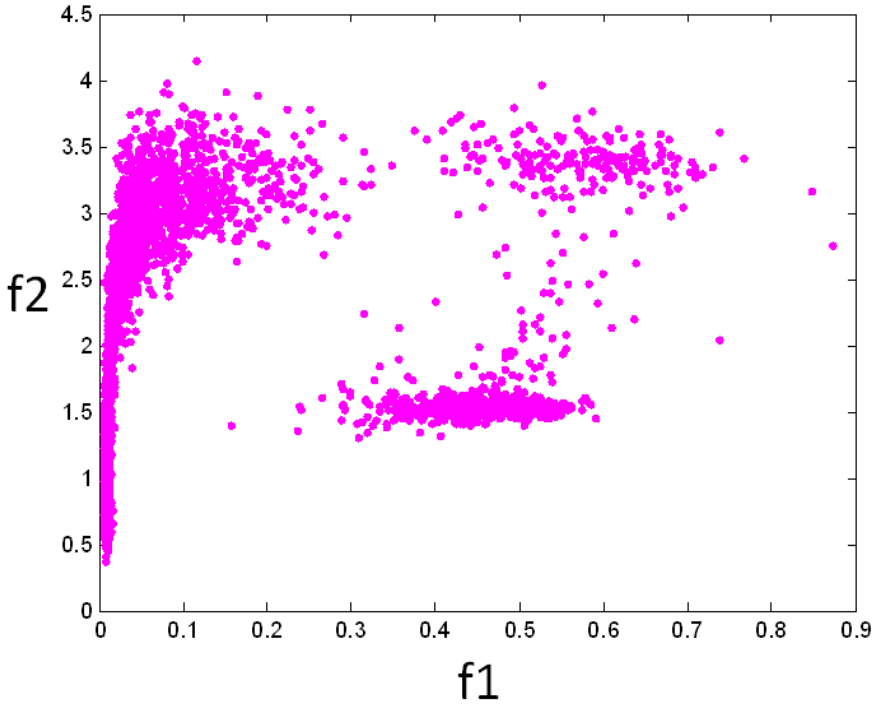

Fig. 3.48. The wavelet features of a mixed radiation field of ^{60}Co and ^{99}Tc sources.

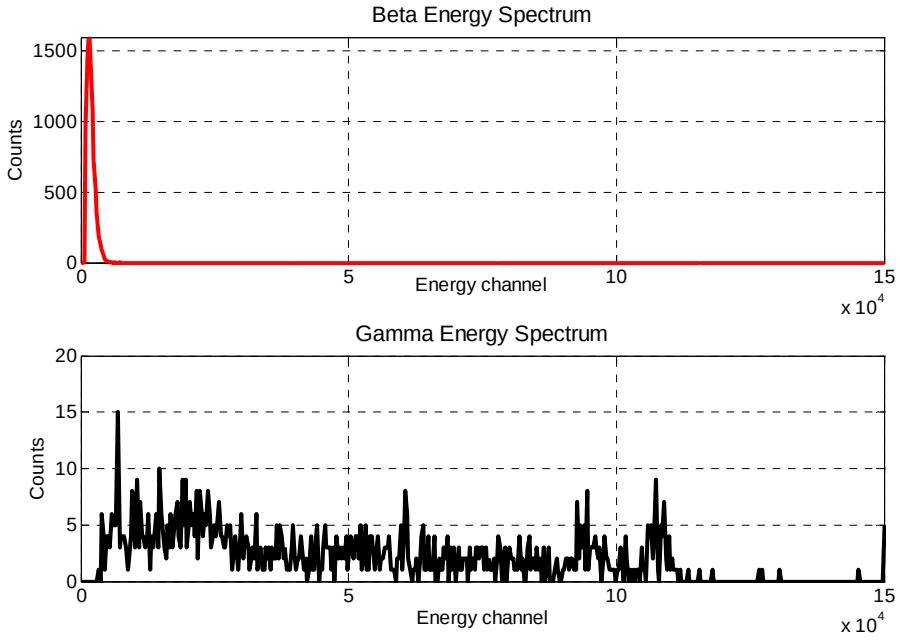

Fig. 3.49. The energy spectrum of the mixed field of ^{60}Co and ^{99}Tc sources with the features plotted in Fig. 3.48.

4 Discussion and Comparison

In this section, the discrimination performances of the two new methods advanced in this thesis are compared with two referenced methods. The two referenced methods are the Constant Time Discrimination (CTD) and the method of Farsoni et al. (2007). The four methods were applied to six different data sets: ^{137}Cs and ^{60}Co gamma sources, ^{99}TC and ^{90}Sr/Y beta sources, mixed ^{137}Cs and ^{90}Sr/Y, and mixed ^{60}Co and ^{99}Tc sources.

The Constant Time Discrimination method is based on taking one sample of the normalized signal after a constant time with respect to the peak. In this experiment, the constant time is 300ns. The value of the signal at the specified constant time is used to discriminate between different pulse shapes (Fig. 4.1).

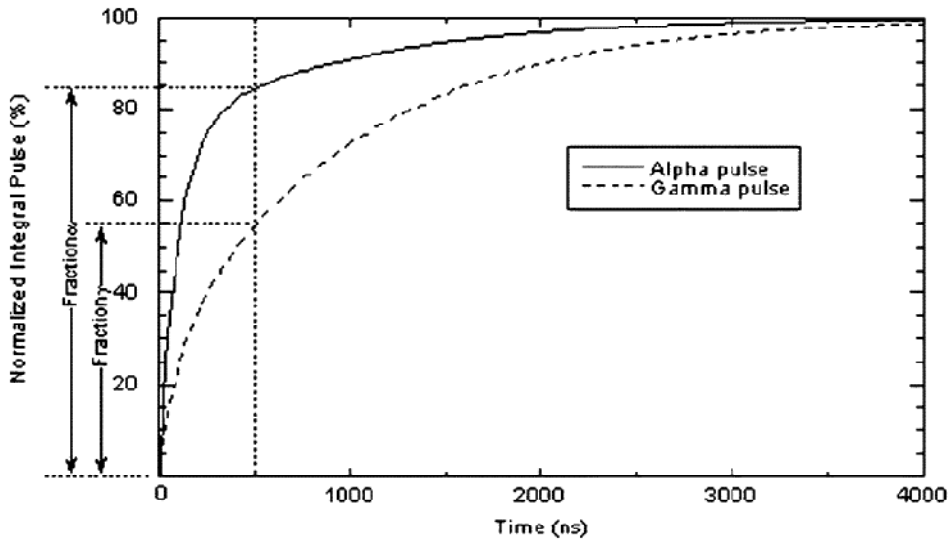

Fig. 4.1. Constant-time discrimination features. (© Chandrikamohan 2007)

The Farsoni's method (2007) is based on using two features of the signal, the fast ratio and the slow ratio, defined next. The feature extraction in this method works as follows. Four quantities (baseline, P, M1 and M2) that describe the basic shape of each pulse are measured (Fig. 4.2). The "Baseline" is defined as the average of 100 samples before the trigger point is calculated. The peak of the pulse, P, is the maximum value in the pulse. The value "M1" is the average over the five samples just after the fast decay component, which is between samples 5 and 9 relatively to the peak sample. "M2" is the average over the five samples between 30 and 34, relatively to the peak sample (Fig. 4.2). The fast-ratio (FR) and the slow-ratio (SR) of the captured signal are determined as *FR= (P-M1)/P* and *SR= (M1-M2)/M1* respectively (Farsoni et al. 2007).

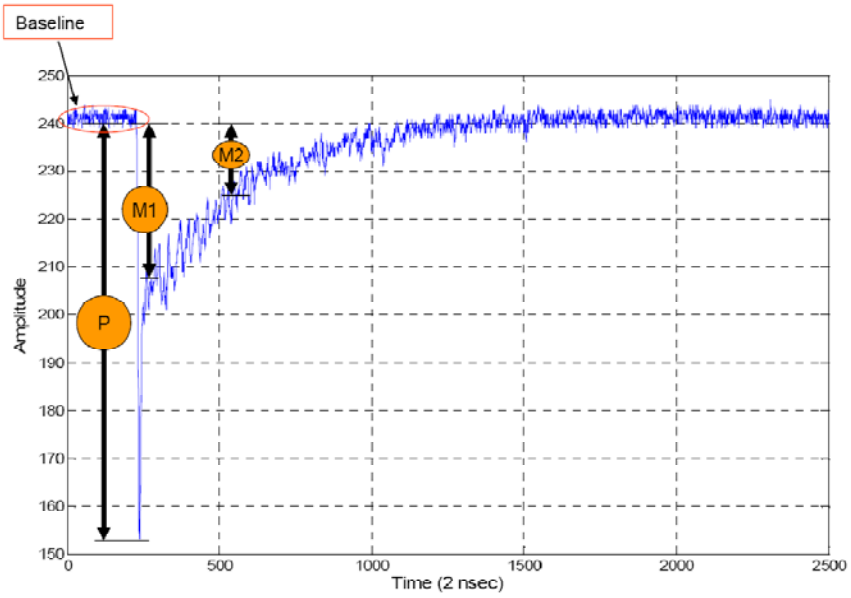

Fig. 4.2. The four parameters, baseline, P, M1 and M2 used for analyzing the anode pulses in Farsoni's method. (© Farsoni 2007)

Figs 4.3 to 4.8 show the features extracted for pulse shape discrimination using the four different methods: the constant time discrimination method, Farsoni's method, the time-domain fuzzy method, and the wavelet method. For each figure, plot "a" shows the features extracted using the CTD method, plot "b" shows the features extracted using the Farsoni's method, plot "c" shows the features extracted using the time-domain fuzzy method and plot "d" shows the features extracted using the wavelet method.

The performances of these methods are compared with each other in Tables 4.1-4.4 for ^{137}Cs, ^{60}Co, ^{90}Sr/Y and ^{99}Tc sources, respectively.

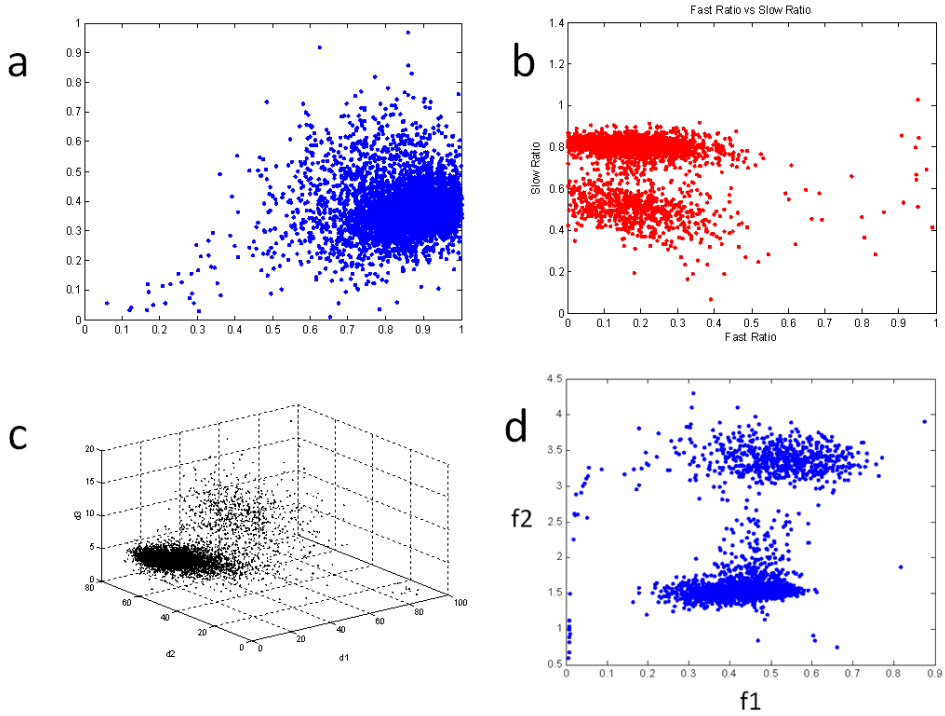

Fig. 4.3. The features of a ^{137}Cs source extracted using four different methods. (a) CTD, (b) Farsoni's method, (c) time-domain fuzzy method, (d) wavelet method.

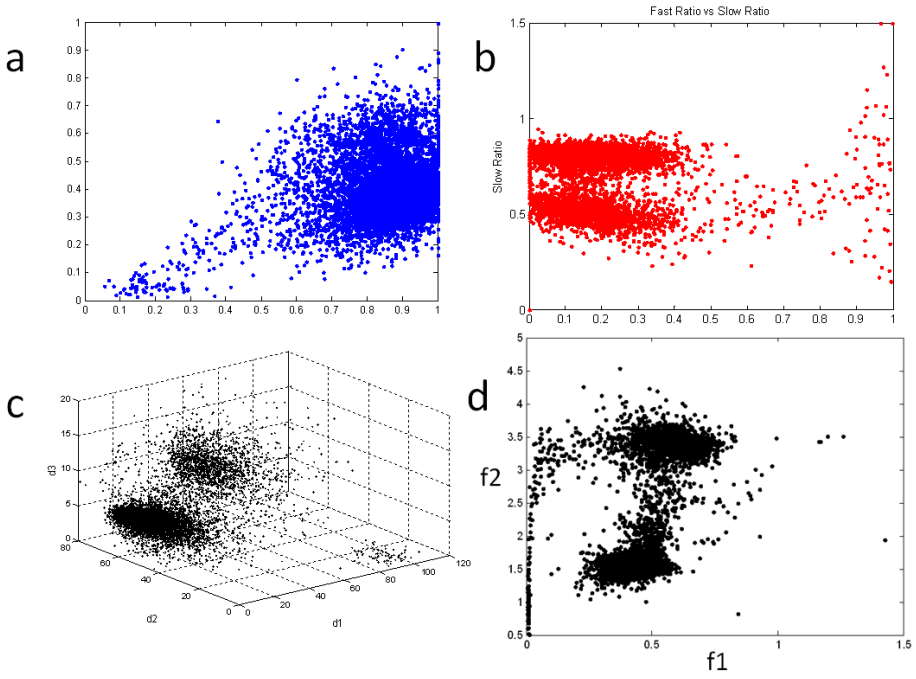

Fig. 4.4. The features of a ^{60}Co source extracted using four different methods. (a) CTD, (b) Farsoni's method, (c) time-domain fuzzy method, (d) wavelet method.

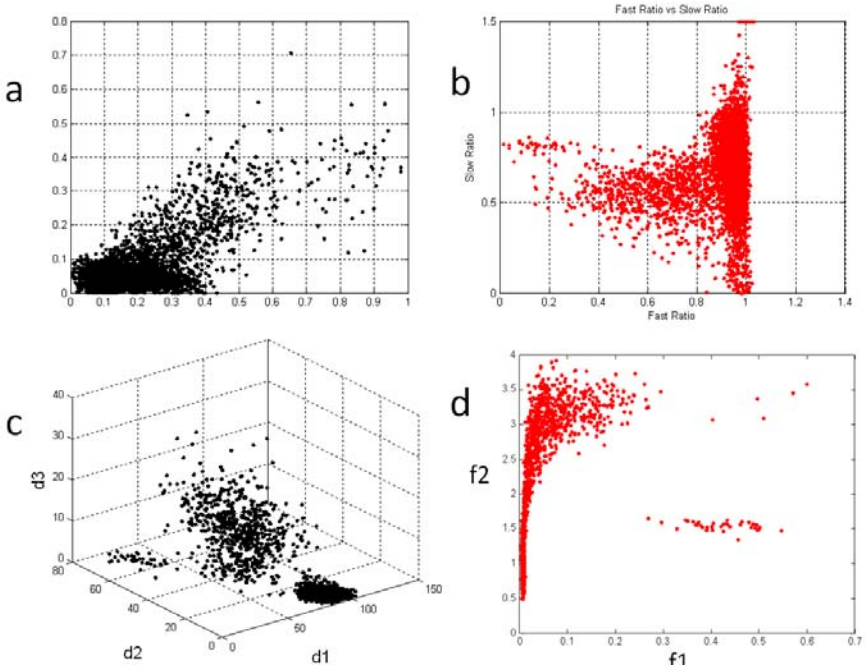

Fig. 4.5. The features of a ^{99}Tc source extracted using four different methods. (a) CTD, (b) Farsoni's method, (c) time-domain fuzzy method, (d) wavelet method.

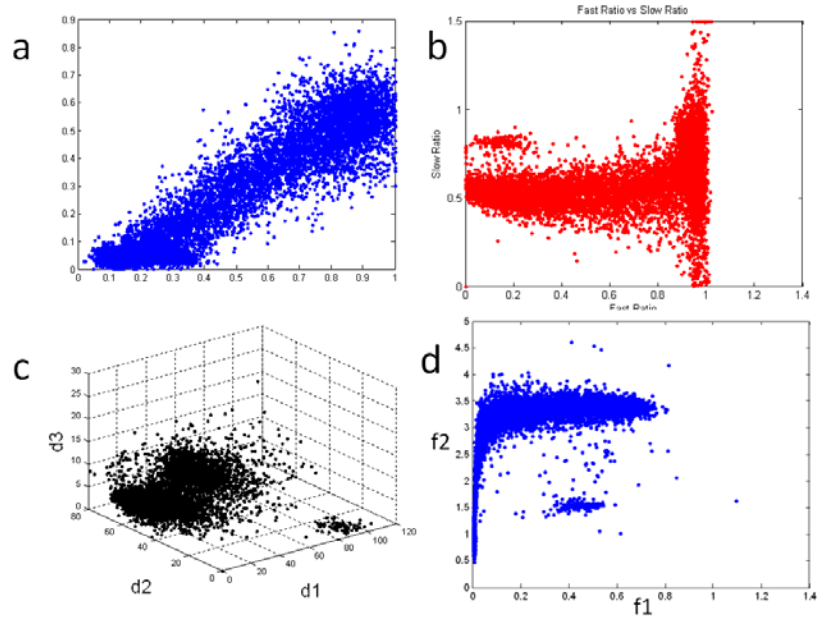

Fig. 4.6. The features of a ^{90}Sr source extracted using four different methods. (a) CTD, (b) Farsoni's method, (c) time-domain fuzzy method, (d) wavelet method.

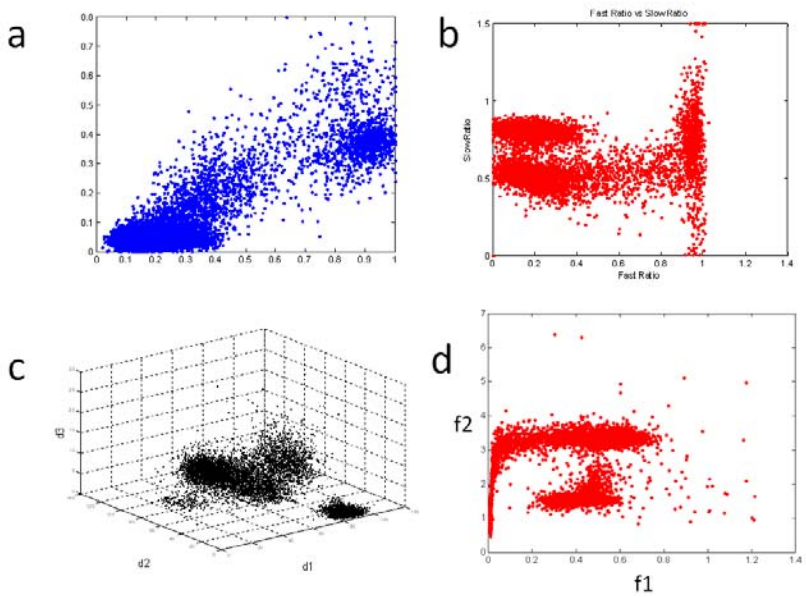

Fig. 4.7. The features of a mixed field of ^{137}Cs and ^{90}Sr/Y sources extracted using four different methods. (a) CTD, (b) Farsoni's method, (c) time-domain fuzzy method, (d) wavelet method.

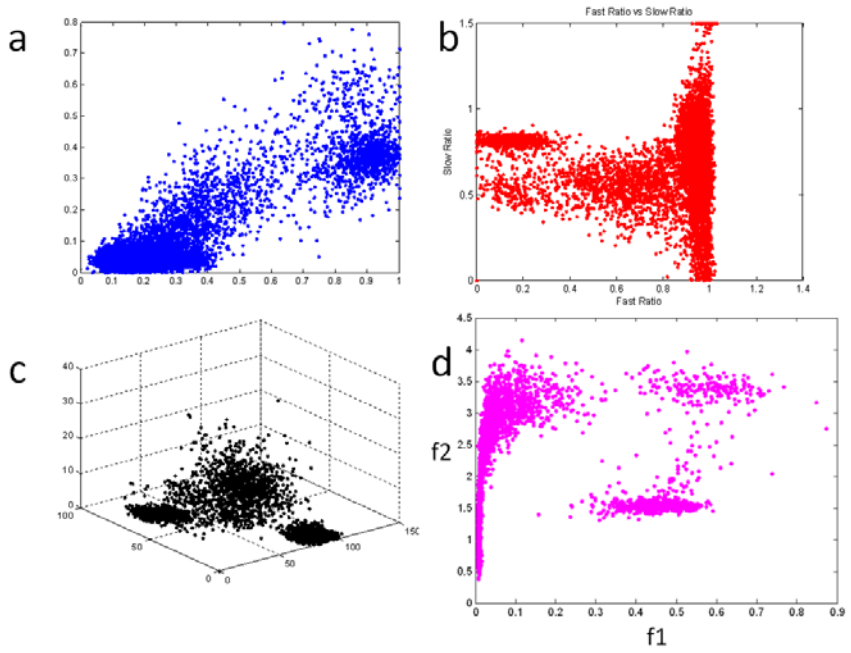

Fig. 4.8. The features of a mixed field of ^{60}Co and ^{99}Tc sources extracted using four different methods. (a) CTD, (b) Farsoni's method, (c) time-domain fuzzy method, (d) wavelet method.

Table 4.1. The comparison between different methods for a ^{137}Cs source.

Method	Gamma Rate (%)	Beta Rate (%)	Pulse Reject (%)
Farsoni's Method	69	1.7	29.3
Time-domain Fuzzy Method	88.6	2.8	8.6
Constant-Time Discrimination	96.6	0.9	2.5
Wavelet Method	85.2	0.7	14.1

Table 4.2. The comparison between different methods for a ^{60}Co source.

Method	Gamma Rate (%)	Beta Rate (%)	Pulse Reject (%)
Farsoni's Method	65.8	1.9	31.3
Time-domain Fuzzy Method	79.3	2.6	18.1
Constant-Time Discrimination	96.8	1.7	1.5
Wavelet Method	79.2	1.6	19.2

Table 4.3. The comparison of different methods for a ^{99}Tc source.

Method	Beta Rate (%)	Gamma Rate (%)	Pulse Reject (%)
Farsoni's Method	95.5	0.8	3.7
Time-domain Fuzzy Method	94.3	0.8	4.9
Constant-Time Discrimination	96.2	1.4	2.4
Wavelet Method	98.6	0.8	0.6

Table 4.4. The comparison between different methods for a ^{90}Sr/Y source.

Method	Beta Rate (%)	Gamma Rate (%)	Pulse Reject (%)
Farsoni's Method	53.1	1.8	44.9
Time-domain Fuzzy Method	56.8	3.8	39.4
Constant-Time Discrimination	53	38	9
Wavelet Method	59.7	1.8	38.5

Although the CTD method seems to have good performance for the ^{137}Cs and ^{99}Tc sources, it misclassifies some of the pulses from the ^{60}Co and ^{90}Sr/Y sources. The feature plots of the ^{60}Co and ^{90}Sr/Y (Fig. 4.4 and Fig. 4.6) prove that the absorption in the 2nd layer of the detector is a common scenario (the pulses from this scenario must be rejected (Farsoni et al. 2007)). However, the CTD method does not reject these pulses. In general, this method classifies the pulses as the fast decay or slow decay and does not discriminate between the absorption in the 2nd layer and the absorption in the 3rd layer. This method does not detect the multiple layer absorptions either. Therefore, the CTD method is not able to discriminate between

seven possible cases which may occur using this triple-layer phoswich detector. Another disadvantage of this method consists in using the timing features, which result in an algorithm very sensitive to noise and to abrupt changes in the signal at specific points. The use of a de-noising algorithm is therefore necessary.

Some low-energy gamma rays (mostly Compton events) interact with the 1st and/or 2nd layer and cause the pulse to be misclassified as beta. However, this phenomenon is not observed at higher energies because the 1st and 2nd layers do not interact with these pulses and they pass so that the spectra of gamma absorption in the 2nd layer should be observed only at low energies. Using the time-domain fuzzy method, the beta energy spectrum (error) of a ^{137}Cs is spread only at low energies. However, beta spectrum using Farsoni's method was spread from low energies to high energies and some high energy pulses, which were absorbed in the 3rd layer, were misclassified as the absorption in the 1st and 2nd layer.

Table 4.5 shows the comparison between Farsoni's method and the time-domain fuzzy method we proposed for a ^{137}Cs source. Although the error rate has increased in this algorithm, fewer pulses were rejected and the FWHM has been improved. The reason that the error rate has increased is that Farsoni's method (2007) is not efficient in detecting pulses with double-decay in the 1st and 2nd layer, and they are mostly rejected. Using the fuzzy algorithm, these pulses are detected effectively and are classified as beta.

Table 4.5. Comparison between Farsoni's method and our fuzzy method

^{137}Cs	Gamma Count (%)	Beta Count (%)	Pulse Reject (%)	FWHM (%)
Farsoni's Method	69.0	1.7	29.3	7.5
Fuzzy Algorithm	88.6	2.8	8.6	6.7

For a ^{99}Tc source, both of the methods show a similar performance but for ^{60}Co and $^{90}Sr/Y$ sources, Farsoni's method rejects more pulses. This phenomenon is a result of the specific cases which arise for these sources. It can be observed that multiple-layer absorption is very common for these sources and Farsoni's method is not effective in detecting these pulses. In general, the time-domain fuzzy method shows better performance than Farsoni's method in detecting multiple-layer absorption.

The time-domain fuzzy method, compared to the wavelet method, has almost equal performance, but is computationally more complex because it uses a wavelet based de-noising algorithm. Both Farsoni's method and the time-domain fuzzy method are sensitive to noise and variations in the pulse shape. Although the time-domain fuzzy method employs a wavelet based de-noising algorithm, it is computationally more complex than the wavelet method and Farsoni's method.

One of the advantages of the wavelet method consists in using the frequency-domain features of the signal which are less sensitive to noise and abrupt changes in

the signal. Therefore, it can be considered a robust algorithm for pulse shape discrimination among pulses with different decaying characteristics.

Another advantage of the wavelet-method consists in detecting the bizarre pulse shapes which represent the pile-up events in the data set and were not detected by the time-domain methods. In the feature plot of the ^{137}Cs source, five major clusters were observed in the data set: the absorption in the 3rd layer, the absorption in the 2nd layer, the absorption in both the 2nd and 3rd layer, the absorption in the 1st layer and the absorption in the 1st and 2nd layer. However, some samples did not belong to any of these clusters. Fig. 4.9 to 4.12 show some of these samples and their corresponding pulse shapes. These pulses represent pile-up events and should be rejected.

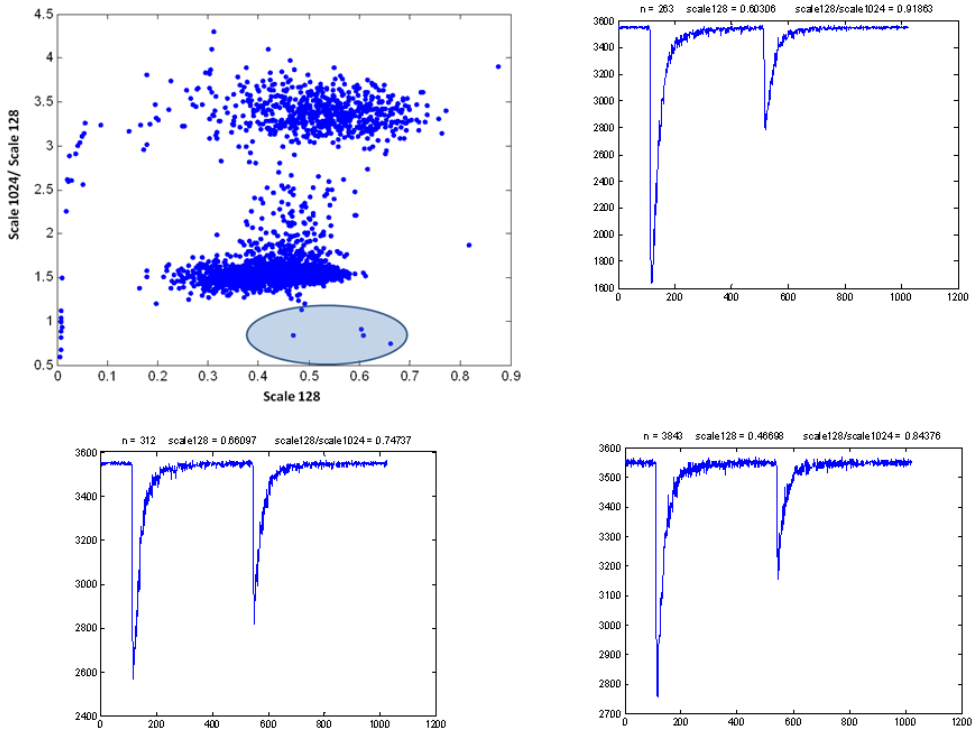

Fig. 4.9. Some bizarre pulse shapes detected in the data set.

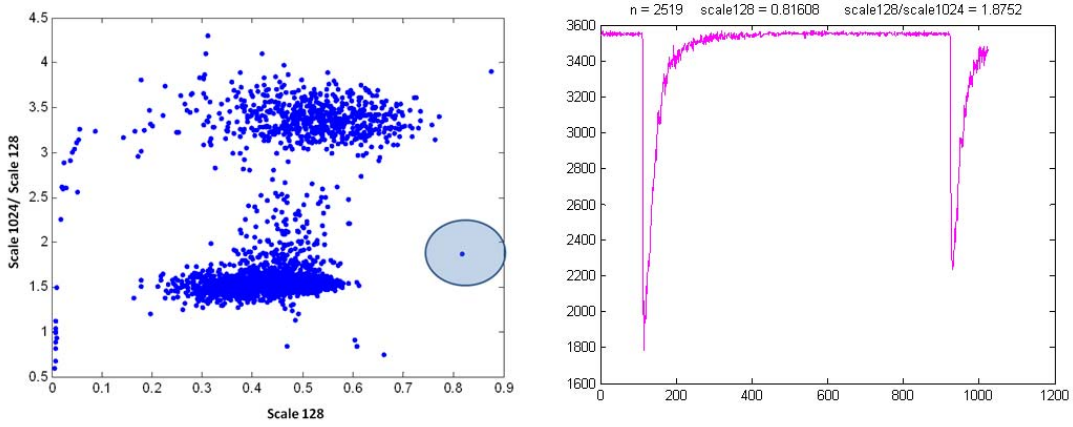

Fig. 4.10. Pile-up pulse.

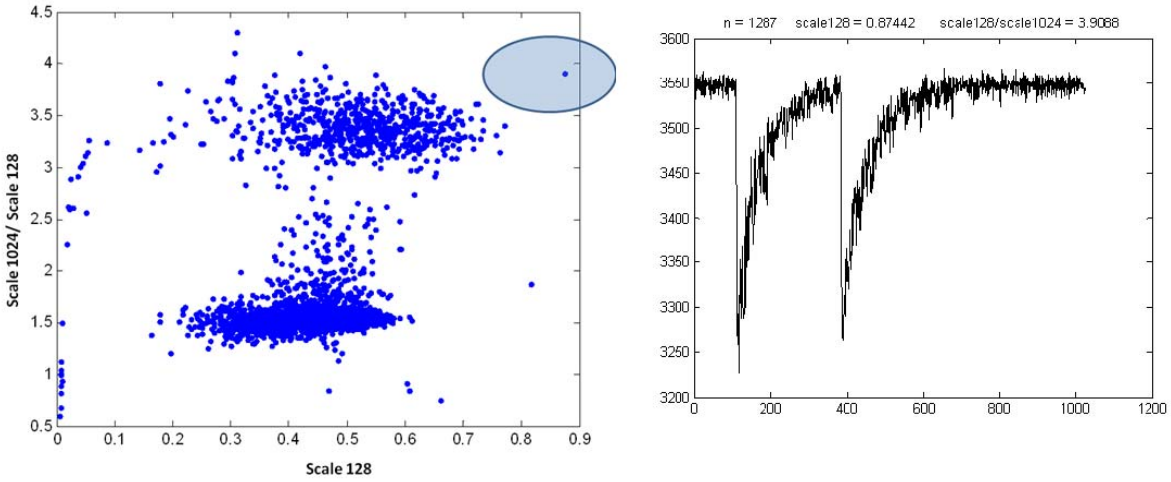

Fig. 4.11. Pile-up pulse.

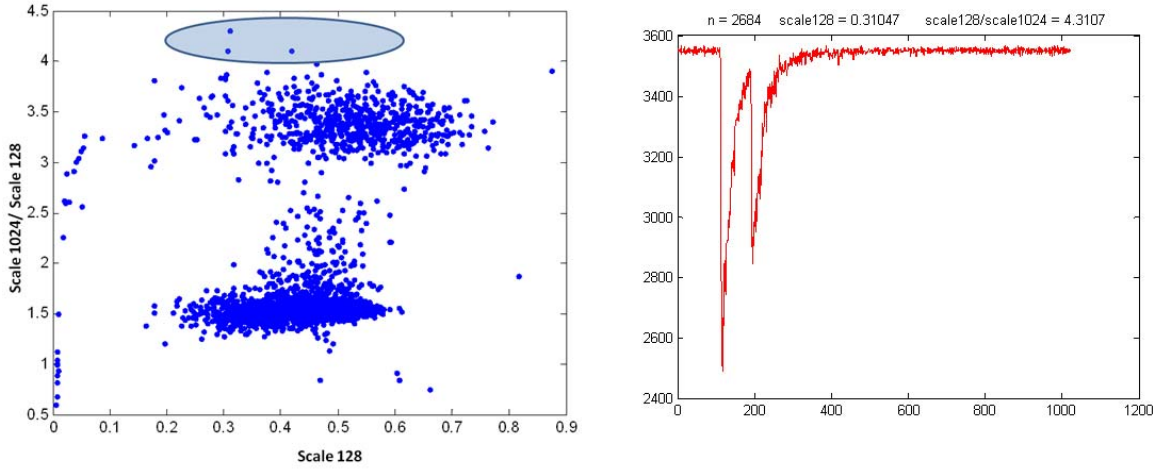

Fig. 4.12. Pile-up pulse.

5 Application of the Wavelet method in neutron/gamma discrimination in liquid scintillators

5.1 Introduction

Neutron spectroscopy has several applications in international safeguard, nuclear material control, and national security. More recently, neutron spectroscopy utilizing organic scintillators has been used for tomographical imaging. Since organic scintillators are also sensitive to γ-ray photons, a pulse shape discrimination (PSD) method between neutrons and γ-rays is necessary.

Liquid scintillators are one of the most popular radiation detection materials because they can be shaped into the desired size for a specific application (D'Mellow et al. 2007). Another advantage of using liquid scintillators is their excellent pulse shape discrimination properties and fast timing performance.

The light produced in organic scintillators can be the result of different decay paths (e. g. fluorescence, phosphorescence, and delayed fluorescence). During the scintillation process, heavier particles show greater energy loss rate and produce delayed fluorescence yielding output pulses that decay more slowly than of those from lighter particles. The difference between the pulse shapes arising from the interaction of heavy particles in scintillation and those stemming from the interaction

of light particles and photons has been exploited in pulse shape discrimination and allows the determination of the radiation type.

Aspinall et al. (2007) verified the discrimination of neutron and γ-ray events in an organic scintillator with the PGA method by comparing the results of the PGA method with those of the Time of Flight (TOF) measurement. Both of the algorithms were implemented in digital logic. The discrimination performance of the PGA algorithm was observed to be consistent with that achieved by the digital TOF.

In this section, we propose a new pulse shape discrimination method based on the wavelet transform which is able to detect neutrons and γ-rays in liquid scintillators. The performance of the wavelet method is compared with PGA. The experimental results show that the wavelet-based pulse shape discrimination method has better performance compared to the PGA algorithm.

5.2 Experimental Set-up

The experimental setup of the scintillator and source is shown in Fig. 5.1. An americium-beryllium (Am/Be) source was exposed to a small-volume (4.5 ml) liquid scintillator (John Caunt Scientific LtD., Oxon, UK) filled with EJ-301, optically-coupled to a fast photomultiplier tube (PMT). The output signal of the PMT was sampled using a fast digitizing oscilloscope (Agilent Technologies Inc.) at a sampling rate of 4

GSPS with a 16-bit amplitude resolution. Data were collected using four different experimental configurations as described in Table 5.1 and were transmitted to the host computer for further processing. A lead shield with a thickness of 50mm was used to attenuate the γ-ray component of the field. The neutron flux was attenuated by moving the source to the back of the tank or through the use of a polyethylene sphere with an external diameter of 208 mm and an internal diameter of 63 mm (D'Mellow et al. 2007). The main use of Am/Be sources is usually in the production of neutrons. However, a gamma-ray can be produced after the alpha-decay of the americium component or as the result of inelastic neutron scattering in the surroundings. Therefore, the Am-Be source can be used as a mixed field of neutrons and gamma rays.

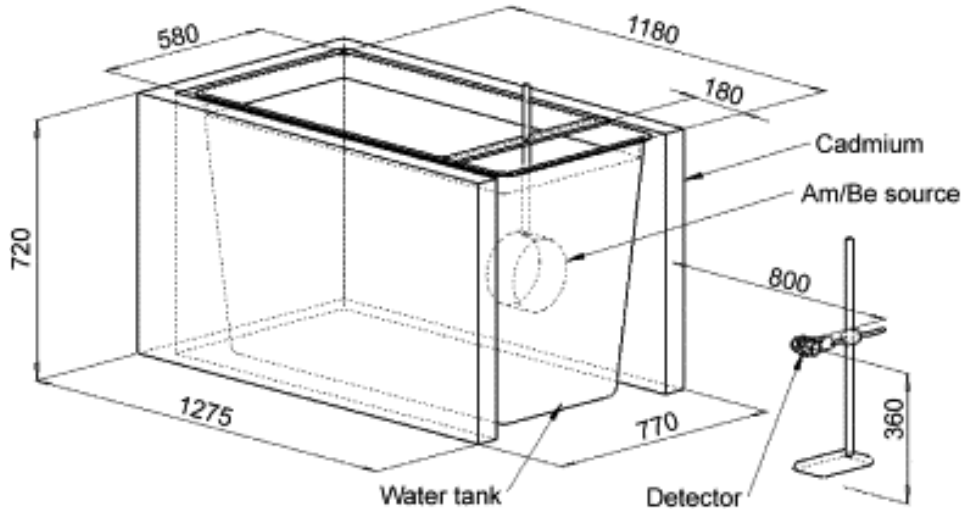

Fig. 5.1. The experimental setup used to record the Am–Be data.

Table 5.1. Neutron and γ-ray moderator configurations investigated with an Am/Be neutron source to achieve data sets of varied neutron/γ ratio.

Configurations	Source Position in tank	Shield	Desired field
1	Front	None	Neutron/γ
2	Front	Polyethylene	γ with reduced neutron
3	Front	Lead	Neutron with reduced γ
4	Front	Polyethylene and lead	Reduced neutron and γ

5.3 Feature Extraction

The same procedure used in the wavelet method (chapter 3.2.2) is applied here to extract relevant features for pulse shape discrimination. First, the continuous wavelet transform is applied to the signal (equation 3.8). Then the scale function of the signal is computed using the equation 3.9.

Typical neutron and γ waveform with their corresponding scale functions are plotted in Fig. 5.2. It can be observed that the scale function provides a good separation between neutron and gamma pulses. The scale functions of 50 normalized pulses captured from a mixed neutron/γ field are plotted in Fig. 5.3. For implementation simplicity, the values of the scale function at scales 512 and 1024 are selected as the discrimination parameters. These scales are chosen as powers of 2 in

order to use the discrete wavelet transform (DWT). The DWT can be easily implemented in digital processors and FPGAs (Ballagh 2001). The optimum features are selected using the following equations

$$f_1 = P(a)|_{a=512}, \qquad [5.1]$$

and

$$f_2 = P(a)|_{a=1024}/P(a)|_{a=512}. \qquad [5.2]$$

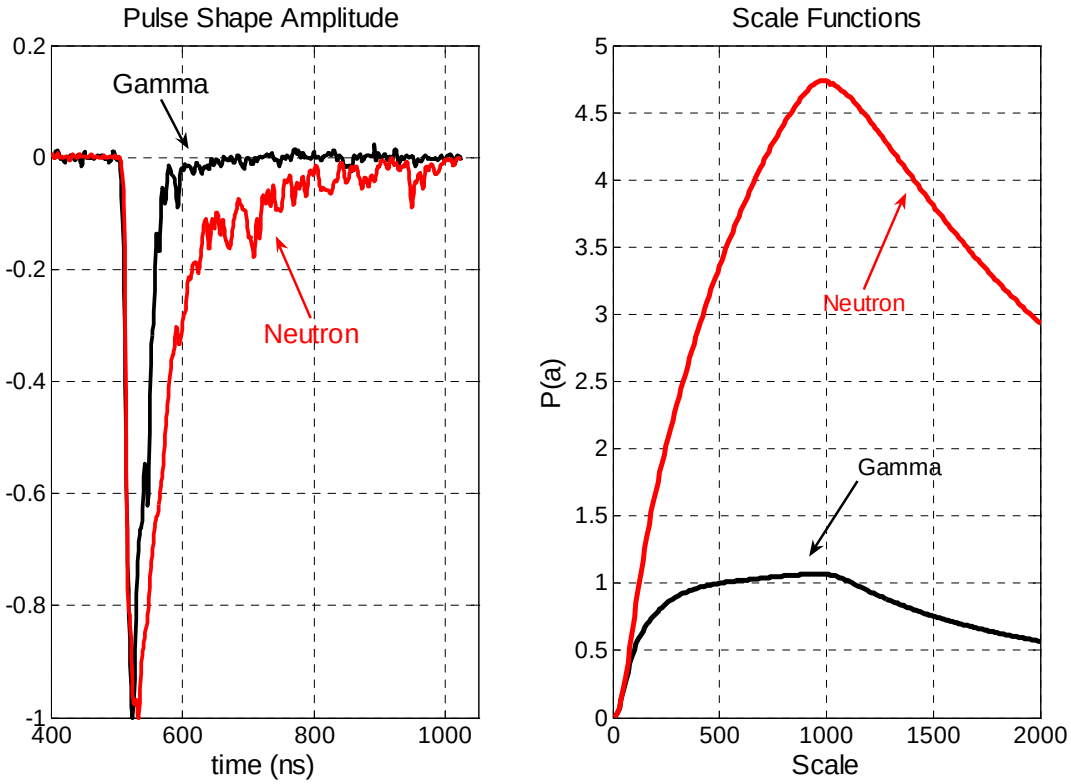

Fig. 5.2. Typical neutron and gamma normalized pulse shapes with their corresponding scale functions.

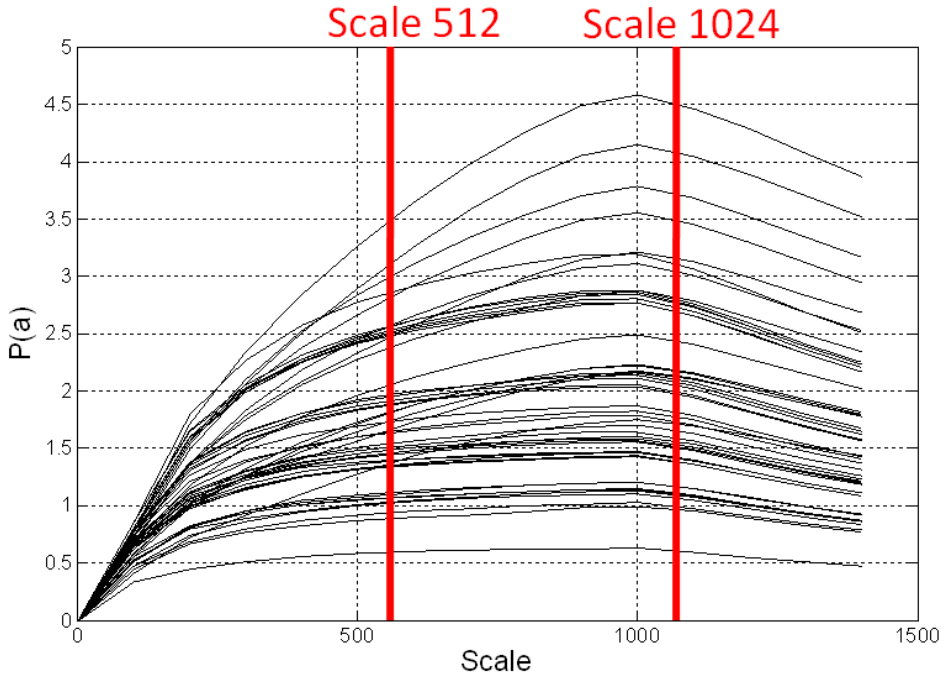

Fig. 5.3. The feature selection diagram for 50 normalized pulses.

5.4 Experimental Results

To verify the performance of the algorithm, the wavelet method was applied to the data from the four configurations reported in Table 5.1, where gamma and neutron events are counted. For each configuration, the scatter plot and the probability histogram are plotted. For the probability histogram plots, the X axis (discrimination value) is the 2nd feature (f_2). Although this feature is not the only discrimination value in the wavelet method, it can be used as a good parameter to visualize the estimated distribution of neutrons and gamma rays and provides a very

good separation of the two sets. The sum of two Gaussian functions is fitted to the histogram, representing the probabilities of neutron and gamma events.

Fig. 5.4 and Fig. 5.5 show the scatter plot and the probability histogram of the first configuration with no additional shielding, respectively. In this experiment, the expected event consisted in observing mostly gamma rays and some neutrons. During this experiment, 734 pulses were captured: 228 pulses were classified as neutrons and 506 pulses as gamma rays and the resulting neutron/gamma ratio was 0.45. Fig. 5.6 and Fig. 5.7 show the scatter plot and the probability distribution of the second configuration, respectively. The expected event in this experiment consisted in observing mostly gamma rays and even fewer neutrons compared to the first configuration. 1050 pulses were captured: 172 pulses were classified as neutrons, and 878 pulses were classified as gamma rays with a corresponding 0.196 neutron/gamma ratio.

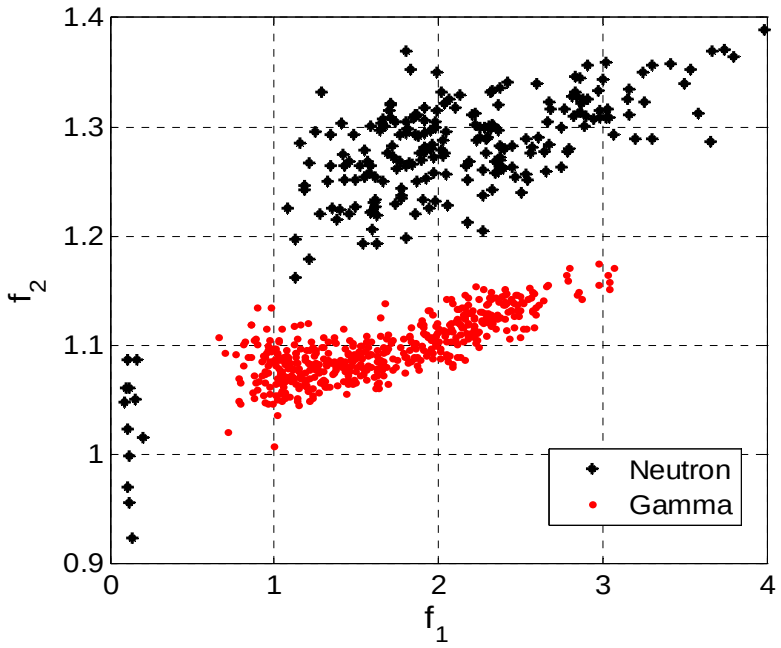

Fig. 5.4. The scatter plot of configuration 1.

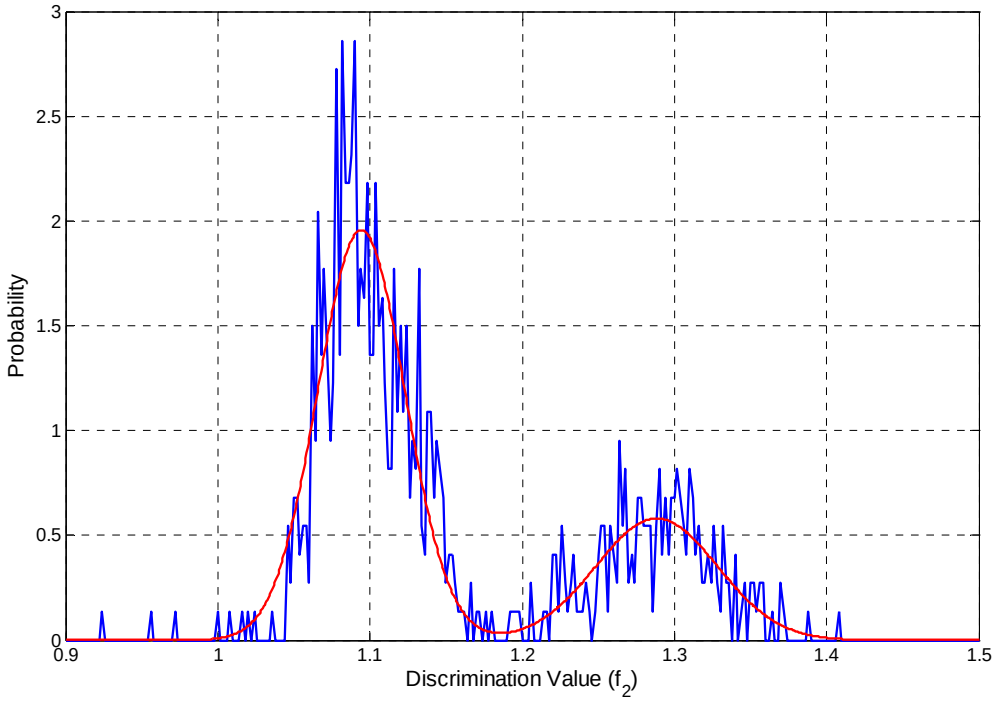

Fig. 5.5. The probability distribution of configuration 1.

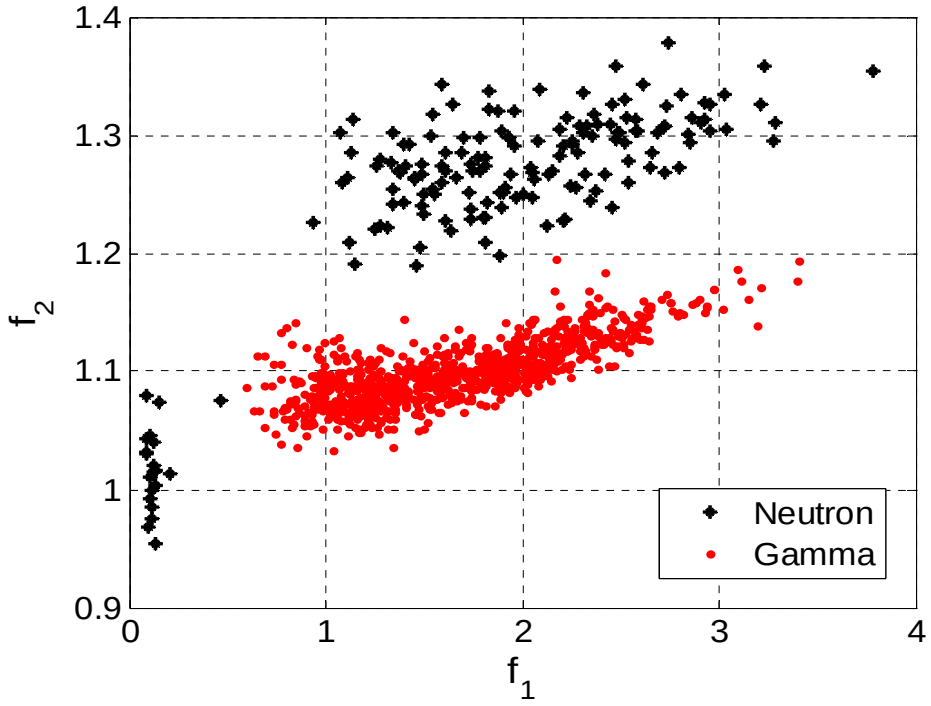

Fig. 5.6. The scatter plot of configuration 2.

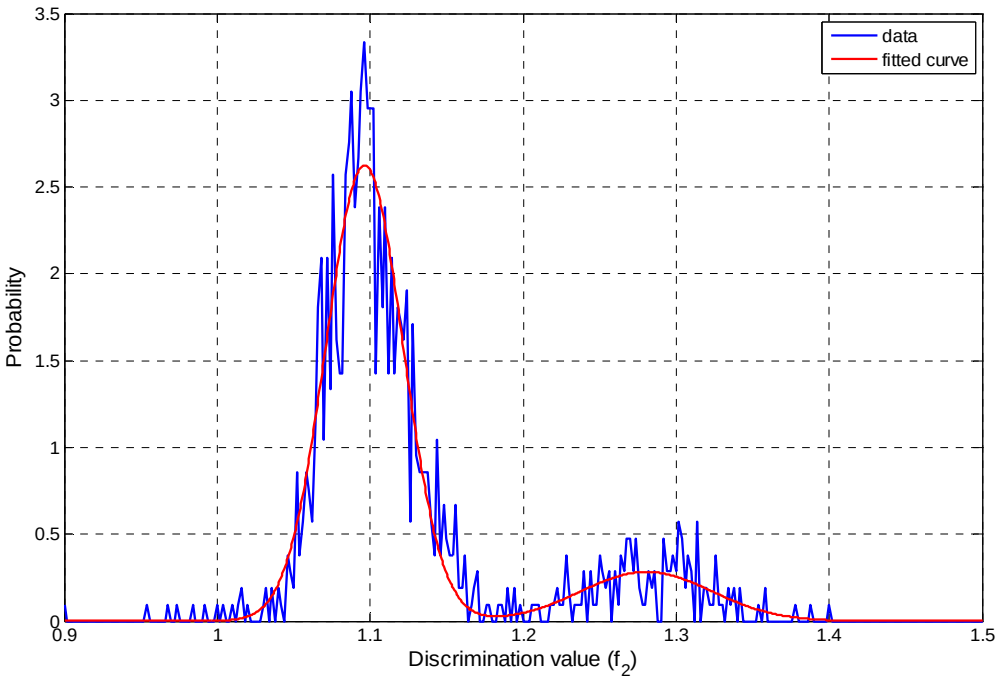

Fig. 5.7. The probability distribution of configuration 2.

Fig. 5.8 and Fig. 5.9 show the scatter plot and the probability distribution of the third configuration in table 5.1, respectively. In this case, the expected event consisted in the observation of equal amounts of neutrons and gamma rays. 2437 pulses were captured: 1242 pulses were classified as gamma rays, and 1195 pulses were classified as neutrons yielding a neutron/gamma ratio of 0.96. Fig. 5.10 and Fig. 5.11 show the scatter plot and the probability distribution of the fourth configuration in table 5.1, respectively. In this case, the event consisted in observing reduced neutrons and gamma rays. 2132 pulses were recorded: 1669 pulses were classified as gamma rays and 463 pulses were classified as neutrons, leading to a 0.277 neutron/gamma ratio.

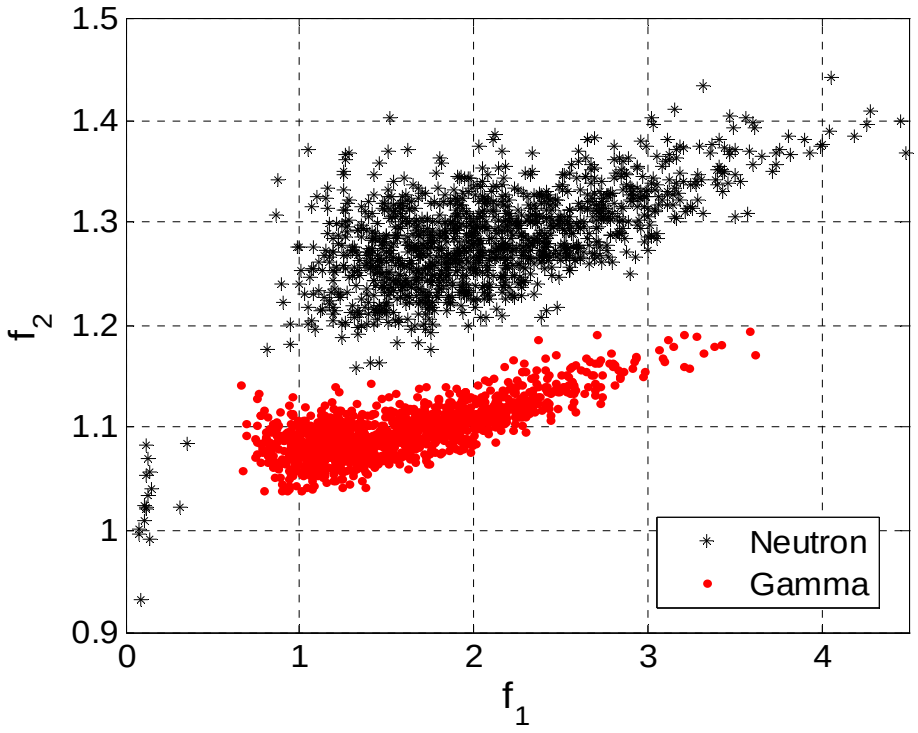

Fig. 5.8. The scatter plot of configuration 3.

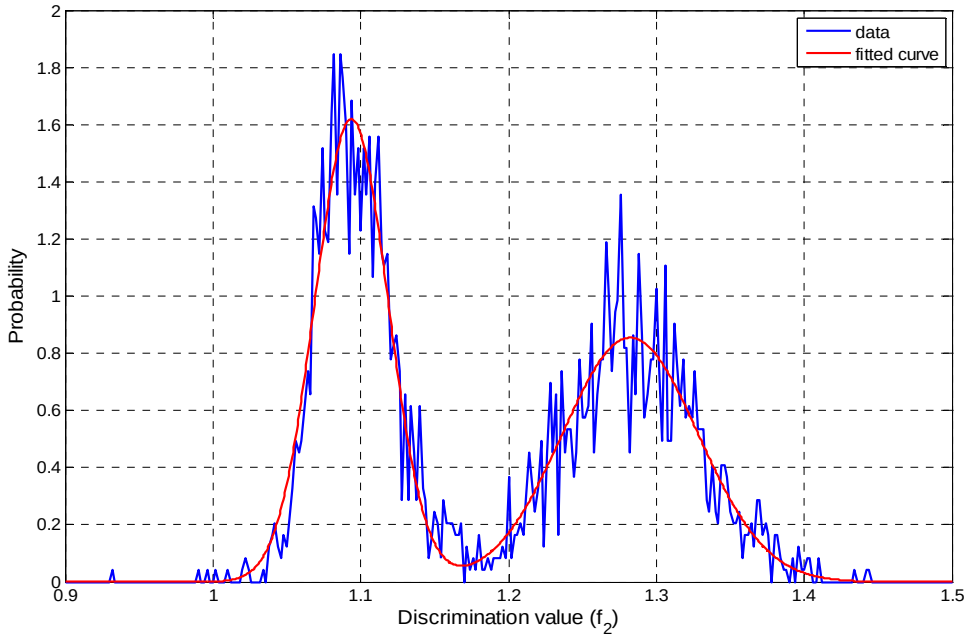

Fig. 5.9. The probability distribution of configuration 3.

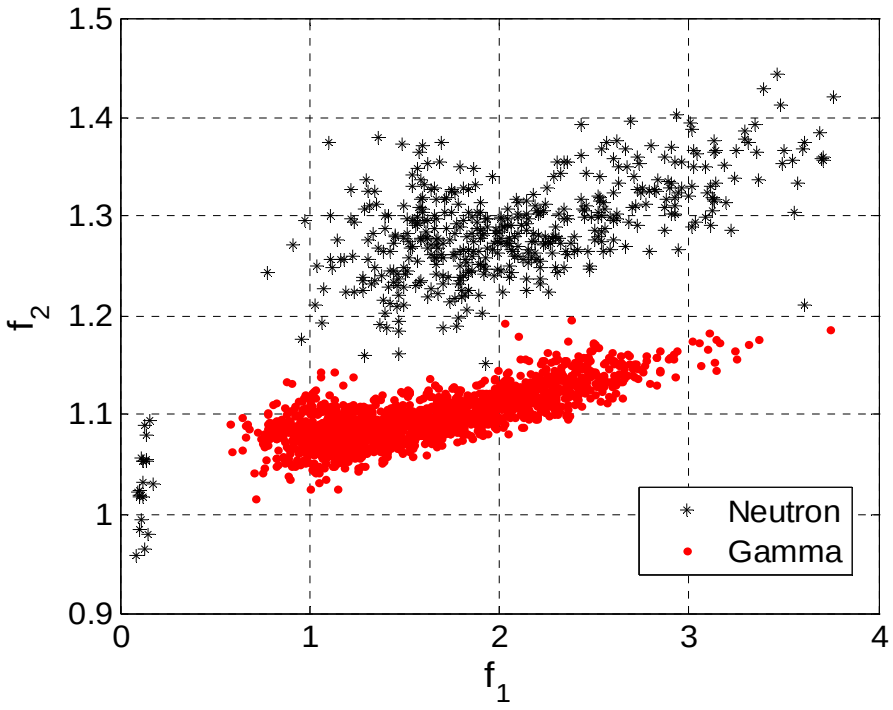

Fig. 5.10. The scatter plot of configuration 4.

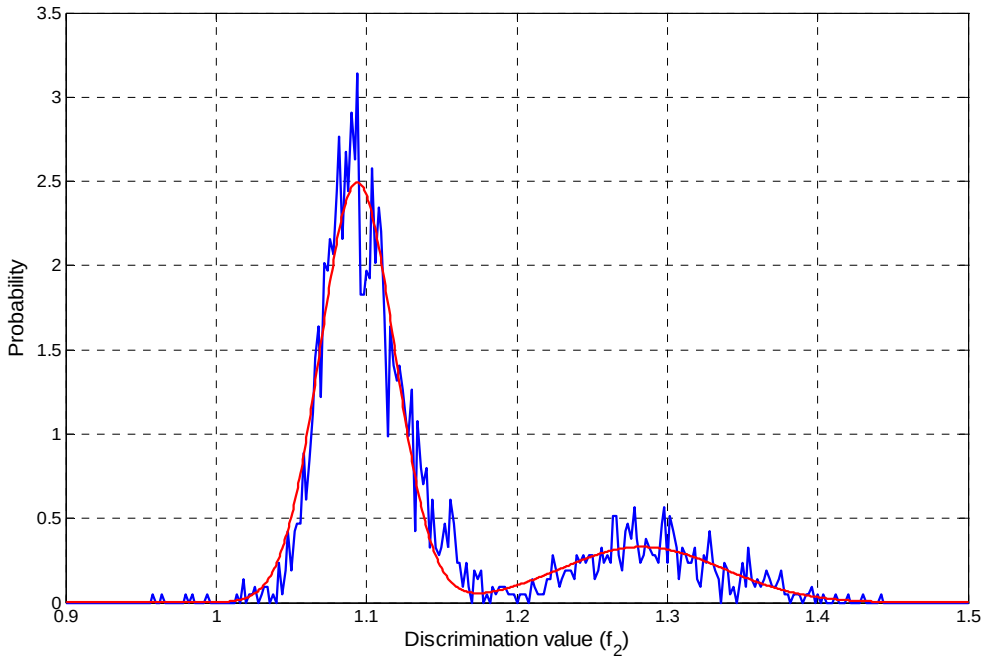

Fig. 5.11. The probability distribution of configuration 4.

The overall results are compared with those obtained with the PGA algorithm. Table 5.2 shows the neutron and γ-ray counts and estimated neutron/γ ratios derived from the scatter plots for the PGA algorithm and for the wavelet method. Also, Table 5.3 shows the fractional areas bounded by the Gaussian fits to the neutron and gamma-ray peaks and estimated neutron/gamma ratios for the probability distribution histograms.

Table 5.2. Neutron and gamma-ray counts and estimated neutron/gamma ratio derived from the scatter plot for PGA algorithm and Wavelet method.

Method	**PGA Algorithm**				**Wavelet Method**			
Configuration	Gamma	Neutron	Total	Neutron/γ	Gamma	Neutron	Total	Neutron/γ
1	490	237	727	0.4837	506	228	734	0.4506
2	859	190	1049	0.2212	172	878	1050	0.1959
3	1202	1234	2436	1.0266	1242	1195	2437	0.9622
4	1612	520	2132	0.3226	1669	463	2132	0.2774

Table 5.3. Fractional areas bounded by the Gaussian fits to the neutron and gamma-ray peaks and estimated neutron/gamma ratio for the probability distribution histograms.

Method	**PGA Algorithm**				**Wavelet Method**			
Configuration	Gamma	Neutron	Overlap	Neutron/γ	Gamma	Neutron	Overlap	Neutron/γ
1	0.7031	0.3035	0.0112	0.4225	0.7236	0.2764	0.0085	0.3746
2	0.8359	0.1682	0.0156	0.1860	0.8454	0.1546	0.0006	0.1822
3	0.4984	0.4541	0.0099	0.9093	0.5055	0.4945	0.0012	0.9782
4	0.5008	0.2444	0.0175	0.3018	0.7739	0.2261	0.0023	0.2899

5.5 Discussion

The results obtained in Table 5.2 with the wavelet method and the PGA algorithm applied to the data from the configurations in Table 5.1 show similar performance. However, the fractional areas in Table 5.3 show that the wavelet method has superior performance compared to the PGA algorithm and that the overlap areas between the neutron and gamma events have dramatically been decreased. Compared to the PGA algorithm, the overlap between neutron and gamma events has decreased 76.8% on average.

Another advantage of the wavelet method over the PGA algorithm consists in using two features which allow a better separation between the possible cases. The discrimination between gamma and neutron events in the wavelet method is obtained by defining simple boundaries, which makes the separation easier compared to the nonlinear discriminator line of the PGA method.

Most of the time-domain methods use samples of the signal at a specific time or ratio with respect to the peak time and amplitude. Therefore, feature selection is very sensitive to noise and variations of the light intensity. The frequency domain analysis allows for removal of the high-frequency noise present in the pulse shape and the extraction of the most important features of the signal.

A comparison between our technique and the PGA algorithm can be performed using the Figure of Merit for the neutron/gamma discrimination defined as

$$FoM = S/(FWHM_n + FWHM_\gamma), \quad [5.3]$$

where *S* is the separation between the peaks of the two events, $FWHM_\gamma$ is the full width half maximum (FWHM) of the spread of events classified as γ-rays and $FWHM_n$ is the FWHM of the spread in the neutron peak (D'Mellow et al. 2007). The comparison between the FoM of the wavelet method and the PGA algorithm is reported in Table 5.4. It can be observed that the FoM has increased noticeably.

Table 5.4. Comparison between the FoM of the PGA algorithm and wavelet method.

Method	PGA Algorithm	Wavelet Method
Configuration	**FOM**	**FOM**
1	0.94861	1.7269
2	0.81773	1.6774
3	0.98306	1.6409
4	0.83117	1.4881

6 Conclusions and Future Work

6.1 Conclusions

In this thesis, a two-channel electronic read-out system for simultaneous detection and discrimination of beta particles and gamma rays has been developed. The system utilizes a two-channel phoswich detector followed by two photomultiplier tubes. The output signal of the photomultiplier tube is digitized and sent to the host computer for further processing. Two new digital algorithms based on Fuzzy Logic and Wavelet Transform for one channel of the detector has been developed.

The overall results are compared with two different methods: the method based on using fast-ratio and slow-ratio (which was originally designed for this detector structure) and the constant time discrimination method. The results presented in Chapter 4 indicate that the constant time discrimination method is not efficient for this detector structure and should not be used in this application. Moreover, this method (fast-ratio/slow-ratio) is not efficient in detecting multiple-layer absorption scenarios. The fuzzy algorithm advanced in this thesis improves the performance of the system in the separation of beta and gamma spectra, especially at high energies. Also, absorption in multiple-layer is detected more efficiently.

The second algorithm is based on the use of the wavelet transform to extract relevant features of the signal in the scale domain (frequency domain) for pulse

shape discrimination. One of the advantages of the wavelet method over time-domain methods consists in using the frequency-domain features of the signal which are less sensitive to noise and abrupt changes in the signal. Another advantage of the wavelet-method consists in detecting the odd pulse shapes which represent the pile-up events in the data set and were not detected by the time-domain methods. Therefore, it can be considered as a robust algorithm for pulse shape discrimination among pulses with different decay characteristics.

The same procedure used in the wavelet method is applied to another scintillation detection structure for neutron/gamma discrimination. The overall results are compared with the PGA method. The fractional areas in Table 5.3 show that the wavelet method has a superior performance compared to the PGA algorithm and that the overlap areas between the neutron and gamma events have dramatically been decreased. Compared to the PGA algorithm, the overlap between neutron and gamma events has decreased 76.8% on average. Also the FoM of the wavelet method has noticeably increased compared with that of the PGA algorithm.

6.2 Future Work

The fuzzy algorithm advanced in this thesis can be optimized using ANFIS (Adaptive Neuro-Fuzzy Interface Systems). In this case, new training data sets should be given to the system to tune the membership functions and increase the

performance of the fuzzy interface system. Also, a new fuzzy interface system can be designed using the wavelet features.

The wavelet method presented in this thesis can be generalized for other scintillation detection systems. The feature selection may vary for different scintillators. However, the scales should be chosen powers of 2 in order use the discrete wavelet transform. The algorithm can be optimized and implemented on FPGA and the device can work as a stand-alone system without the use of PC.

Bibliography

S. Usuda, H. Abe, A. Mihara, “Phoswich detectors combining doubly or triply ZnS(Ag), NE102A, BGO and/or NaI(Tl) scintillators for simultaneous counting of α, β and γ rays“, Nucl. Instr. and Meth. In Phys. Res. A 340 (1994) 540.

S. Usuda, S. Sakurai, K. Yasuda, “Phoswich detectors for simultaneous counting of α-, β(γ)-rays and neutrons”, Nucl. Instr. and Meth. In Phys. Res. A 388 (1997) 193.

T. White, W.Miller, “A triple-crystal phoswich detector with digital pulse shape discrimination for alpha/beta/gamma spectroscopy”,Nucl. Instr. And Meth. In Phys. Res. A 422 (1999) 144.

N. L. Childress, W. H. Miller, “MCNP analysis and optimization of a triple crystal phoswich detector” Nuc. Instr. And Meth. In Phys. Res. A 490 (2002) 263.

Y. Eisen, B. H. Erkkila, R. J. Brake, W. P. Unruh and F. Hajnal, “A new method for measuring beta spectra and doses in mixed beta-photon fields” Nucl. Instr. And Meth. In Phys. Res. A 238 (1985) 187.

H. Hsu, J. Chen, H. Ing, E. T. H. Clifford and T. McLean, “Skin dose measurement with microspec-2^{TM} “,Nucl. Instr. And Meth. In Phys. Res. A 412 (1998) 155.

W. Hennig, H. Tan, A. Fallu-Labruyere, W. K. Warburton, J. I. McIntyre, A. Gleyzer, “A phoswich well detector for radioxenon monitoring”, Nucl. Instr. And Meth. In Phys. Res. A 579 (2007) 431.

W. Hennig, H. Tan, W. K. Warburton, J. I. McIntyre, “Single-channel beta-gamma coincidence detection of radioactive xenon using digital pulse shape analysis of phoswich detector signals”, IEEE Trans. Nucl. Sci. NS-53 (2) (2006) 620.

G. F. Knoll, Radiation Detection and Measurements, Wiley, New York, 2000.

L. Bardelli, M. Bini, G. Poggi, N. Taccetti, “Application of digital sampling techniques to particle identification in scintillation detectors”, Nucl. Instr. And Meth. In Phys. Res. A 491 (2002) 244.

G. Casini, M. Bini, S. Calamai, R. Laforest, P.R. Maurenzig, A. Olmi, G. Pasquali, S. Piantelli, G. Poggi, F. Saint-Laurent, J.C. Steckmeyer, A.A. Stefanini and N. Taccetti, “Energy and angular momentum sharing in dissipative collisions”, Eur. Phys. J. A 9 (2000) 491.

S. Piantelli, L. Bidini, G. Poggi, M. Bini, G. Casini, P. R. Maurenzig, A. Olmi, G. Pasquali, A. A. Stefanini, and N. Taccetti, “Intermediate Mass Fragment Emission Pattern in Peripheral Heavy-Ion Collisions at Fermi Energies” Phys. Rev. Lett. 88 (2002) 052701

A. T. Farsoni, D.M. Hamby, “A system for simultaneous beta and gamma spectroscopy” Nucl. Instr. And Meth. A 578 (2007) 528

A. T. Farsoni, D.M. Hamby, “MCNP analysis of a multilayer phoswich detector for β-particle dosimetry and spectroscopy” Nucl. Instr. And Meth. A 555 (2005) 225

I. Daubechies, “Orthonormal bases of compactly supported wavelets”, Comm. Pure Appl. Math. 41 (1988) 909

S. G. Mallat, “A theory for multiresolution signal decomposition: the wavelet representation” IEEE Trans. Pattern Analysis and Machine Intelligence 11(7) (1989) 674

S. G. Mallat, “Multifrequency channel decompositions of images and wavelet models”, IEEE Trans. Acoust., Speech, Signal Processing, 37 (1989) 2090

A. Kareem, K Gurley, JC Kantor, ” Time-Scale Analysis of Non-stationary Processes Utilizing Wavelet Transforms” Proceedings of the 6th International Conference on Structural Safety and Reliability, Innsbruck, Austria (1993)

M. Farge, "Wavelet transforms and their applications to turbulence”, Annual Reviews of flud mechanics, 24 (1992).

T. J. Wahl and J. S. Bolton, “The Application of the Wigner Distribution to the Identification of Structure-borne Noise Components”, Journal of Sound and Vibration, 163 (1) (1993) 101.

C. Shiguo, Z. Ruanyu, W. Peng, L. Taihua, Enhance accuracy in pole identification of system by wavelet transform de-noising, IEEE Trans. Nucl. Sci. NS-51 (1) (2004) 250.

L. A. Zadeh, Fuzzy Algorithms, Information and Control, vol. 8, pp.338-353 1965

T. Radecki, “A probabilistic approach to information retrieval in systems with boolean search request formulations”, Progress in Cybernetics and System Research, vol. 11 1982

K. Franke, M. Koppen, B. Nickolay, “Fuzzy image processing by using Dubois and Prade fuzzy norms” Proceedings of 15th International Conference on Pattern Recognition, Barcelona, Spain, pp. 518-521, 2000

J. Wachs, H. Stern, Y. Edan, “Parameter search for an image processing fuzzy C-means hand gesture recognition system”, Proceedings of IEEE International Conference on Image processing, Barcelona, Spain, vol. 3, pp. 341-344, 2003

S. Ghidary, Y. Nakata, H. Saito, m. Hattori, T. Takamori, “Multi-modal human robot interaction for map generation”, Proceedings of International Conference on Intelligent Robots and Systems, pp. 2246-2251, 2001

H. Shim, T. J. Koo, F. Hoffmann, S. Sastry, “A comprehensive study of control design for an autonomous helicopter”, Proceedings of 37th Conference on Decision and Control, tampa, FL, pp. 3653-3658, 1998.

L. Magdalena, J. R. Velasco, “Fuzzy Rule-Based Controllers that Learn by Evolving their Knowledge Base”, Genetic Algorithms and Soft Computing, Physica-Verlag, pp. 172-201, 1996.

J. Zhang, A. Knoll, “Designing fuzzy controllers by rapid learning” Fuzzy Sets and Systems 101(2) (1999) 287-301.

Y. Diao, J. L. Hellerstein, S. Parekh, “Using fuzzy control to maximize profits in service level management”, IBM Systems Journal, vol. 41, no. 3, pp. 403-420, 2000.

N. Nedjah, Luiza de Macedo Mourelle, Fuzzy Systems Engineering, Theory and Practice, Springer, 2005.

J. -S. R. Zhang, “ANFIS : Adaptive Network-Based Fuzzy Interface Systems”, IEEE Transaction on Systems, Man and Cybernetics, 23 (3) (1993) 665-685.

J. B. Birks, The Theory and Practice of Scintillation Counting, Electronics and Instrumentation, vol. 27, Pergamon Press, Oxford, 1964.
P. Chandrikamohan, T. A. DeVol, “Comparison of Pulse Shape discrimination methods for phoswich and CsI:TI Detectors”, IEEE Transaction on Nuclear Science, NS-54 (2) (2007) 398.

B. D’Mellow, M. D. Aspinall, R. O. Macin, M. J. Joyce, A. J. Peyton, “Digital discrimination of neutrons and γ-rays in liquid scintillators using pulse gradient analysis”, Nuclear Instruments and Methods in Physics Research A 578 (2007) 191-197.

M. D. Aspinall, B. D'Mellow, R. O. Mackin, M. J. Joyce, Z. Jarrah, A. J. Peyton, "The empirical characterization of organic liquid scintillation detectors by the normalized average of digitized pulse shapes", Nuclear Instruments and Methods in Physics Research A 578 (2007) 261-266.

M. Flaska, S. A. Pozzi, "Identification of shielded neutron sources with the liquid scintillator BC-501A using a digital pulse shape discrimination method", Nuclear Instruments and Methods in Physics Research A 577 (2007) 654-663.

M. D. Aspinall, B. D'Mellow, R. O. Mackin, M. J. Joyce, N. P. Hawkes, D. J. Thomas, Z. Jarrah, A. J. Peyton, P. J. Nolan, A. J. Boston, "Verification of the digital discrimination of neutrons and γ rays using pulse gradient analysis by digital measurement of time of flight", Nuclear Instruments and Methods in Physics Research A 583 (2007) 432-438.

Appendices

Appendix A Fuzzy Method Matlab Code

```
clear all
close all
clc

%%%%%%%% Building a fuzzy Interface system for pulse shape
discrimination

%%%%%%%%% fuzzy_model_test %%%%%%5

clc

a=newfis('npsd');  %%%%
a.input(1).name='d1';
a.input(1).range=[0 200];
a.input(1).mf(1).name='small';
a.input(1).mf(1).type='zmf';
a.input(1).mf(1).params=[30 40];
a.input(1).mf(2).name='large';
a.input(1).mf(2).type='smf';
a.input(1).mf(2).params=[30 40];

a.input(2).name='d2';
a.input(2).range=[0 100];
a.input(2).mf(1).name='medium';
a.input(2).mf(1).type='zmf';
a.input(2).mf(1).params=[30 50];
a.input(2).mf(2).name='large';
a.input(2).mf(2).type='smf';
a.input(2).mf(2).params=[30 50];

a.input(3).name='d3';
a.input(3).range=[0 60];
a.input(3).mf(1).name='small';
a.input(3).mf(1).type='zmf';
a.input(3).mf(1).params=[8 20];
a.input(3).mf(2).name='large';
a.input(3).mf(2).type='smf';
a.input(3).mf(2).params=[8 20];

sigma = .95 ;
a=addvar(a,'output','k1',[-3 3]);
a=addmf(a,'output',1,'negative','gaussmf',[sigma -1]);
a=addmf(a,'output',1,'positive','gaussmf',[sigma 1]);
```

```
a=addvar(a,'output','k2',[-3 3]);
a=addmf(a,'output',2,'negative','gaussmf',[sigma -1]);
a=addmf(a,'output',2,'positive','gaussmf',[sigma 1]);
a=addvar(a,'output','k3',[-3 3]);
a=addmf(a,'output',3,'negative','gaussmf',[sigma -1]);
a=addmf(a,'output',3,'positive','gaussmf',[sigma 1]);

ruleList=[ ...
2 1 1 2 1 1 1 1
1 2 1 1 2 1 1 1
2 2 1 2 2 1 1 1
1 1 2 1 1 2 1 1
2 1 2 2 1 2 1 1
1 2 2 1 2 2 1 1
2 2 2 2 2 2 1 1
];

a=addrule(a,ruleList);



%%%%%%%% loading the data set %%%%%%%
load ('Sr_90')
% load ('Co60');
% load ('sr_90');
% load ('Tc99_Co60')
% load ('Sr90_Cs137')
% data=double(data);
data=double(pulses);
% load('cs137')
% load('cs137_big');
% data=double(Pulses_Cs137);

fuzzy_model_test;

dis = 1;
[r,c]=size(data);
maxg=150000;
maxb=150000;
gbin=0:maxg/500:maxg;
bbin=0:maxb/500:maxb;
gspec=zeros(1,length(gbin));
bspec=zeros(1,length(bbin));


bc=0;
gc=0;
gbc =0;
bbc=0;

lev = 5;
```

```
for n=1:1:r

    100*n/r
    datas(n,:)  = wden(data(n,:),'minimaxi','s','mln',lev,'sym8');
    base(n)=mean(data(n,700:1024));
    [mn,i]=min(datas(n,:));
    if i<200 & mn > 0
    peak_1(n,1)=(base(n)-datas(n,i));

    peak1(n,1)=peak_1(n,1);
    peak_2(n,1)=(base(n)-mean(datas(n,i+3:i+8)));
    peak_ratio(n,1)=abs(peak_2(n,1)/peak_1(n,1));
    new_1(n,1) = base(n)-mean(datas(n,i+4:i+8));

    if (peak_ratio(n,1)< 1/2.4) & (peak_2(n,1) >0) &
(new_1(n,1)/peak1(n,1) >.1) &((datas(n,i+3)-datas(n,i))/peak_1(n,1) <
.8 )
         peak2(n,1) = base(n)-mean(datas(n,i+2:i+3));
    else
        peak2(n,1) = peak_1(n,1);
    end

    d1(1,n)=100*abs((datas(n,i))-(datas(n,i+3)))/peak1(n,1);
    d2(1,n)=100*abs((((datas(n,i+3)))  -
(datas(n,i+30)))/peak2(n,1));
    d3(1,n)=100*abs(((datas(n,i+120)) -
(datas(n,i+350)))/peak2(n,1));
    d(n,:)=[d1(1,n),d2(1,n),d3(1,n)];

    out(n,:)=evalfis(d(n,:),a);
    layer(n,:)=sign(out(n,:));

    mmm(n)=mn;

        if (layer(n,2)==-1) && (layer(n,1)~=-1)

            bc =bc+1;
            beta_index(bc)=n;
            sum_A=(base(n)*11)-sum(datas(n,i-5:i+5));
            sum_B=(base(n)*394)-sum(datas(n,i+6:i+400));
            sum_C=(base(n)*405)-sum(datas(n,i-5:i+400));
            slow_area(bc)=sum_B * 1.176;
            fast_area(bc)=sum_A - (sum_B * 0.16);
            if sum_B>0
                eb(bc)=slow_area(bc) + (fast_area(bc) * 1.92);
            else
                eb(bc)=sum_A *1.92;
            end
            bspec = hist(eb(bc),bbin) + bspec;
           if dis == 1
            subplot(2,1,1)
            plot(bbin,bspec,'r', 'LineWidth',2),xlabel('Energy
channel'),ylabel('Counts')
            title('Beta Energy Spectrum')
```

```
            axis([0 maxb 0 600])
            grid on
           end

        else

           if (layer(n,:)==[-1,1,-1])

                gc=gc+1;
                eg(gc)=(base(n)*411) - sum(datas(n,i-10:i+400));
                gspec = hist(eg(gc),gbin) + gspec;
                if dis ==1
                subplot(2,1,2)
                plot(gbin,gspec,'k', 'LineWidth',2),xlabel('Energy
channel'),ylabel('Counts')
                title('Gamma Energy Spectrum')
                axis([0 maxg 0 80])
                grid on
                end

            else

           bbc =bbc+1;
           end
        end
        end
end

total = [gc , 100*gc/r ; bc , 100*bc/r; bbc , 100*bbc/r ]
```

Appendix B Wavelet Method Matlab Code

```
clear all
close all
clc

load('cs137_big');
data=double(Pulses_Cs137);
% load('sr90');
% load ('Co60')
% load('TC99_big');
% data=double(Pulses_TC99);
% data=double(data);

% data1=double(Pulses_Cs137);
% data2=double(Pulses_TC99);
% data=[data1;data2];
% load ('Co60')
% load ('Tc99_Co60')
% load ('Sr90_Cs137')
% load ('Sr_90')
% data=double(pulses);

dis = 1;
[r,c]=size(data);
maxg=150000;
maxb=150000;
gbin=0:maxg/500:maxg;
bbin=0:maxb/500:maxb;
gspec=zeros(1,length(gbin));
bspec=zeros(1,length(bbin));

bc=0;
gc=0;
gbc =0;
bbc=0;

scale =1024;

for n=1:1:r

    100*n/r
    base(n)=mean(data(n,700:1024));
    [mn,i]=min(data(n,:));
    peak_1(n,1)=(base(n)-data(n,i));
    peak1(n,1)=peak_1(n,1);
    data1(n,:)=(data(n,:)-base(n))/peak1(n,1);

    COEFS1 = cwt(data1(n,:),128:128:scale,'haar');

    [mm,nn]=size(COEFS1);
```

```
    mw=zeros(1,mm);

    for ii=1:1:mm
        for j=1:1:nn
            mw1(1,ii)=(1/nn)*(COEFS1(ii,j).^2);
            mw(1,ii)=mw1(1,ii)+mw(1,ii);
        end
        amghezi1(n,:)=mw(1,:);
    end
    slope_1(n,1)=amghezi1(n,6)/amghezi1(n,1);

    if i < 200 && i >70
        if amghezi1(n,1) < .2
            bc =bc+1;
            beta_index(bc)=n;
            sum_A=(base(n)*11)-sum(data(n,i-5:i+5));
            sum_B=(base(n)*394)-sum(data(n,i+6:i+400));
            sum_C=(base(n)*405)-sum(data(n,i-5:i+400));
            slow_area(bc)=sum_B * 1.176;
            fast_area(bc)=sum_A - (sum_B * 0.16);
            if sum_B>0
                eb(bc)=slow_area(bc) + (fast_area(bc) * 1.92);
            else
                eb(bc)=sum_A *1.92;
            end
            bspec = hist(eb(bc),bbin) + bspec;
            if dis == 1
                subplot(2,1,1)
                plot(bbin,bspec,'r', 'LineWidth',2),xlabel('Energy
channel'),ylabel('Counts')
                title('Beta Energy Spectrum')
                axis([0 maxb 0 600])
                grid on
            end
        else
            if (amghezi1(n,1) > .25) && (slope_1(n,1) < 2.5 )
                gc=gc+1;
                eg(gc)=(base(n)*411) - sum(data(n,i-10:i+400));
                gspec = hist(eg(gc),gbin) + gspec;
                if dis ==1
                    subplot(2,1,2)
                    plot(gbin,gspec,'k',
'LineWidth',2),xlabel('Energy channel'),ylabel('Counts')
                    title('Gamma Energy Spectrum')
                    axis([0 maxg 0 80])
                    grid on
                end
            else
                bbc =bbc+1;
            end
        end
    end
end
total = [gc , 100*gc/r ; bc , 100*bc/r; bbc , 100*bbc/r ]
```

Appendix C Wavelet Method for Neutron/Gamma Discrimination Matlab Code

```
clear all
close all
clc
tic
load('2433_mixed_neutron_gamma_pulses');
% load('AmBe_no_moderator');
% load('AmBe_no_lead_moderator');
% load('AmBe_no_poly_moderator');
% load('AmBe_no_lead&poly_moderator');
data=double(voltsCH1);

scale =1200;
nc=0;
gc=0;
[r,c]=size(data);
MM=1;
NN=r;

for n=MM:1:NN

    100*n/NN
    base(n)=mean(data(n,1:400));
    [mn,i]=min(data(n,:));
    peak_1(n,1)=(base(n)-data(n,i));
    peak1(n,1)=peak_1(n,1);
    data1(n,:)=(data(n,:)-base(n))/peak1(n,1);
    COEFS1 = cwt(data1(n,:),512:512:scale,'haar');
    [mm,nn]=size(COEFS1);
    mw=zeros(1,mm);
    for i=1:1:mm
        for j=1:1:nn
            mw1(1,i)=(1/nn)*(COEFS1(i,j).^2  );
            mw(1,i)=mw1(1,i)+mw(1,i);
        end
    end
    amghezi1(n,:)=mw(1,:);
    slope_1(n,1)=(amghezi1(n,2)/amghezi1(n,1));
    feature_1(n,1)=amghezi1(n,1);
    feature_1(n,2)=slope_1(n,1);
end

%%%%%%%%%%%%%%%%%% gamma nuetron counting %%%%%%%%%%
for n=1:1:r
    if (((feature_1(n,1)>0.5) && (feature_1(n,1)<2) && (
feature_1(n,2))>1.15) ) || ((feature_1(n,1)> 2) && (feature_1(n,2)
> 1.2)) || (amghezi1(n,1)<0.5)
        nc=nc+1;
        neutron(nc,1)=feature_1(n,1);
        neutron(nc,2)=feature_1(n,2);
```

```
        neutron_peak(nc,1)=(1/10000).*peak1(n,1);
    else gc=gc+1;
        gamma(gc,1)=feature_1(n,1);
        gamma(gc,2)=feature_1(n,2);
        gamma_peak(gc,1)=(1/10000).*peak1(n,1);
    end
end
plot(neutron(:,1),neutron(:,2),'.k')
grid on
hold on
plot(gamma(:,1),gamma(:,2),'.r')
grid on
total=[gc nc]
nc/gc
bin=0.9:0.002:1.5;
N=hist(feature_1(:,2),bin);
N=100*N/r;
N2=N';
bin2=bin';
opts = fitoptions('gauss2');
opts.Lower = [0 1 0 0 1.2 0];
opts.upper = [inf 1.15 inf inf 1.4 inf];
ftype = fittype('gauss2');
gfit = fit(bin2,N2,ftype,opts);
figure(2)
plot(bin,N)
hold on
plot(gfit,'r')
grid on
toc

%%%%%%%%%%%%%% The End %%%%%%%%%%%%%%5
```

Appendix D The schematic of the analog circuit board

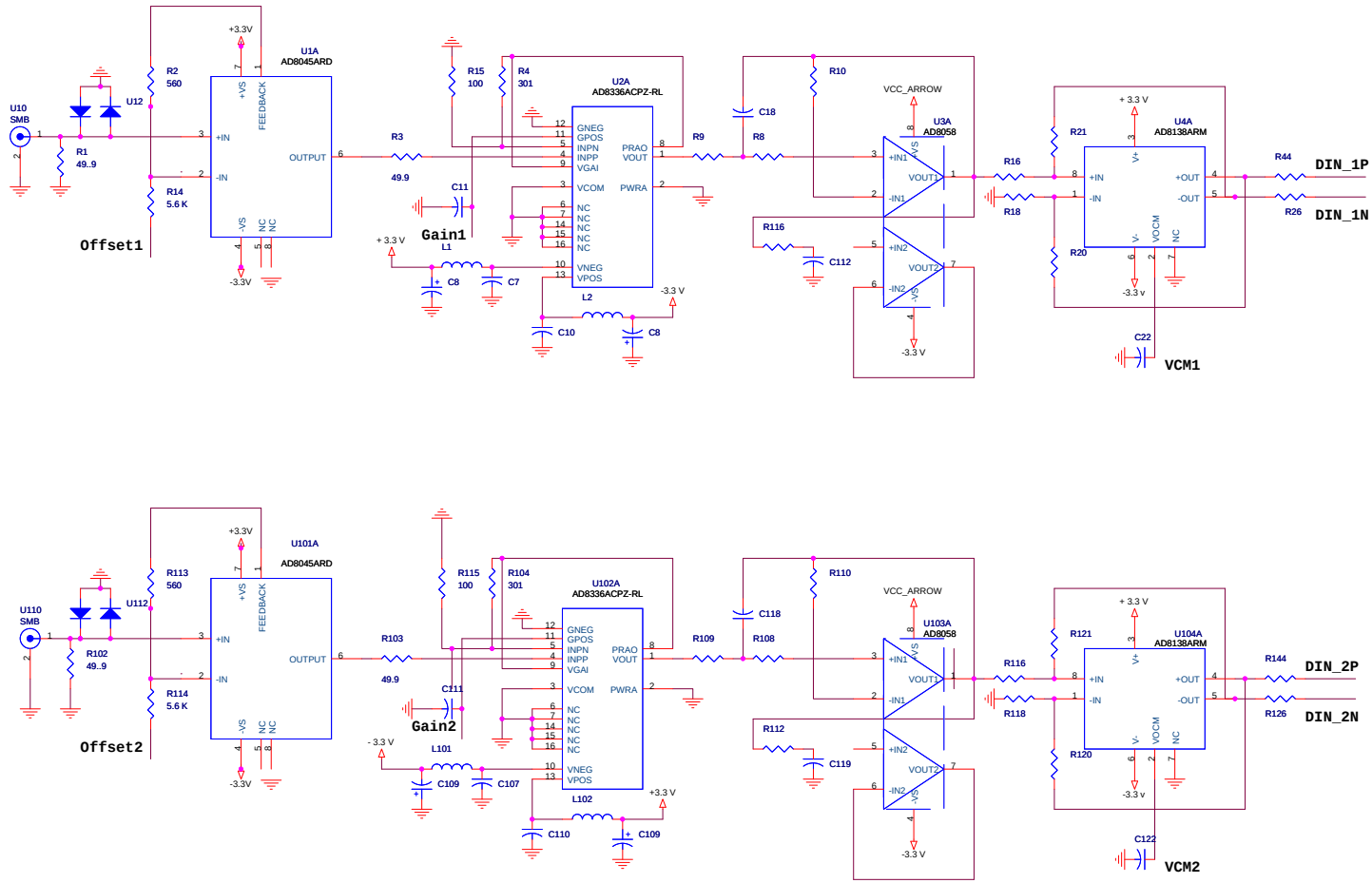
U10
SMB
U12
R1
49..9
R2
560
R14
5.6 K
U1A
AD8045ARD
+3.3V
-3.3V
FEEDBACK
OUTPUT
+IN
-IN
+VS
-VS
NC
Offset1
R3
49.9
R15
100
R4
301
U2A
AD8336ACPZ-RL
GNEG
GPOS
INPN
INPP
VGAI
VCOM
PRAO
VOUT
PWRA
VNEG
VPOS
C11
Gain1
L1
C8
C7
L2
C10
R9
C18
R8
R10
VCC_ARROW
U3A
AD8058
+IN1
-IN1
+IN2
-IN2
VOUT1
VOUT2
R116
C112
R16
R18
R21
R20
U4A
AD8138ARM
V+
V-
VOCM
+OUT
-OUT
R44
R26
DIN_1P
DIN_1N
C22
VCM1
U110
SMB
U112
R102
49..9
R113
560
R114
5.6 K
U101A
AD8045ARD
Offset2
R103
49.9
R115
100
R104
301
U102A
AD8336ACPZ-RL
C111
Gain2
L101
C109
C107
L102
C110
R109
C118
R108
R110
R112
C119
R116
R118
R121
R120
R144
R126
DIN_2P
DIN_2N
C122
VCM2

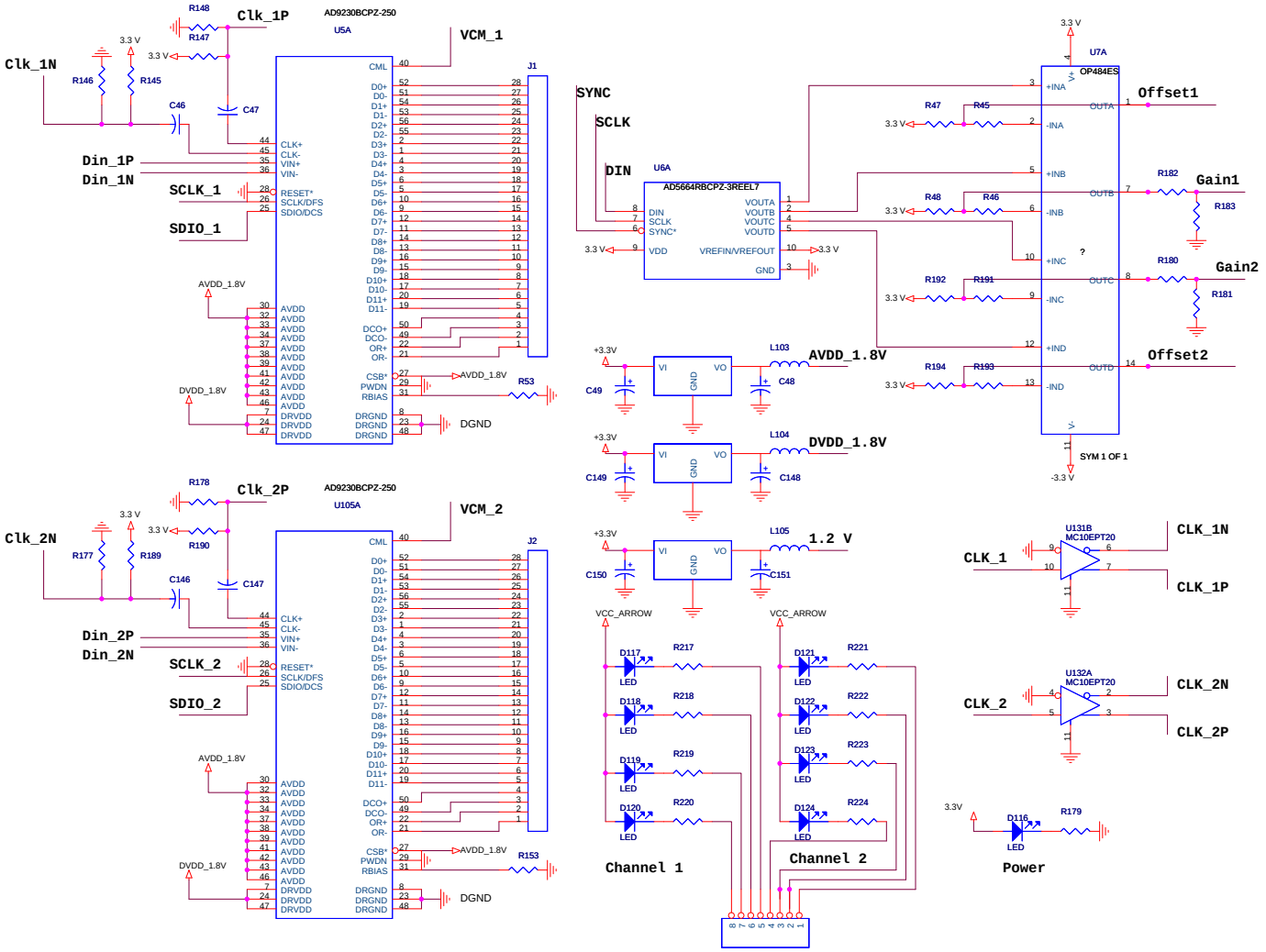
Clk_1P
Clk_1N
Din_1P
Din_1N
SCLK_1
SDIO_1
AD9230BCPZ-250
U5A
VCM_1
J1
Clk_2P
Clk_2N
Din_2P
Din_2N
SCLK_2
SDIO_2
U105A
VCM_2
J2
AVDD_1.8V
DVDD_1.8V
DGND
R53
R153
SYNC
SCLK
DIN
U6A
AD5664RBCPZ-3REEL7
U7A
OP484ES
Offset1
Offset2
Gain1
Gain2
SYM 1 OF 1
L103
AVDD_1.8V
L104
DVDD_1.8V
L105
1.2 V
CLK_1
CLK_2
CLK_1N
CLK_1P
CLK_2N
CLK_2P
U131B
U132A
MC10EPT20
Channel 1
Channel 2
Power